Optimization of Platinum Loading on Partially Fluorinated Carbon Catalysts for Enhanced Proton Exchange Membrane Fuel Cell Performance

Dean E. Glass, Vicente Galvan, Marc Iulliucci and G. K. Surya Prakash*
Loker Hydrocarbon Research Institute, Department of Chemistry, University of Southern California, 837 Bloom Walk, Los Angeles, CA, 90089
*Corresponding Author: gprakash@usc.edu
Phone: (213) 740-5984
Fax: (213) 740-6679

Abstract

The role of partially fluorinated carbon (CFx) supported platinum nanoparticles as proton exchange membrane fuel cell (PEMFC) electrodes in a hydrogen fuel cell was investigated. CFx was employed as a platinum catalyst support via impregnation for oxygen reduction reaction (ORR) at various platinum loadings to determine the optimal loading for ORR and compared to the widely used (non-fluorinated) Vulcan Carbon (XC-72R). In half-cell testing, CFx catalysts displayed greater ORR kinetics at lower Pt loadings while XC-72R displayed higher kinetics at higher Pt loadings. PEMFC tests utilizing 30% wt-platinum on carbon supports as the cathode material revealed a 20% increase in fuel cell performance and an 11% decrease in charge transfer resistance for the CFx supported catalysts compared to that of the XC-72R supported catalysts. PEMFCs tests utilizing 10% wt-platinum on CFx supports as the anode catalyst displayed a 20% increase in power density compared to the XC-72R supported catalyst. Furthermore, utilizing CFx as the support for both anode and cathode electrodes displayed a 15% power density increase compared to XC-72R supported catalysts.

Keywords: CFx-based electrodes; Oxygen reduction; Hydrogen oxidation; PEM fuel cells; Improved water management and efficiency.

1. Introduction

With the ever-growing demand for energy worldwide, fuel cells can offer a viable alternative to the direct combustion of fossil fuels. Fuel cells operate by employing the energy stored in chemical bonds in order to produce electrical energy, often more efficiently compared to conventional heat engines. One of the main reactions found in fuel cells is the oxygen reduction reaction (ORR) performed at the cathode compartment. This is often regarded as the limiting factor in the chemical reaction pathway, yielding slow kinetics when compared to the various oxidation reactions carried out at the anode compartment. The energy involved in the splitting of the oxygen-oxygen double bond can lead to high overpotentials and low power densities in the fuel cell [1,2]. The main pathway for ORR in the acidic media is the 4 e^- pathway shown in equation (1) [3]. This leads to the formation of water and is the desired pathway. Another pathway is the 2 e^- pathway as shown in equation (2). This is less preferred because it forms hydrogen peroxide, which can corrode parts of the fuel cell [4].

$$O_2 + 4H^+ + 4e^- \rightarrow 2H_2O \quad (1)$$

$$O_2 + 2H^+ + 2e^- \rightarrow H_2O_2 \quad (2)$$

Another challenge is the subsequent flooding of the cathode due to the formation of water along with the electro-osmotic drag from the anode [5]. Much has been done to mitigate these effects in order to increase the performance of the membrane electrode assembly (MEA). This has included treatment of the gas diffusion layers (GDLs) with polytetrafluoroethylene (PTFE) [6], modifying the flow fields of the gas channels [7], and controlling the humidity of the gases [8].

Platinum is currently the prime metal catalyst for ORR in many types of fuel cells. It most often exhibits the highest ORR activity when compared to other metal catalysts, most notably in

the acidic media [9,10]. Platinum, however, suffers poisoning at low levels of CO and can be unstable during potential cycling and operation [11,12]. It is also rare and expensive, and its usage should be kept to a minimum for mass production [13]. Some of the synthetic avenues employed to reduce the amount of incorporated platinum include core-shell catalyst design [14,15] and platinum alloyed catalysts [16,17]- particularly PtCo alloyed catalysts employed in the present fuel cell vehicles. Other synthetic avenues utilize catalyst supports in order to maximize the dispersion, surface area, stability, and synergistic effects of the catalyst being studied [18]. Some of the main types of carbon supports are carbon black [19], graphene [20], carbon nanotubes [21], carbon xerogels [22], as well as other metals and doped supports [23,24].

Partially-fluorinated high surface area carbon (CFx) has been implemented mainly as a cathode material for lithium-ion batteries in previous studies [25–27]. This has been shown to lead to higher discharge capacities in batteries by increasing the surface area and pore size within the catalyst layers [28,29]. Sun et al. first worked with fluorinating various carbon blacks such as Black Pearls 2000 and Vulcan Carbon as a stand-alone ORR catalyst in both acidic and alkaline media [30,31]. Since then, other groups have doped various carbon nanostructures with other heteroatoms such as nitrogen and fluorine [32–34] and various other halogens [35,36]. The activity of said catalysts, however, are still less than that of a platinum or noble metal catalyst in the acidic media. Previous research in fuel cells has been carried out using partially fluorinated carbon supports and polytetrafluoroethylene (PTFE) in the gas diffusion layer (GDL) resulting in less flooding in the cathode as well as better oxygen diffusivity, leading to enhanced cell performance [37]. Berthon-Fabry et al. demonstrated the use of fluorinated carbon aerogels for ORR, in which the fluorination process was done either prior to or after the deposition of platinum. They found that the fluorination must be done prior to deposition of platinum or else amorphous

platinum is formed resulting in decreased ORR catalytic activity [38]. Our group has employed commercially available partially fluorinated carbon (CFx, where x is 0.09-0.11), which has electrical conductivity similar to non-fluorinated XC-72R, as a platinum support for the cathode catalyst with a ~40%-wt platinum loading [39]. This led to enhanced performances in both proton exchange membrane (PEM) based direct methanol fuel cells (DMFCs) and hydrogen fuel cells. Furthermore, Chatenets group has studied the role of partially fluorinated carbon supported platinum towards ORR, again with 40%-wt of platinum. They found no difference in stability under simulated "load cycling", however under a start-stop procedure they found the fluorinated carbon supported catalysts to retain higher ECSA and attributed this to mitigation in carbon corrosion [40,41]. Li et al. provided further insight into the improvements in stability of fluorinated carbon supports and determined that the improvement arises from improved charge transfer between the platinum and the fluorinated carbon and, similar to the studies of Chatenet et al., improved resistance to carbon corrosion from introduction of C-F bonds as opposed to only C-O and C-C bonds in nonfluorinated carbons [40,42].

In the present study we have explored a variety of platinum loadings – from 10% to 75% to assess the effect of partial fluorination of the carbon support to gauge the optimal platinum loading conditions in proton exchange membrane fuel cells. The CFx utilized in this study contained a fluorine content of 9-11% to take advantage of the benefits of fluorination while maintaining proper electrical conductivity (electrical resistance < 10 Ω cm). CFx was used and compared directly to the widely adopted Vulcan Carbon (XC-72R) for its utility as a platinum support for ORR kinetics in acidic medium to gauge the ORR and fuel cell performance. Furthermore, we demonstrate the robustness of CFx as it also improves the catalytic activity and stability of platinum towards hydrogen oxidation. Moreover, we utilize CFx supported electrodes

for both the anode and cathode electrodes in a PEMFC and demonstrate superior power density compared to XC-72R supported catalysts.

2. Experimental

2.1 Catalyst Preparation

Platinum salts were deposited on the carbon supports by means of impregnation. Briefly, Vulcan Carbon (XC-72R, Electrosynthesis) and CFx (9%-11% fluorine loading, electrical resistance < 10 Ω cm, Advanced Research Chemicals Inc.) was vigorously stirred and sonicated in 100 mL Millipore water (Direct-Q UV, 18.2 MΩ) until the solution was well dispersed. A certain amount of H_2PtCl_6 (48.8 mM solution) (Alfa Aesar) was then added according to the loading targets of 10%, 25%, 50%, and 75%-wt platinum. These will be referenced as Pt-1C, Pt-2C, Pt-3C, and Pt-4C for the XC-72R supported platinum, and Pt-1F, Pt-2F, Pt-3F, and Pt-4F for the CFx supported platinum, respectively. The pH of the solution was adjusted to neutral by adding 1.0 M NaOH (Macron). The solution was then heated to 80 ℃, reduced with a fresh aqueous solution of sodium borohydride, stirred at 80 ℃ for 2 h, and then stirred at room temperature overnight. It was then washed and centrifuged with Millipore water and until the supernatant had reached a neutral pH, then dried in an oven at 65 ℃.

2.2 Characterization

The N_2 adsorption and desorption measurements were carried out on a Quantachrome Nova 2200E surface area and pore volume analyzer; the specific surface area and pore size distribution were determined by the Brunauer-Emmett-Teller (BET) and Barrett-Joyner-Halenda (BJH) analysis, respectively. SEM and energy dispersive X-ray spectroscopy (EDS) measurements were

performed on a JEOL JSM-7001F electron microscope with an acceleration voltage of 20 kV. TEM measurements were performed on a JEOL JEM-2100F electron microscope with an acceleration voltage of 200 kV. XRD measurements were performed on a Rigaku X-Ray diffractometer using Cu-Kα (0.15458 nm) radiation with a scan rate of 6^{o} min^{-1}. Thermogravemetric analysis (TGA) was performed on a TGA-50 Thermogravimetric Analyzer (Shimadzu). The catalysts were heated up at a rate of 10 °C per minute under air or nitrogen.

2.3 Electrochemical Measurements

The half-cell tests were conducted with a standard rotating disk electrode (RDE) setup. The measurements were taken on a Solartron SI 1287 Potentiostat and analyzed using Corrware Software. Briefly, 1 mg of catalyst was added to a 1 mL solution consisting of 10% isopropyl alcohol, 90% Millipore water, and 10 mg of 5% Nafion® ionomer solution (Ion Power). The solution was sonicated and 20 μL was pipetted onto a glassy carbon RDE (Pine Instruments) with a surface area of 0.195 cm^2. The electrode was dried and placed into a three-electrode testing system with the RDE as the working electrode, a platinum wire as the counter electrode, and a mercury sulfate electrode (0.5 M H_2SO_4 filling soln., 0.68 V vs. RHE) as the reference electrode.

The cell was purged with ultra-pure argon (99.999%) for 15 min before the cyclic voltammetry (CV) scans were performed from 0 V to 1.28 V vs. the reference hydrogen electrode (RHE). For the CO stripping measurements, CO (99.5%) was bubbled into the cell for 30 min followed by argon for 50 min. The cell was scanned at 50 mV s^{-1} for two cycles with the CO being oxidized on the first cycle.

For the ORR measurements, the cell was purged with ultra-pure oxygen (99.994%) for 15 min. Linear sweep voltammetry (LSV) measurements were performed by scanning the potential

from 1.18 V to 0.18 V vs. RHE at 5 mV s^{-1} at rotations of 400, 800, 1200, 1600, 2000, and 2400 RPM. Chronoamperommetry measurements were taken at 0.18 V vs. RHE at 1600 RPM for 3000 seconds. Start-stop stability measurements were performed under Ar by scanning the potential from 1.0 V to 1.5 V vs. RHE at 0.5 mV step increments and holding at each potential for 3 seconds. Further durability measurements were conducted under O_2 flow and doing 3000 CV scans from 0.45 V to 0.95 V vs. RHE.

For the HOR measurements, the cell was purged with ultra-pure hydrogen (99.999%) for 30 minutes. LSV measurements were performed by scanning the potential from -0.08 V to 0.115 V vs. RHE at 5 mV s^{-1} at rotations of 400, 800, 1200, 1600, 2000 and 2400 RPM. Start-stop stability measurements were performed under Ar by scanning the potential from 0.17 V to -0.27 V vs. RHE at 0.5 mV step increments and holding at each potential for 3 seconds. Further durability measurements were conducted under H_2 flow and doing 3000 CV scans between -0.03 V to 0.22 V vs. RHE.

2.4 MEA Fabrication

Catalyst inks were made from a 1:3:5 weight ratio of catalyst to Millipore water to 5% Nafion® ionomer solution respectively for both the cathode and anode. The resulting Nafion® ratio was 20% based on the equation:[43]

$$\frac{W_{Naf}}{W_{Naf} + W_{Cat}} x100 \quad (3)$$

where W_{Naf} is the dry weight of the Nafion and W_{Cat} is the weight of the catalyst and carbon support.

The ink was sonicated and then painted onto a 5 cm^2 Toray Carbon Paper electrodes (E-TEK, TGH-060, 10% wet proofing). For ORR, platinum black (Premetek Co.) was used on the anode with a loading of 2.8 mg cm^{-2} and either the Pt-2C or Pt-2F catalysts on the cathode with a platinum loading of 0.5 mg cm^{-2} to ensure the limiting reaction would be the ORR at the cathode. For HOR, Pt-1 or Pt-2 catalysts were painted onto the electrode until a platinum loading of 0.5 mg cm^{-2} was obtained. For the cathode 40% Pt/C was painted onto the electrode until a platinum loading of 1.6 mg cm^{-2} was obtained. Furthermore, an MEA with Pt-1 and Pt-2 as the anode and cathode electrode, respectively, was also prepared with a platinum loading of 0.5 mg cm^{-2} of platinum on both anode and cathode electrodes. The electrodes were then dried in an oven at 110 ℃. The proton form of Nafion®-211 was prepared and sandwiched between the cathode and anode and hot pressed at 140 ℃ for 5 min at 500 kilograms of force. The MEA was then hydrated overnight at room temperature.

Commercial Pt/C catalyst (Alfa Aesar, 40%-wt platinum) was also mixed with CFx, via ball-milling, to give three-part ratios denoted as Pt-CFx. Catalyst inks were formulated in the same manner previously mentioned and painted onto the Toray Carbon paper electrodes with a total cathode catalyst loading of around 1.8 mg cm^{-2}. MEAs were also fabricated and treated in the same manner.

2.5 Fuel Cell Measurements

The fuel cell polarization measurements were performed using a Fuel Cell Test System 890B (Schribner Associated). The MEAs were tested at an ambient cell temperature (~23 ℃) and either 50 ℃ or 60 ℃. For ORR, humidified hydrogen was flowed through the anode compartment at 100 mL min^{-1} at 85 ℃ while humidified oxygen was flowed through the cathode compartment

at 150 mL min^{-1} at 85 ℃. For HOR, humidified hydrogen was flowed through the anode compartment at 100 mL min^{-1} at 85 ℃, while oxygen was flowed through the cathode compartment at 50 mL min^{-1} at 85 ℃. The relative humidity for each of the gases was 100%. Electrochemical impedance spectroscopy (EIS) measurements were performed with a Solartron SI 1287 and SI 1260 Impedance-Phase Analyzer. EIS measurements were taken a 0.4 V vs. RHE with an amplitude of 10 mV at a frequency range of 100 kHz to 100 mHz.

3. Results and Discussion

3.1 Characterization of the Catalysts

The specific surface area of the CFx and XC-72R supports were determined via BET, shown in Figure S1a&b with the values reported in Table S1, there is a slight decrease in surface area for the CFx compared to the XC-72R. Furthermore, the pore volume for the CFx was larger than XC-72R due to the disruption of the carbon structure by introduction of fluorine, as shown previously [38]. TGA tests were performed on the catalysts to determine the platinum loading on each of the catalysts shown in Figure S2a&b. The platinum weight percent in the samples was calculated and shown in Table S2. Both the XC-72R and CFx were ran as blanks and the resulting weights subtracted from the results for each of the samples. The actual platinum loading on the CFx had a greater deviation from the target loading than the XC-72R due to the lower solubility in the aqueous solution during impregnation.

SEM images of the catalysts were obtained and shown in Figures S3a-d for CFx supports and Figures S4a-d for XC-72R supports. The images show similar macro surface morphologies irrespective of the platinum loading and support material. For better resolution of the platinum nanoparticles, TEM images were obtained and are shown in Figure 1a-d for Pt-1 and Pt-2 with the

corresponding particle size distribution histograms in Figure S5a-d and the remaining images of catalysts are shown in Figure S6 with the corresponding particle size histograms and average particle size distributions. The particle size of the platinum nanoparticles is 3.712±1.832, 3.58±1.322, 4.127±1.256, and 3.798±1.493 nm for the Pt-1F, Pt-2F, Pt-3F, and Pt-4F catalysts, respectively and 4.640±1.626, 3.654±1.222, 4.241±1.650, and 5.076±1.856 nm for the Pt-1C, Pt-2C, Pt-3C, and Pt-4C catalysts, respectively. At each respective platinum loading, the particle size for the CFx supports is smaller than for the XC-72R supports. This could be due to the hydrophobic nature of the CFx aiding in the particle dispersion during the impregnation process. The average particle sizes are close to the ones reported in our previous study [39]. XRD patterns were taken and are shown in Figures S7a&b. In each of the platinum-based catalyst patterns, there are 3 characteristic peaks at 2θ values of: 40.0°, 46.6°, and 67.9° signifying the face centered cubic (fcc) structure of platinum with crystallographic indices of (111), (200), and (220), respectively. These peaks tend to become more pronounced as the platinum loadings increase in the samples. The peak at a 2θ value of 25.2° signifies the (002) graphitic phase of both the XC-72R and CFx supports and diminishes as the platinum loadings increase. The patterns for XC-72R and CFx display very similar features showing the fluorination of the high surface area carbon does not affect the overall crystallographic morphology of the platinum or carbon support, which is similar to what was observed in previous reports.[38,42]

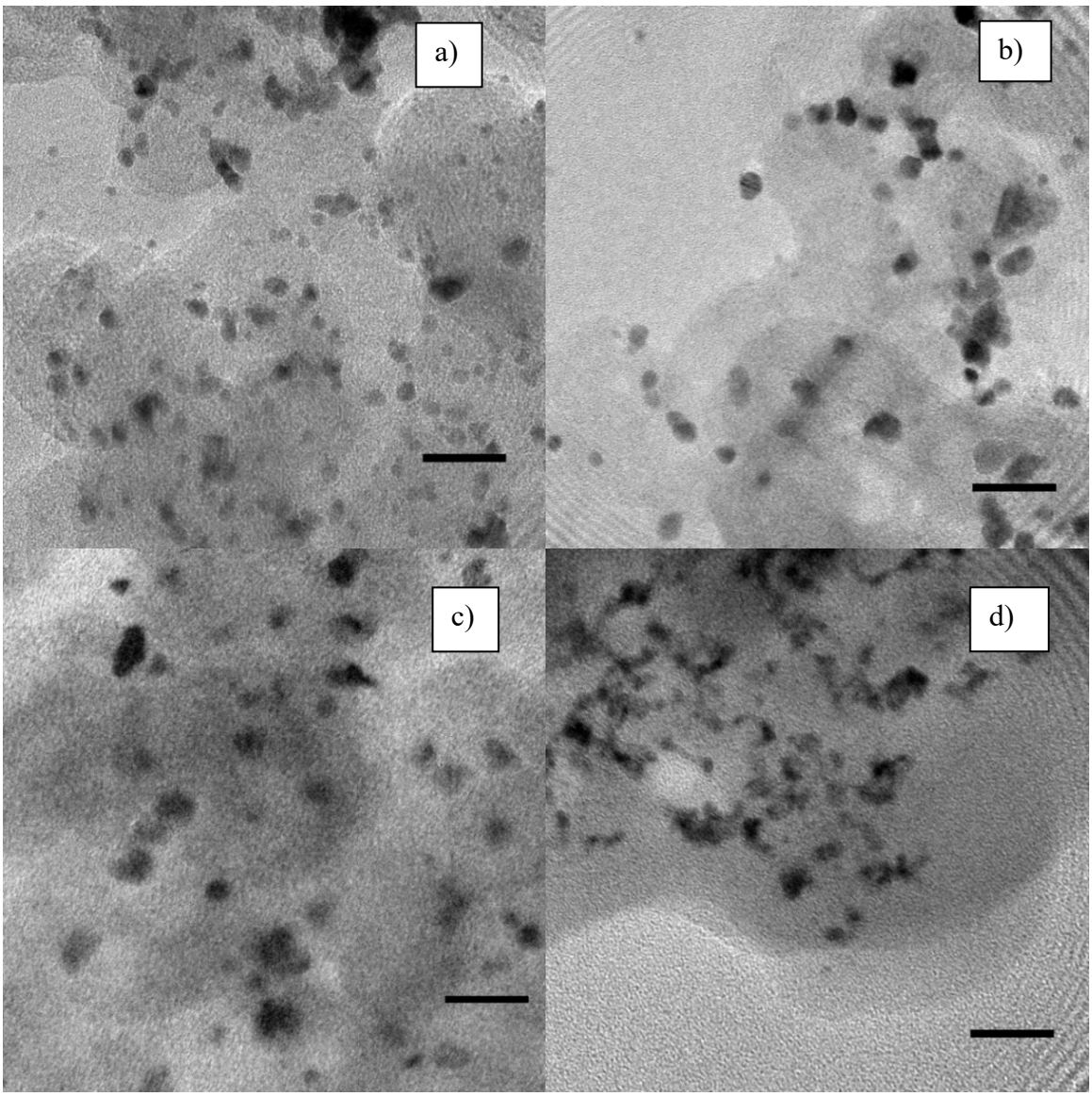

Figure 1. TEM images of the catalysts with the particle size distribution charts of: a) Pt-1F; b) Pt-2F; c) Pt-1C; d) Pt-2C. The measuring bar indicates 20 nm.

3.2 Electrochemical Tests

The platinum loadings for the half-cell testing were calculated to be 3.18, 6.00, 13.68, and 16.64 µg for the Pt-1F, Pt-2F, Pt-3F, and Pt-4F catalysts, respectively and 2.06, 6.12, 9.98, and 14.76 µg for the Pt-1C, Pt-2C, Pt-3C, and Pt-4C catalysts, respectively. A CV scan of the catalysts in 0.5M H_2SO_4 under Ar at 20 mV s^{-1} is shown in Figure 2a for the Pt2-F and Pt2-C catalysts and

in Figure S9 for all the catalysts. The XC-72R supports display an increase in catalytic activity as the platinum loading increases. This trend is however reversed for the CFx supports, whereas the lower platinum loadings display a greater catalytic activity especially in the hydrogen adsorption/desorption range. This can be indicative of a higher surface area stemming from a higher dispersion of the catalyst especially at lower platinum loadings. CO stripping was performed to obtain the electrochemically active surface area (ECSA), which was calculated from the area under the CO oxidation peak in Figure S8 from the first scan and subtracted from the second scan. The ECSA was then calculated from the total charge and based on the charge required to strip the monolayer of surface, Q_{CO}, equal to 420 $\mu C\ cm^{-2}$ [44]. The ECSA was also obtained from the hydrogen adsorption region and was calculated from the area above the curve in the potential region between 0 V to 0.4 V and subtracted from the double layer capacitance portion of the CV located at around 0.4 V. The ECSA was calculated from this total charge and based on the charge required for hydrogen desorption of 210 $\mu C\ cm^{-2}$ [45]. The ECSAs from both the CO stripping and hydrogen adsorption display a decrease in ECSA for both the CFx and XC-72R supports as the platinum loadings decrease as reported in Table 1. The ECSAs of the CFx supported catalysts are higher than those of the XC-72R supported catalysts at the lower loadings and vice versa at the higher loadings. This is likely due to the increased agglomeration of platinum particles on the CFx at higher loadings due to the hydrophobic nature compared to that of the XC-72R. The improved dispersion of the platinum nanoparticles on the CFx support in the lower loadings is evident from the comparison of TEM images. The size of the platinum nanoparticles also has an effect on the ECSA of the catalysts. It has been shown that the optimal size of the platinum nanoparticles for ORR activity regarding the ECSA is between 2-4 nm in diameter [46,47]. Most of the Pt-F catalysts have size distributions in this range while only Pt-2C and Pt-

3C catalysts fall in this range. Furthermore, the CVs of the CO stripping experiments display a change in the onset potential for CO oxidation where the CFx supported catalysts have a more negative potential compared to the XC-72R supported catalysts. This negative shift in potential indicates a more facile removal of CO from the surface which arises from the stronger metal to support interaction. Kato et al. demonstrated that preparing Pt nanoparticles on a nitrogen doped carbon shifted the CO oxidation potential when compared to Pt nanoparticles on carbon without nitrogen. This shift in potential was attributed to a shift in the d-band center of Pt caused by a strong metal to support interaction; the strong metal-support interaction has also previously been shown to occur with Pt and fluorinated carbons [42,48]. Moreover, the role of Pt loading on CO oxidation has previously been studied and it was shown that higher loading of Pt resulted in lower peak potential due to Pt agglomeration and a higher CO oxidation potential results from Pt nanoparticles in the low loadings [49]. A similar trend is observed here, where the Pt-1 displays the highest potential for CO oxidation and Pt-3 and Pt-4 demonstrate a lower potential for CO oxidation. However, the Pt-2 series demonstrated the lowest potential for CO oxidation even though the TEM micrographs demonstrate the prevalence of smaller nanoparticles. This difference may arise from different surface defects and facets and size distribution of the particles [50].

One particular aspect worth mentioning regarding the electrochemical tests is that whereas the XC-72R powder displayed better dispersion in aqueous solution during the impregnation process, the Pt-F catalysts displayed enhanced dispersion in the catalyst ink solutions for the electrochemical tests. This is due to the interactions between the fluorine present in CFx with the tetrafluoroethylene backbone in Nafion®.

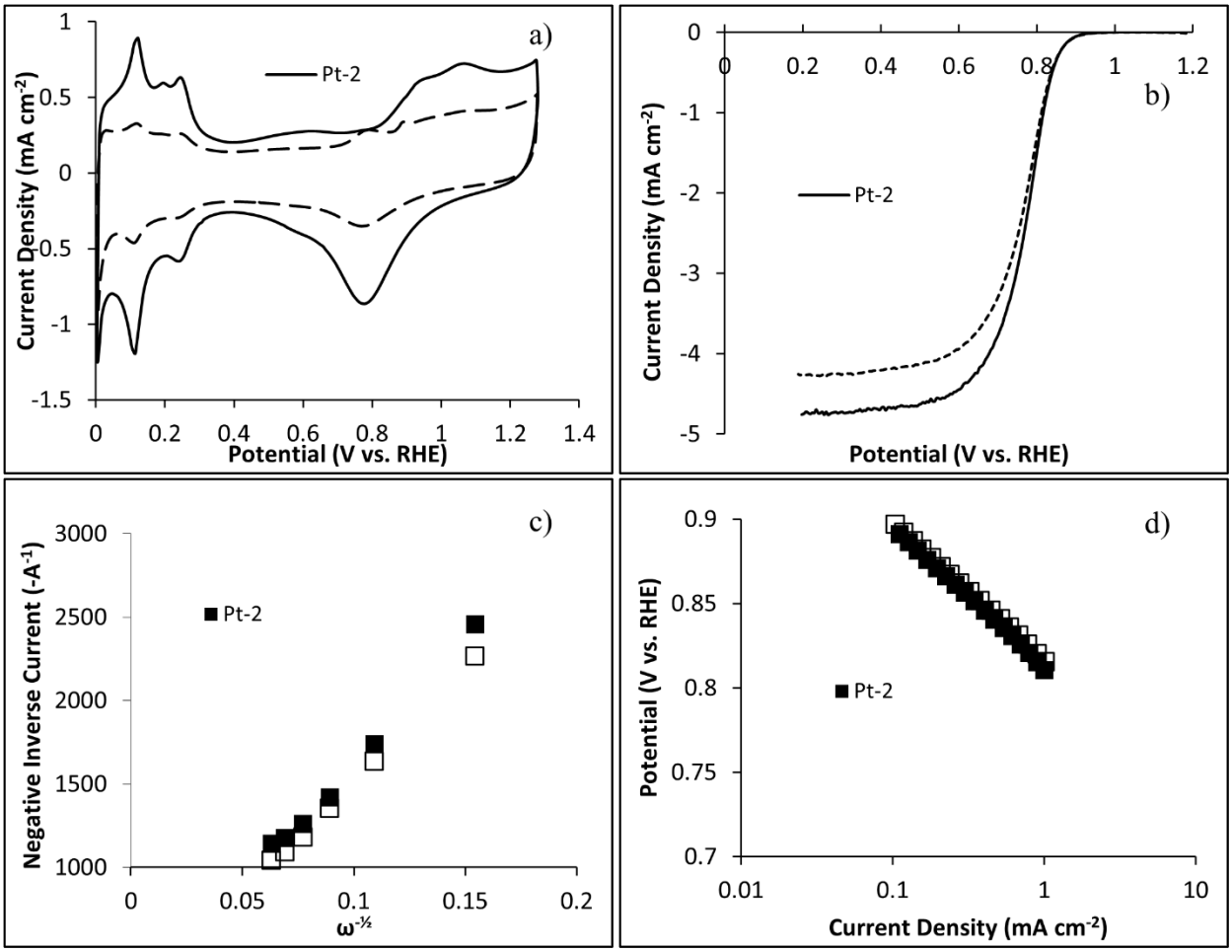

Figure 2. a) CV scans of the catalysts in 0.5 M H_2SO_4 solution at 20 mV s^{-1} under Ar. The solid lines indicate the CFx support; the dashed lines indicate the XC-72R support. b) LSV scan at 1600 RPM for all the catalysts. The solid lines indicate the CFx support; the dashed lines indicate the XC-72R support. c) Koutecky-Levich plot of the catalysts at 0.6 V vs. RHE. The solid markers indicate the CFx support; the hollow markers indicate the XC-72R support. d) The Tafel plot for the catalysts. The solid markers indicate the CFx support; the hollow markers indicate the XC-72R support.

ORR

LSV scans were performed at varying rotation rates from 400 to 2400 RPM to study the ORR kinetics of the catalysts and shown in Figure S8a-h. Figure 2b shows the LSV plots for the Pt2-F and Pt-2C catalyst while Figure S9b shows the LSV scans for all of the catalysts at 1600 RPM, at which most of the subsequent electrochemical measurements were carried out. The onset potential and limiting current densities of the LSV scans are reported in Table 1. Figure S12 shows

a close up of Figure 2b and Figure S9b to differentiate between the slight differences in onset potential for the catalysts. There is minimal variation in the onset potential for the LSVs in all of the catalyst samples meaning the CFx support has minimal synergistic effects on the intrinsic ORR activities of the platinum catalyst compared to that of the XC-72R throughout the various platinum loadings. The XC-72R supported catalysts displayed a slight increase in limiting current density as the platinum loadings increase. This stems from the overall increase in particle sizes reported in previous studies [51,52]. It has also been previously reported that at higher loadings of platinum on carbon, the smaller particle sizes have greater mass and specific activity for ORR [53]. The general trend for the CFx supported catalysts, however, indicates a decrease in limiting current density with the increase in platinum loadings. This could be due to the oxygen dispersion properties (mass transport) of the CFx support. At lower loadings, there is a higher amount of CFx in the catalyst to better disperse the oxygen to the platinum nanoparticles while at the higher loadings (especially that of Pt-4F) the effect of CFx is less pronounced in comparison. Furthermore, the lower ECSA as Pt loading increases on the CFx results in lower active sites for ORR. Moreover,

From the LSVs, a Koutecky-Levich plot was created by plotting the negative inverse limiting current against the negative square root of the rotation rate of the RDE, shown in Figure 2c for the Pt2-F and Pt2-C catalysts and in FigureS10a for all the catalysts. From the slopes of the lines, the Koutecky-Levich equation (equation 4) was used to calculate the electron number [54]:

$$\frac{1}{I} = \frac{1}{I_k} + \frac{1}{I_d} = \frac{1}{I_k} + \frac{1}{0.62nFAD_{O_2}^{2/3}\nu^{-1/6}C_{O_2}\omega^{1/2}} \quad (4)$$

where I is the measured current, I_k is the kinetic limitation current, I_d is the diffusion limitation current, n is the electron transfer number, F is the Faraday constant, A is the electrode area, D_{O2} is

the diffusion coefficient of oxygen in the bulk phase, v is the kinematic viscosity of the solution, C_{O2} is the concentration of oxygen in the bulk phase, and ω is the rotation rate in rad s^{-1}. The corresponding average electron transfer numbers, n, are reported in Table 1. The electron transfer numbers for the catalysts are very close to 4, signifying a general 4 e^- transfer process as was reported in our previous study [39]. The electron transfer numbers for the XC-72R catalysts are slightly lower than that of the CFx catalysts but still resemble an overall 4e^- process.

Tafel plots are displayed in Figure 2d for the Pt2-F and Pt2-C catalysts and in Figure S10b for all the catalysts with the calculated slopes in Table 1. The Tafel slopes for the CFx catalysts increase as the platinum loading increases. This was previously reported by Banham et al. and is due to the larger potential drop through the pores which increases the Tafel slope [55]. The slopes for the XC-72R supported catalysts also increase as the loadings increase except for the Pt-1C sample. At each of the loadings, the Tafel slope for the XC-72R catalysts is lower than that of the CFx catalysts signifying higher intrinsic reaction kinetics at low overpotentials and current densities [56]. All of the slopes are relatively close to the accepted values of -60 mV dec^{-1} for platinum in the acidic media [20,57]. The overpotentials of the CFx supported catalysts also increase with increasing platinum loadings. The fluorination of the carbon support seems to slightly hinder the ORR activity at low current densities in the Tafel region. Chronoamperommetries were also run and are shown in Figure S13. Each of the catalysts displays around the same slope of current decay meaning that the long-term stabilities of the catalysts are similar and the fluorination of the carbon support has minimal effect on the overall stability at constant current. Furthermore, due to the increased ORR catalytic activity of the Pt-2 catalyst its stability was studied further. Start-stop experiments were conducted in the potential window of 1.0 V to 1.5 V vs. RHE and the ECSA as well as the LSV experiments were obtained before and after

the start-stop experiment. The current density of the LSVs after the start-stop for the nonfluorinated carbon support were similar to the initial values, whereas the CFx supported catalyst displayed a slight increase in the current density (Figure 3a). Further, the ECSA of the XC-72R supported catalyst had a slight decrease whereas the CFx supported catalyst displayed an increase. Furthermore, the stability was observed by cycling the catalyst in the potential window of 0.46 V to 0.95 V vs. RHE under a flow of O_2 for 3000 cycles. A negative potential shift in the onset potential is seen in both catalysts, likely due to catalyst agglomeration, however the CFx supported catalyst did not decrease in current density, whereas with the XC-72R catalyst the current density decreased significantly. Furthermore, the ECSA in both catalysts decreased however, the CFx catalyst had a loss of less than 20% of the original ECSA whereas the XC-72R catalyst decreased by nearly 80% of the initial ECSA. The improved stability of fluorinated carbons arises from improved interaction between the metal and the carbon support and mitigation of carbon corrosion due to the presence of C-F bonds, as opposed to only C-C and C-O bonds in the XC-72R catalyst [41,42]. The free dangling groups of carbon supports are often the most prone to corrosion and it has been shown that the C-F bonds formed on these free dangling groups result in a more robust support. Moreover, the metal to support interaction has been shown to increase with heteroatom doped carbons, which further improves the stability of the catalyst [40,42,48]. EDS mapping of the catalysts were obtained prior to and after the stability experiments (Figure S14). From the figure, we can see that there is no change in the elemental distribution for the CFx supported catalyst, except for sulfur present from the sulfuric acid electrolyte. For the XC-72R supported catalyst there is a larger presence of sulfur and oxygen, the larger presence of oxygen indicates corrosion of the carbon. Moreover, there is some fluorine present with the XC-72R supported catalyst due to the Nafion added when making the catalyst inks. To further asses the differences,

TEM micrographs of the catalysts after the stability experiments were obtained (Figure S15). From the figure, we can see that there is a change in the particle size of the Pt for both catalysts. However, the agglomeration and increase in particle size is more prominent in the XC-72R supported Pt. The CFx supported Pt has more particles that remained similar in size to before the stability experiments and this arises from the improved interaction between the Pt and support as shown previously involving a charge transfer between Pt and the fluorinated support resulting in improved stability [42].

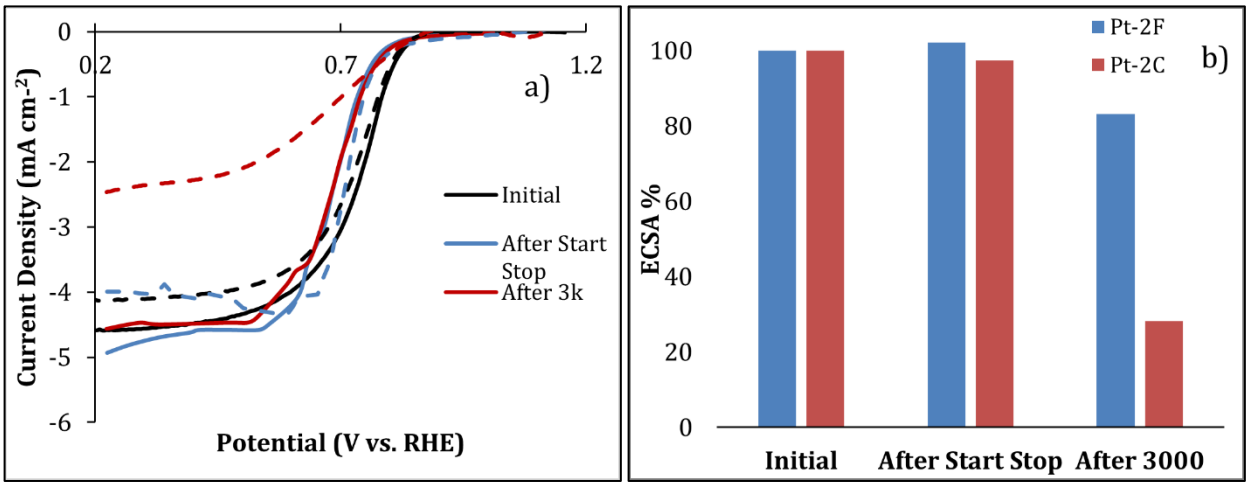

Figure 3. a) LSV scans before and after stability experiments at scan rate of 5 mV s^{-} at 1600 RPM. The solid lines indicate the CFx support; the dashed lines indicate the XC-72R support. b) Change in ECSA after start stop and 3000 cycles.

Table 1. Summary of the half-cell ORR electrochemical tests.

Catalyst	ECSA (H-Adsorp) (m^2 g^{-1} Pt)	ECSA (CO-Strip) (m^2 g^{-1} Pt)	Onset Potential (V vs. RHE)	Limiting Current (mA cm^{-2})	Electron Trans.	Tafel Slope (mV dec^{-1})
Pt-1F	74.55	103.71	0.88±0.02	4.49±0.09	3.97±0.02	-77±4
Pt-1C	51.89	59.30	0.88±0.03	4.17±0.54	3.84±0.08	-83±4
Pt-2F	44.26	60.33	0.90±0.03	4.36±0.13	3.95±0.04	-81±4
Pt-2C	33.48	45.52	0.88±0.01	4.31±0.23	3.79±0.03	-75±10
Pt-3F	20.04	24.85	0.89±0.03	4.32±0.39	3.97±0.01	-88±7
Pt-3C	35.01	42.80	0.89±0.02	4.10±0.05	3.63±0.05	-78±4
Pt-4F	14.27	16.73	0.86±0.01	3.89±0.12	3.58±0.21	-91±6
Pt-4C	25.49	31.40	0.90±0.01	4.39±0.21	3.85±0.01	-83±9

HOR

Following the improvement in ORR activity, the catalyst was also screened for HOR activity. Given the highest activity for ORR the Pt-2 series catalysts were also used for HOR as well as the Pt-1 catalyst due to the higher ECSA. As seen in Figure 4a the LSVs of the catalysts under H_2 saturated electrolyte solution, the CFx supported catalyst show slightly higher current densities than the XC-72R supported catalysts, while the Pt-1F catalyst displays the highest current density of the screened catalysts. The improvement in HOR for the CFx supported catalyst arises from the improved ECSA and could also be due to improved H_2 diffusion. Furthermore, the stability of the catalysts was examined similar to the ORR conditions. Start-stop measurements were completed from the potential window of 0.17 V to -0.27 V vs. RHE. After the start-stop measurement there is a decrease in current density for all catalysts, however the decrease is much more significant for the XC-72R catalysts. Moreover, when observing the ECSA the CFx supported catalysts had a loss between 5-15%, whereas the XC-72R catalysts had a decrease in ECSA between 20-60%. The stability was also examined after 3000 cycles between -0.03 V to 0.22 V vs. RHE, again a decrease in the current density was seen across all the catalysts and more significant in the XC-72R catalyst. Furthermore, the ECSA decreased 50-70% for the XC-72R and 15-30% for the CFx catalysts. Thus, the fluorination of carbon also aids in improving stability of the catalysts under acidic conditions in the hydrogen oxidation region. Moreover, EDS mapping of the catalysts before and after the stability experiments were obtained (Figure S16 and 17). Pt-2C and Pt-1C both show the presence of fluorine from the Nafion added to the catalyst inks. Furthermore, after stability experiments all catalysts display sulfur from the electrolyte. The Pt-2 catalysts both show similar distribution of elements before and after the stability experiments. However, the Pt-2C does display a slightly higher amount of sulfur and oxygen present when

compared to the Pt-2F. Similarly, the Pt-1C displays a larger presence of sulfur and oxygen than the Pt-1F. Furthermore, the Pt-1F catalysts again show minimal differences in the elemental distribution between the initial catalyst and catalyst after stability experiments. TEM micrographs of the catalysts after the stability experiments were also obtained, shown in Figure S18. The Pt-1 catalysts displayed minimal changes in the nanoparticle sizes, although there was more Pt agglomeration seen in the Pt-1C. Moreover, the Pt-2 catalysts displayed significant changes. Pt-2C had a significant increase in Pt agglomeration and size in nanoparticles, whereas the Pt-2F had minor increase in average particle size. The larger difference between the Pt-1 and Pt-2 is due to the amount of Pt present on the carbon supports. With higher Pt loading there is higher propensity for Pt agglomeration and thus the improvement of the Pt stability from CFx is more prominent at higher loadings. Nonetheless, the partial fluorination of carbon also aids in improving stability of the Pt under acidic conditions in the hydrogen oxidation region.

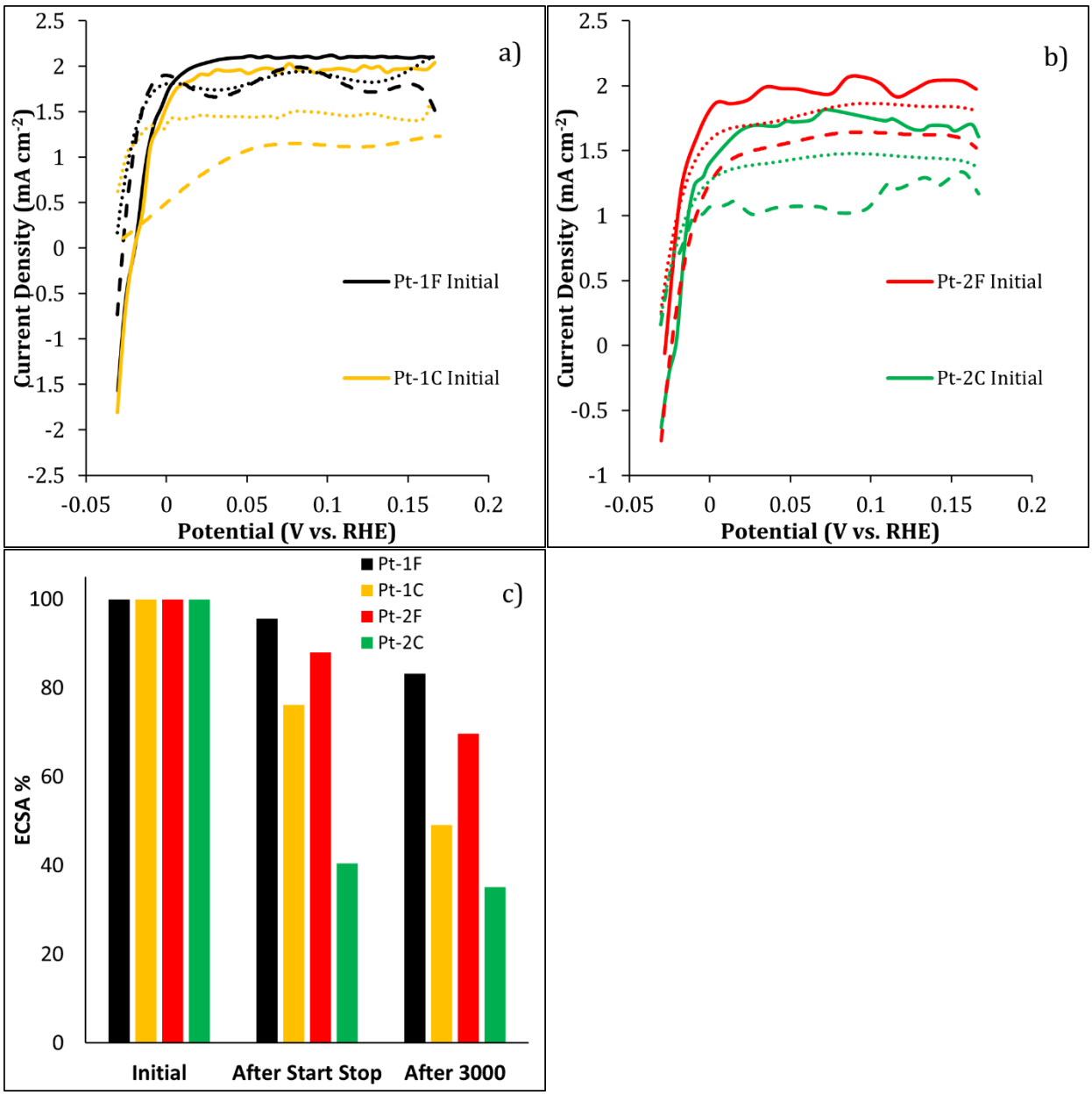

Figure 4. LSV scans of a) Pt-1and b) Pt-2 in 0.5M H_2SO_4 under H_2 gas before and after stability experiments at scan rate of 5 mV s^- at 1600 RPM. The solid lines indicate before stability, the dotted lines indicate after start-stop experiments and the dashed lines indicate after 3000 CV cycles. c) Change in ECSA after start stop and 3000 cycles.

3.2 Fuel Cell Tests

Contact angle measurements of the prepared electrodes were obtained and are shown in Figure S19 and 20, with values of 135.35 ± 3.3, 136.98 ± 5.5, 140.69 ± 3.6 and 144.59 ± 4.2 for Pt-1C, Pt-2C, Pt1F and Pt-2F, respectively. The CFx containing gas diffusion electrodes have a

higher average contact angle measurement, confirming the greater hydrophobicity of the CFx containing electrodes. Polarization curves of the PEM-based hydrogen fuel cells were measured and are shown in Figure 5a at 50 °C and in Figure S20a at ambient temperature (~25 °C) with a summary of the results shown in Table 3. The highest power density achieved was 868 mW cm^{-2} with the CFx supported catalyst compared to 737 mW cm^{-2} for the XC-72R supported catalyst at 50 °C. The CFx supported catalyst shows a 23% and 18% enhancement of peak power density over the XC-72R supported catalyst at ambient temperature and 50 °C, respectively. One reason for this could be the greater oxygen diffusion to the catalyst as well as better water management from the hydrophobicity of the fluorine-doped support. This is a considerable increase in performance from our previous paper at lower temperatures and reactant gas flow rates [39].

EIS spectra were obtained and are shown in Figures 5b and Figure S22b for the fuel cells at 50 °C and 25 °C, respectively, with a summary of the charge transfer resistances reported in Table 3. All of the curves resemble depressed semicircles and were fitted to a circuit shown in Figure S21. From the circuit, L_1 and L_2 represent the inductance of the system arising from the wires and equipment, R_{mem} and R_{ct} represent the membrane and charge transfer resistances respectively, CPE represents the pseudo-capacitive nature of the catalyst layers, and W_s represents the Warburg element for the finite diffusion of reactants and products through the porous catalyst layers. The charge transfer resistances of the MEAs at ambient temperature are higher than those at 50 °C. This is to be expected due to the faster kinetics at elevated temperatures and higher current. Partially fluorinated CFx has been shown to display relatively high conductivity even though there are saturated C-F bonds in the carbon support [39]. The CFx supported catalysts display an 11% decrease in charge transfer resistance at 50 °C. This is due to increased oxygen diffusion and hydrophobicity of the fluorine in the CFx supports [58]. Furthermore, there could

be better synergistic connection between the fluorine backbone of the CFx and the Nafion® ionomer solution ink creating an enhance network to facilitate charge transfer. Another aspect worth mentioning is the high frequency x-intercept, which is indictive of the membrane resistance, R_{mem}, of the MEAs. The R_{mem} of the CFx MEAs is lower than that of the XC-72R MEAs meaning higher conductivity, possibly stemming from better water management at the membrane and catalyst layers from the hydrophobicity of the CFx as well as the triple-phase boundary connection between the catalyst, ionomer, and the membrane.

In order to further test the efficacy of CFx as a platinum catalyst support, CFx was mixed with commercial 40%-wt Pt/C catalyst at varying amounts (which are denoted as Pt-CFx). The polarization curves are shown in Figure S23a for the standard curves and Figure S23b for the normalized curves with respect to the total platinum loading amount in the cathode compartment. The enhancement in performance is evident when the data is normalized to the platinum content at the cathode. The total platinum mass in 40%-wt Pt/C, Pt-CFx 2-1, Pt-CFx 1-1, and Pt-CFx 1-2 is 40wt%, 26.7wt%, 20.0 wt%, and 13.3wt%, respectively. Pt-CFx mixtures of 2-1 and 1-1 exhibit the lowest utilizations, which may be due to a combination of less platinum active sites than commercial Pt/C, and an insufficient amount of CFx present in the matrix to improve mass transport. On the contrary, despite having the least amount of precious metal, Pt-CFx 1-2 exhibits the highest mass specific current and power densities due the presence of excess CFx, which improves oxygen transport and maintains cathodic water at an optimal level.

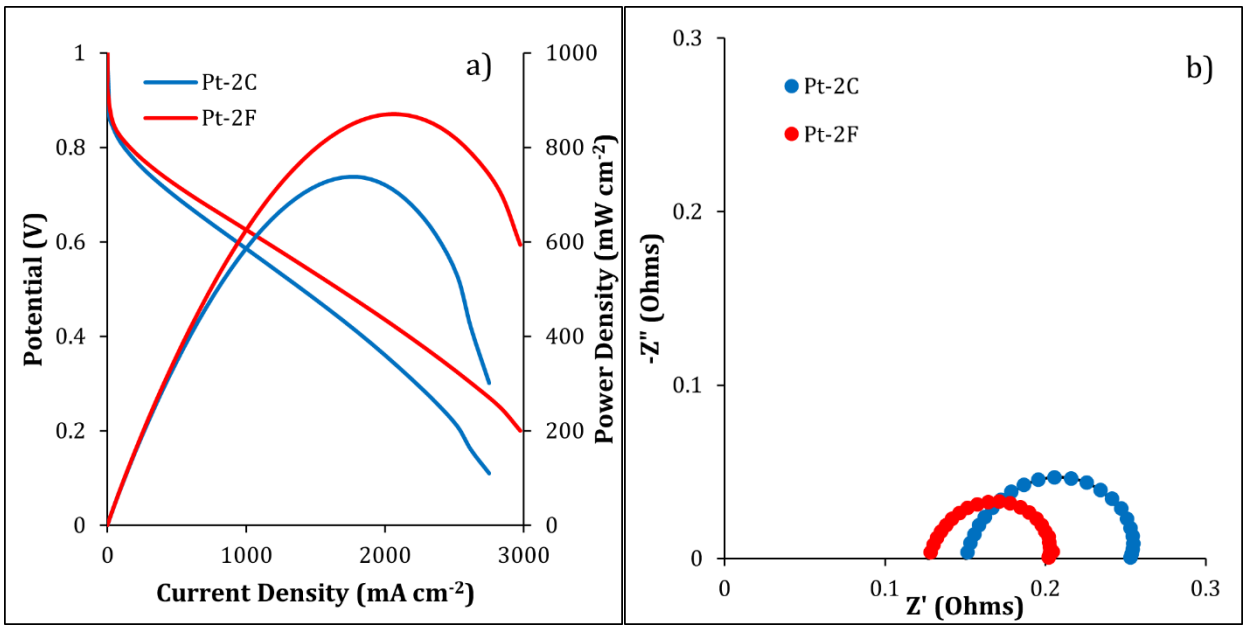

Figure 5. Polarization curves for MEAs with the cathode electrode using the Pt-2 catalyst at: a) 50 °C. b) EIS curves for the Pt-2 catalyst MEAs at 0.4 V vs. reference at 50 °C.

Table 3. Summary of the fuel cell tests for the catalysts.

Anode Electrode	Cathode Electrode	OCV (V)		Peak Power Density (mW cm^{-2})		Charge Transfer Resistance (mΩ)	
		Ambient	50/60 °C	Ambient	50/60 °C	Ambient	50/60 °C
Pt Black	Pt-2C	1.01	1.01	415	737	152	110
Pt Black	Pt-2F	1.00	1.00	510	868	107	83
Pt-2C	Pt/C	1.01	0.977	560	632	202	141
Pt-2F	Pt/C	0.922	0.981	667	820	141	97
Pt-1C	Pt/C	0.937	0.945	780	980	145	95
Pt-1F	Pt/C	0.937	0.952	933	1175	98	66

The Pt-1 and Pt-2 catalysts were further assessed as the anode electrode (Figure 6) in PEMFCs. Here the synthesized catalysts were used as the anode and a commercial Pt/C catalyst was used as the cathode catalyst. With the Pt-1F and Pt-2F catalysts, an increase in peak power densities of 23% and 20%, respectively, was observed at 60 °C when compared to the XC-72R supported catalyst. This increase in power densities could be attributed to the higher ECSA of the CFx support compared to XC-72R as well as better diffusivity of H_2 (improved mass transport). Furthermore, the P-1F catalysts displayed a higher power density than the P-2F, potentially arising

from the higher ECSA and improved Pt utilization. To further understand the differences in catalytic activity, EIS experiments were conducted. Similar to the catalytic studies carried out for ORR, depressed semi-circles were obtained in the Nyquist plots and the same equivalent circuit was used to fit the obtained EIS spectra. There is a 30% decrease in the charge transfer resistance compared to the XC-72R supported catalyst for both the Pt-1 and Pt-2 at 60 °C. Furthermore, there is a decrease in the R_{mem} for CFx supported catalyst compared to the XC-72R supported catalysts, which further indicates an improved triple phase boundary or improved water management leading to higher conductivity.

Furthermore, a PEMFC utilizing CFx supported platinum as both the anode and cathode electrodes was constructed and compared to a PEMFC with XC-72R support for both electrodes in Figure 6c and Figure S25 at 60 °C and 25 °C, respectively. Herein, Pt-1 and Pt-2 were used as the anode and cathode electrodes, respectively. Similarly, we see an increase in peak power density of 20% when using the CFx support compared to the XC-72R supported PEMFC. Therefore, the hydrophobicity of the CFx aids in mitigating catalyst flooding but still allows for proper hydration of the membrane to maintain high ionic conductivity. Moreover, stability experiments were conducted holding the PEMFCs at constant currents of 200 mA/cm^2 and 1A/cm^2 shown in Figure S26. Both MEAs displayed no change in the potential while holding the current at 200 mA/cm^2, however at 1 A/cm^2 there was a slight decrease in the potential and the XC-72R supported catalysts showed large fluctuations throughout the allotted time. Moreover, polarization curves of the PEMFCs after the stability experiments were obtained and a reverse scan was done in the mass transport loss region (Figure 6d). The MEA with CFx supported catalysts displayed minimal change in performance in the reverse scan, whereas the XC-72R supported catalyst displayed a larger decrease in performance. The minimal difference in performance for the MEA with CFx

likely arises from improved water management from the hydrophobicity of the CFx supported catalyst, thus showing the benefits of utilizing CFx for both anode and cathode electrodes.

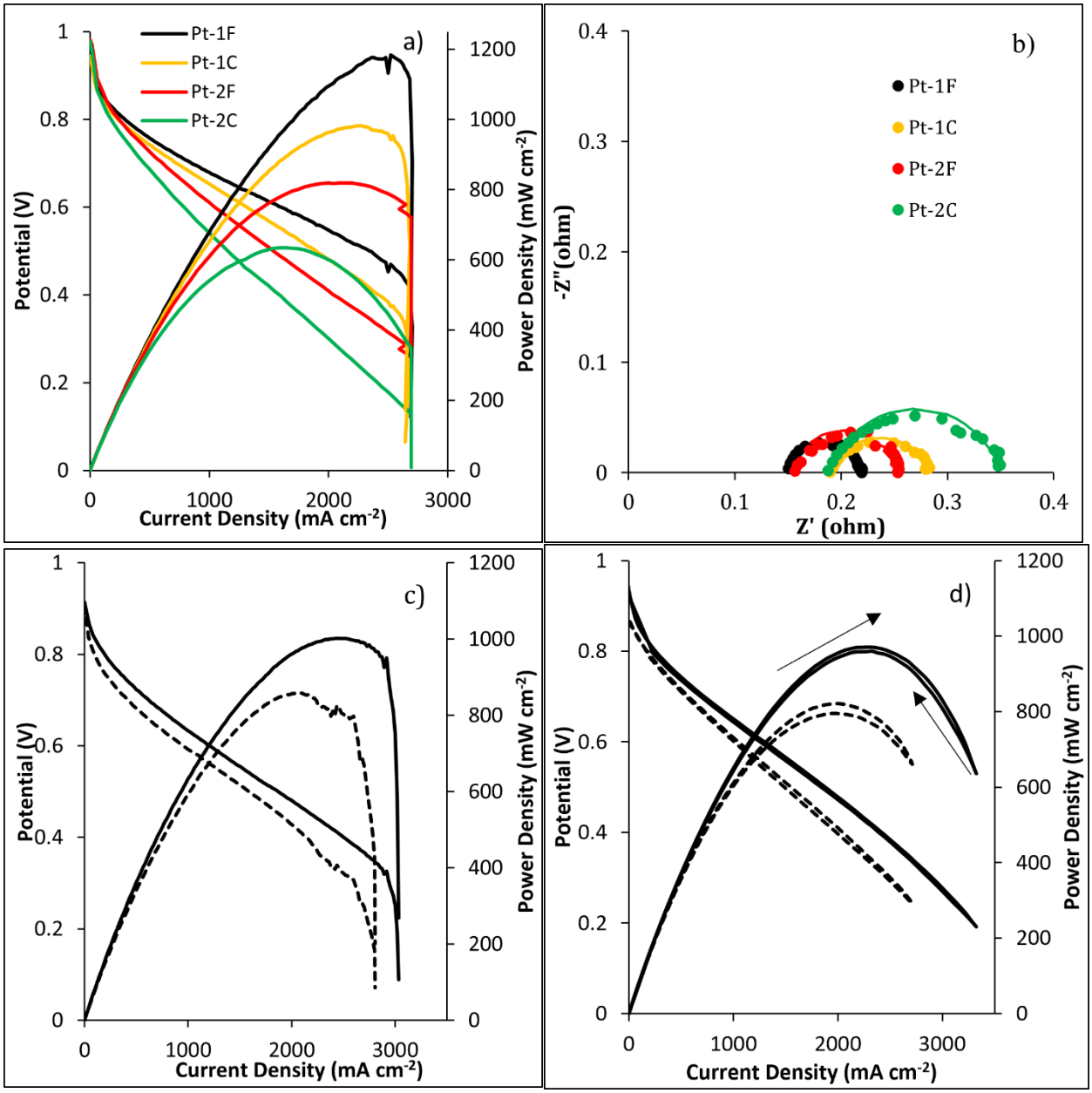

Figure 6. Polarization curves for the Pt-1, Pt-2 anode catalyst MEAs at: a) 60 °C. b) EIS curves for the Pt-1 and Pt-2 catalyst MEAs at 0.4 V vs. reference at 60 °C. c) Polarization curves for the MEAs with Pt-1 anode and Pt-2 cathode electrodes at 60 °C. d) Polarization curves with Pt-1 anode and Pt-2 cathode electrodes after stability experiments with a forward and reverse scan. Solid lines indicate CFx supported and dashed lines indicate XC-72R supported catalyst.

4. Conclusions

When screening catalysts for use in fuel cells and other applications, other factors must be considered outside of the catalyst size, morphology, support etc. Previous studies have shown that the larger the particle size of the catalyst, particularly platinum, the greater the specific ORR activity. This is not always the case as was demonstrated in this study with the partially fluorinated carbon, CFx, supported platinum catalysts. At each of the loadings, the platinum particle size was smaller on the CFx support, yet many of the platinum loadings had higher specific ORR activities compared to the XC-72R support. One of the aspects of half-cell and fuel cell testing that is overlooked is the interaction of the catalyst with the ionomer in the electrode preparation. This aspect can affect the overall properties of the catalyst layer and performance of the MEA. It is evident that there is a greater symbiotic effect of the fluorinated carbon backbone from the CFx that allows better catalyst-ionomer dispersion and intercalation than with the non-fluorinated carbon backbone of XC-72R. This was shown to translate into higher PEM-based hydrogen fuel cell performances and lower charge transfer and membrane resistances.

Acknowledgements

The authors wish to thank the Loker Hydrocarbon Research Institute for funding and Dr. Ian McFarlane and Dr. Rohan Dhall of the Center for Microscopy and Microanalysis (CEMMA) for their assistance on the SEM and TEM, respectively. We would like to thank the National Science Foundation (award: CHE-2018740) for the purchase of the diffractometer used to obtain the powder X-ray diffraction patterns reported here.

References

[1] E.P. Randviir, C.E. Banks, The Oxygen Reduction Reaction at Graphene Modified

Electrodes, Electroanalysis. 26 (2014) 76–83. doi:10.1002/elan.201300477.
[2] H.A. Gasteiger, S.S. Kocha, B. Sompalli, F.T. Wagner, Activity benchmarks and requirements for Pt, Pt-alloy, and non-Pt oxygen reduction catalysts for PEMFCs, Appl. Catal. B Environ. 56 (2005) 9–35. doi:10.1016/j.apcatb.2004.06.021.
[3] F. Jaouen, J.-P. Dodelet, O_2 Reduction Mechanism on Non-Noble Metal Catalysts for PEM Fuel Cells. Part I: Experimental Rates of O_2 Electroreduction, H_2O_2 Electroreduction, and H_2O_2 Disproportionation, J. Phys. Chem. C. 113 (2009) 15422–15432. doi:10.1021/jp900837e.
[4] D.E. Curtin, R.D. Lousenberg, T.J. Henry, P.C. Tangeman, M.E. Tisack, Advanced materials for improved PEMFC performance and life, J. Power Sources. 131 (2004) 41–48. doi:10.1016/j.jpowsour.2004.01.023.
[5] H. Li, Y. Tang, Z. Wang, Z. Shi, S. Wu, D. Song, J. Zhang, K. Fatih, J. Zhang, H. Wang, Z. Liu, R. Abouatallah, A. Mazza, A review of water flooding issues in the proton exchange membrane fuel cell, J. Power Sources. 178 (2008) 103–117. doi:10.1016/j.jpowsour.2007.12.068.
[6] G. Velayutham, J. Kaushik, N. Rajalakshmi, K.S. Dhathathreyan, Effect of PTFE Content in Gas Diffusion Media and Microlayer on the Performance of PEMFC Tested under Ambient Pressure, Fuel Cells. 7 (2007) 314–318. doi:10.1002/fuce.200600032.
[7] X. Li, I. Sabir, J. Park, A flow channel design procedure for PEM fuel cells with effective water removal, J. Power Sources. 163 (2007) 933–942. doi:10.1016/j.jpowsour.2006.10.015.
[8] C. Cadet, S. Jemeï, F. Druart, D. Hissel, Diagnostic tools for PEMFCs: from conception to implementation, Int. J. Hydrogen Energy. 39 (2014) 10613–10626. doi:10.1016/j.ijhydene.2014.04.163.
[9] * J. K. Nørskov, J. Rossmeisl, and A. Logadottir, L. Lindqvist, J.R. Kitchin, T. Bligaard, H. Jónsson, Origin of the Overpotential for Oxygen Reduction at a Fuel-Cell Cathode, (2004). doi:10.1021/JP047349J.
[10] Z. Mo, S. Liao, Y. Zheng, Z. Fu, Preparation of nitrogen-doped carbon nanotube arrays and their catalysis towards cathodic oxygen reduction in acidic and alkaline media, Carbon N. Y. 50 (2012) 2620–2627. doi:10.1016/j.carbon.2012.02.021.
[11] D.Y. Chung, H. Kim, Y.-H. Chung, M.J. Lee, S.J. Yoo, A.D. Bokare, W. Choi, Y.-E. Sung, Inhibition of CO poisoning on Pt catalyst coupled with the reduction of toxic hexavalent chromium in a dual-functional fuel cell., Sci. Rep. 4 (2014) 7450. doi:10.1038/srep07450.
[12] C.A. Rice, P. Urchaga, A.O. Pistono, B.W. McFerrin, B.T. McComb, J. Hu, Platinum Dissolution in Fuel Cell Electrodes: Enhanced Degradation from Surface Area Assessment in Automotive Accelerated Stress Tests, J. Electrochem. Soc. 162 (2015) F1175–F1180. doi:10.1149/2.0371510jes.
[13] D.E. Glass, G.A. Olah, G.K.S. Prakash, Effect of the thickness of the anode electrode catalyst layers on the performance in direct methanol fuel cells, J. Power Sources. 352 (2017) 165–173. doi:10.1016/j.jpowsour.2017.03.106.
[14] J. Zhang, † F. H. B. Lima, M. H. Shao, K. Sasaki, J. X. Wang, and J. Hanson, R.R. Adzic*, Platinum Monolayer on Nonnoble Metal−Noble Metal Core−Shell Nanoparticle Electrocatalysts for O2 Reduction, (2005). doi:10.1021/JP055634C.
[15] L. Gan, M. Heggen, S. Rudi, P. Strasser, Core–Shell Compositional Fine Structures of Dealloyed Pt_xNi_{1-x} Nanoparticles and Their Impact on Oxygen Reduction Catalysis,

Nano Lett. 12 (2012) 5423–5430. doi:10.1021/nl302995z.
[16] K.-S. Lee, H.-Y. Park, H.C. Ham, S.J. Yoo, H.J. Kim, E. Cho, A. Manthiram, J.H. Jang, Reversible Surface Segregation of Pt in a Pt_3Au/C Catalyst and Its Effect on the Oxygen Reduction Reaction, J. Phys. Chem. C. 117 (2013) 9164–9170. doi:10.1021/jp403135k.
[17] M. Ammam, E.B. Easton, Oxygen reduction activity of binary PtMn/C, ternary PtMnX/C (X = Fe, Co, Ni, Cu, Mo and, Sn) and quaternary PtMnCuX/C (X = Fe, Co, Ni, and Sn) and PtMnMoX/C (X = Fe, Co, Ni, Cu and Sn) alloy catalysts, J. Power Sources. 236 (2013) 311–320. doi:10.1016/j.jpowsour.2013.02.029.
[18] Y. Luo, N. Alonso-Vante, The Effect of Support on Advanced Pt-based Cathodes towards the Oxygen Reduction Reaction. State of the Art, Electrochim. Acta. 179 (2015) 108–118. doi:10.1016/j.electacta.2015.04.098.
[19] A. Pozio, M. De Francesco, A. Cemmi, F. Cardellini, L. Giorgi, Comparison of high surface Pt/C catalysts by cyclic voltammetry, J. Power Sources. 105 (2002) 13–19. doi:10.1016/S0378-7753(01)00921-1.
[20] B.B. Xiao, X.Y. Lang, Q. Jiang, Pt monatomic wire supported on graphene nanoribbon for oxygen reduction reaction, RSC Adv. 4 (2014) 28400–28408. doi:10.1039/c4ra03387f.
[21] Z. Liu, J. Qu, X. Fu, Q. Wang, G. Zhong, F. Peng, Low Pt content catalyst supported on nitrogen and phosphorus-codoped carbon nanotubes for electrocatalytic O2 reaction in acidic medium, 2015. doi:10.1016/j.matlet.2014.12.011.
[22] C. Alegre, D. Sebastián, E. Baquedano, M.E. Gálvez, R. Moliner, M. Lázaro, Tailoring Synthesis Conditions of Carbon Xerogels towards Their Utilization as Pt-Catalyst Supports for Oxygen Reduction Reaction (ORR), Catalysts. 2 (2012) 466–489. doi:10.3390/catal2040466.
[23] J.-H. Kim, G. Kwon, H. Chun, Y.-T. Kim, Enhancement of Activity and Durability through Cr Doping of TiO_2 Supports in Pt Electrocatalysts for Oxygen Reduction Reactions, ChemCatChem. 6 (2014) 3239–3245. doi:10.1002/cctc.201402466.
[24] Y. Tian, Y. Liu, J. Zhao, Y. Ding, High stability and superior catalytic reactivity of nitrogen-doped graphene supporting Pt nanoparticles as a catalyst for the oxygen reduction reaction: a density functional theory study, RSC Adv. 5 (2015) 34070–34077. doi:10.1039/C5RA02585K.
[25] Q. Zhang, S. D'Astorg, P. Xiao, X. Zhang, L. Lu, Carbon-coated fluorinated graphite for high energy and high power densities primary lithium batteries, 2010. doi:10.1016/j.jpowsour.2009.10.096.
[26] Y. Tian, H. Yue, Z. Gong, Y. Yang, Enhanced electrochemical performance of fluorinated carbon nanotube as cathode for Li–O2 primary batteries, Electrochim. Acta. 90 (2013) 186–193. doi:10.1016/j.electacta.2012.12.008.
[27] R. Jayasinghe, A.K. Thapa, R.R. Dharmasena, T.Q. Nguyen, B.K. Pradhan, H.S. Paudel, J.B. Jasinski, A. Sherehiy, M. Yoshio, G.U. Sumanasekera, Optimization of Multi-Walled Carbon Nanotube based CFx electrodes for improved primary and secondary battery performances, J. Power Sources. 253 (2014) 404–411. doi:10.1016/j.jpowsour.2013.12.076.
[28] T. Nakajima, M. Koh, R.N. Singh, M. Shimada, Electrochemical behavior of surface-fluorinated graphite, Electrochim. Acta. 44 (1999) 2879–2888. doi:10.1016/S0013-4686(99)00048-1.
[29] V. Gupta, T. Nakajima, Y. Ohzawa, H. Iwata, Electrochemical characteristics and structures of surface-fluorinated graphites with different particle sizes for lithium ion

secondary batteries, J. Fluor. Chem. 112 (2001) 233–240. doi:10.1016/S0022-1139(01)00517-6.
[30] X. Sun, P. Song, T. Chen, J. Liu, W. Xu, Fluorine-doped BP 2000: highly efficient metal-free electrocatalysts for acidic oxygen reduction reaction with superlow H2O2 yield, Chem. Commun. 49 (2013) 10296. doi:10.1039/c3cc45480k.
[31] X. Sun, Y. Zhang, P. Song, J. Pan, L. Zhuang, W. Xu, W. Xing, Fluorine-Doped Carbon Blacks: Highly Efficient Metal-Free Electrocatalysts for Oxygen Reduction Reaction, ACS Catal. 3 (2013) 1726–1729. doi:10.1021/cs400374k.
[32] X. Zhang, Y. Chen, J. Wang, Q. Zhong, Nitrogen and fluorine dual-doped carbon black as an efficient cathode catalyst for oxygen reduction reaction in neutral medium, ChemistrySelect. 1 (2016) 696–702. doi:10.1002/slct.201600144.
[33] K. Meng, Q. Liu, Y. Huang, Y. Wang, Facile synthesis of nitrogen and fluorine co-doped carbon materials as efficient electrocatalysts for oxygen reduction reactions in air-cathode microbial fuel cells, J. Mater. Chem. A. 3 (2015) 6873–6877. doi:10.1039/C4TA06500J.
[34] S. Jiang, Y. Sun, H. Dai, J. Hu, P. Ni, Y. Wang, Z. Li, Z. Li, Nitrogen and fluorine dual-doped mesoporous graphene: a high-performance metal-free ORR electrocatalyst with a super-low HO_2^- yield, Nanoscale. 7 (2015) 10584–10589. doi:10.1039/C5NR01793A.
[35] G. Panomsuwan, N. Saito, T. Ishizaki, Simple one-step synthesis of fluorine-doped carbon nanoparticles as potential alternative metal-free electrocatalysts for oxygen reduction reaction, J. Mater. Chem. A. 3 (2015) 9972–9981. doi:10.1039/C5TA00244C.
[36] K. Kakaei, A. Balavandi, Synthesis of halogen-doped reduced graphene oxide nanosheets as highly efficient metal-free electrocatalyst for oxygen reduction reaction, J. Colloid Interface Sci. 463 (2016) 46–54. doi:10.1016/j.jcis.2015.10.030.
[37] H. Shioyama, K. Honjo, M. Kiuchi, Y. Yamada, A. Ueda, N. Kuriyama, T. Kobayashi, C2F6 plasma treatment of a carbon support for a PEM fuel cell electrocatalyst, 2006. doi:10.1016/j.jpowsour.2006.05.046.
[38] S. Berthon-Fabry, L. Dubau, Y. Ahmad, K. Guerin, M. Chatenet, First Insight into Fluorinated Pt/Carbon Aerogels as More Corrosion-Resistant Electrocatalysts for Proton Exchange Membrane Fuel Cell Cathodes, Electrocatalysis. 6 (2015) 521–533. doi:10.1007/s12678-015-0267-9.
[39] F.A. Viva, G.A. Olah, G.K.S. Prakash, Characterization of Pt supported on commercial fluorinated carbon as cathode catalysts for Polymer Electrolyte Membrane Fuel Cell, Int. J. Hydrogen Energy. (2017). doi:10.1016/j.ijhydene.2017.04.255.
[40] T. Asset, R. Chattot, F. Maillard, L. Dubau, Y. Ahmad, N. Batisse, M. Dubois, K. Guérin, F. Labbé, R. Metkemeijer, S. Berthon-Fabry, M. Chatenet, Activity and Durability of Platinum-Based Electrocatalysts Supported on Bare or Fluorinated Nanostructured Carbon Substrates, J. Electrochem. Soc. 165 (2018) F3346–F3358. doi:10.1149/2.031806jes.
[41] J.L. Bott-Neto, T. Asset, F. Maillard, L. Dubau, Y. Ahmad, K. Guérin, S. Berthon-Fabry, A. Mosdale, R. Mosdale, E.A. Ticianelli, M. Chatenet, Utilization of graphitized and fluorinated carbon as platinum nanoparticles supports for application in proton exchange membrane fuel cell cathodes, J. Power Sources. 404 (2018) 28–38. doi:10.1016/j.jpowsour.2018.10.004.
[42] Z. Li, L. Sui, L. Calvillo, N. Alonso-Vante, J. Ma, Strengthening oxygen reduction activity and stability of carbon-supported platinum nanoparticles by fluorination, Electrochim. Acta. 399 (2021) 139409. doi:10.1016/j.electacta.2021.139409.
[43] X. Zhao, W. Li, Y. Fu, A. Manthiram, Influence of ionomer content on the proton

conduction and oxygen transport in the carbon-supported catalyst layers in DMFC, Int. J. Hydrogen Energy. 37 (2012) 9845–9852. doi:10.1016/j.ijhydene.2012.03.107.
[44] S. Rudi, C. Cui, L. Gan, P. Strasser, Comparative Study of the Electrocatalytically Active Surface Areas (ECSAs) of Pt Alloy Nanoparticles Evaluated by Hupd and CO-stripping voltammetry, Electrocatalysis. 5 (2014) 408–418. doi:10.1007/s12678-014-0205-2.
[45] T. Binninger, E. Fabbri, R. Kotz, T.J. Schmidt, Determination of the Electrochemically Active Surface Area of Metal-Oxide Supported Platinum Catalyst, J. Electrochem. Soc. 161 (2013) H121–H128. doi:10.1149/2.055403jes.
[46] K. Yamamoto, T. Imaoka, W.-J. Chun, O. Enoki, H. Katoh, M. Takenaga, A. Sonoi, Size-specific catalytic activity of platinum clusters enhances oxygen reduction reactions, Nat. Chem. 1 (2009) 397–402. doi:10.1038/nchem.288.
[47] Z. Xu, H. Zhang, H. Zhong, Q. Lu, Y. Wang, D. Su, Effect of particle size on the activity and durability of the Pt/C electrocatalyst for proton exchange membrane fuel cells, Appl. Catal. B Environ. 111 (2012) 264–270. doi:10.1016/j.apcatb.2011.10.007.
[48] M. Kato, K. Ogura, S. Nakagawa, S. Tokuda, K. Takahashi, T. Nakamura, I. Yagi, Enhancement of Electrocatalytic Oxygen Reduction Activity and Durability of Pt-Ni Rhombic Dodecahedral Nanoframes by Anchoring to Nitrogen-Doped Carbon Support, ACS Omega. 3 (2018) 9052–9059. doi:10.1021/acsomega.8b01373.
[49] S. Taylor, E. Fabbri, P. Levecque, T.J. Schmidt, O. Conrad, The Effect of Platinum Loading and Surface Morphology on Oxygen Reduction Activity, Electrocatalysis. 7 (2016) 287–296. doi:10.1007/s12678-016-0304-3.
[50] E.G. Ciapina, S.F. Santos, E.R. Gonzalez, Electrochemical CO stripping on nanosized Pt surfaces in acid media: A review on the issue of peak multiplicity, J. Electroanal. Chem. 815 (2018) 47–60. doi:10.1016/j.jelechem.2018.02.047.
[51] S.H. Joo, K. Kwon, D.J. You, C. Pak, H. Chang, J.M. Kim, Preparation of high loading Pt nanoparticles on ordered mesoporous carbon with a controlled Pt size and its effects on oxygen reduction and methanol oxidation reactions, Electrochim. Acta. 54 (2009) 5746–5753. doi:10.1016/j.electacta.2009.05.022.
[52] F.J. Perez-Alonso, D.N. McCarthy, A. Nierhoff, P. Hernandez-Fernandez, C. Strebel, I.E.L. Stephens, J.H. Nielsen, I. Chorkendorff, The Effect of Size on the Oxygen Electroreduction Activity of Mass-Selected Platinum Nanoparticles, Angew. Chemie Int. Ed. 51 (2012) 4641–4643. doi:10.1002/anie.201200586.
[53] S. Li, H. Liu, Y. Wang, W. Xu, J. Li, Y. Liu, X. Guo, Y. Song, Controlled synthesis of high metal-loading, Pt-based electrocatalysts with enhanced activity and durability toward oxygen reduction reaction, RSC Adv. 5 (2015) 8787–8792. doi:10.1039/c4ra16026f.
[54] A. Bayrakçeken, A. Smirnova, U. Kitkamthorn, M. Aindow, L. Türker, İ. Eroğlu, C. Erkey, Pt-based electrocatalysts for polymer electrolyte membrane fuel cells prepared by supercritical deposition technique, J. Power Sources. 179 (2008) 532–540. doi:10.1016/j.jpowsour.2007.12.086.
[55] D.W. Banham, J.N. Soderberg, V.I. Birss, Pt/Carbon Catalyst Layer Microstructural Effects on Measured and Predicted Tafel Slopes for the Oxygen Reduction Reaction, J. Phys. Chem. C. 113 (2009) 10103–10111. doi:10.1021/jp809987g.
[56] W. Bian, Z. Yang, P. Strasser, R. Yang, A CoFe2O4/graphene nanohybrid as an efficient bi-functional electrocatalyst for oxygen reduction and oxygen evolution, J. Power Sources. 250 (2014) 196–203. doi:10.1016/j.jpowsour.2013.11.024.
[57] A. Damjanovic, M.A. Genshaw, J.O. Bockris, The Mechanism of Oxygen Reduction at

Platinum in Alkaline Solutions with Special Reference to H[sub 2]O[sub 2], J. Electrochem. Soc. 114 (1967) 1107. doi:10.1149/1.2426425.
[58] M. Chen, S. Wang, Z. Zou, T. Yuan, Z. Li, D.L. Akins, H. Yang, Fluorination of Vulcan XC-72R for cathodic microporous layer of passive micro direct methanol fuel cell, J. Appl. Electrochem. 40 (2010) 2117–2124. doi:10.1007/s10800-010-0193-8.

Electronic Supplementary Information (ESI)

Optimization of Platinum Loading on Partially Fluorinated Carbon Catalysts for Enhanced Proton Exchange Membrane Fuel Cell Performance

Dean E. Glass, Vicente Galvan, Marc Iulliucci and G. K. Surya Prakash*
Loker Hydrocarbon Research Institute, Department of Chemistry, University of Southern California, 837 Bloom Walk, Los Angeles, CA, 90089
*Corresponding Author: gprakash@usc.edu
Phone: (213) 740-5984
Fax: (213) 740-6679

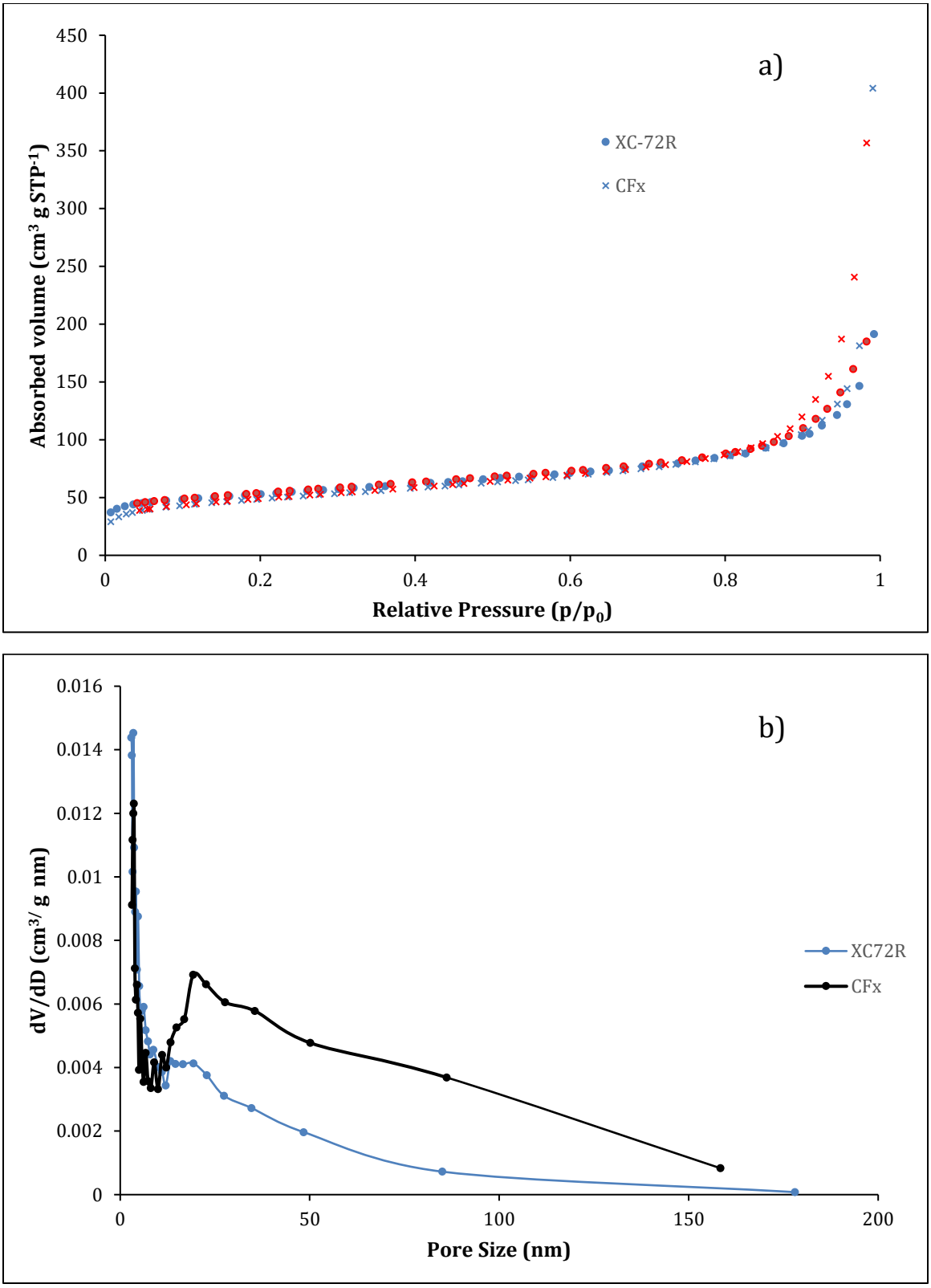

Fig. S1. a) N_2 adsorption-desorption isotherms of XC-72R and CFx and b) corresponding mesoporous size distribution curves for XC-72R and CFx

Table S1. Summary of BET and Pore Volume for the carbon supports

	SA_BET ($m^2 g^{-1}$)	Pore Volume ($cm^3 g^{-1}$)
XC72R	194	0.232
CFx	174	0.574

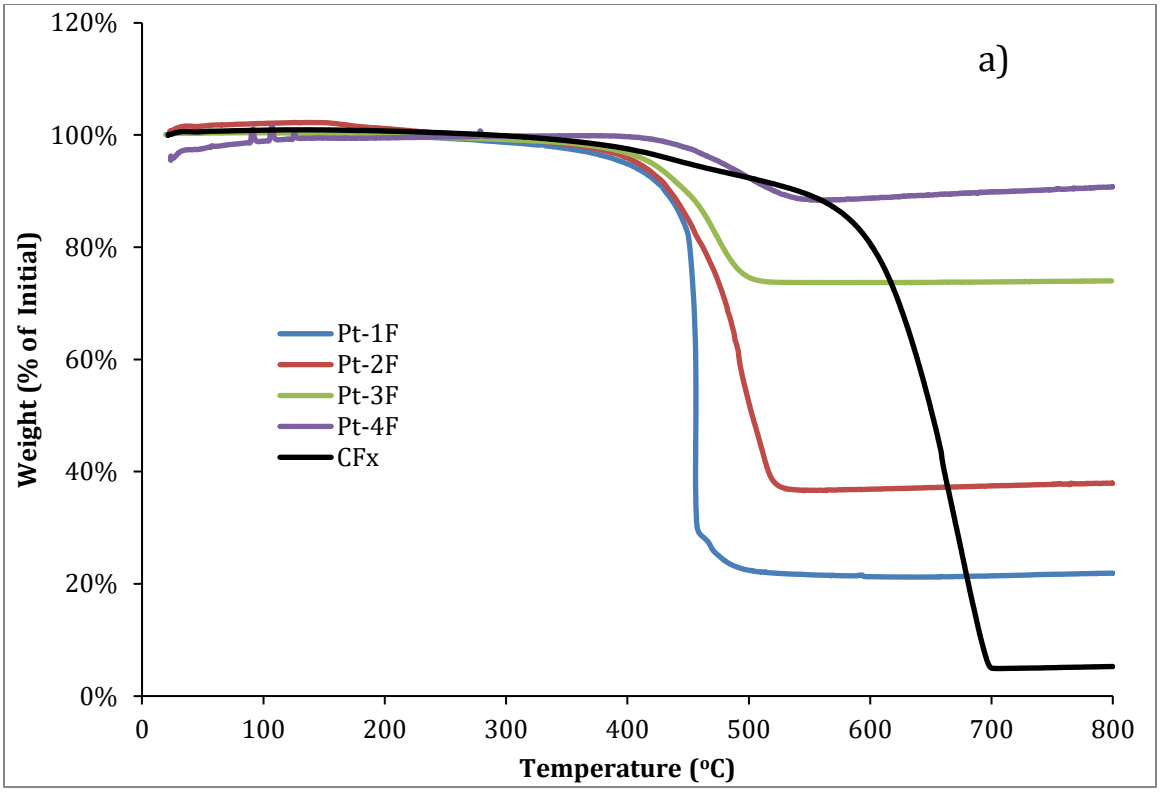
a)
120%
100%
80%
60%
40%
20%
0%
Weight (% of Initial)
0
100
200
300
400
500
600
700
800
Temperature (°C)
Pt-1F
Pt-2F
Pt-3F
Pt-4F
CFx

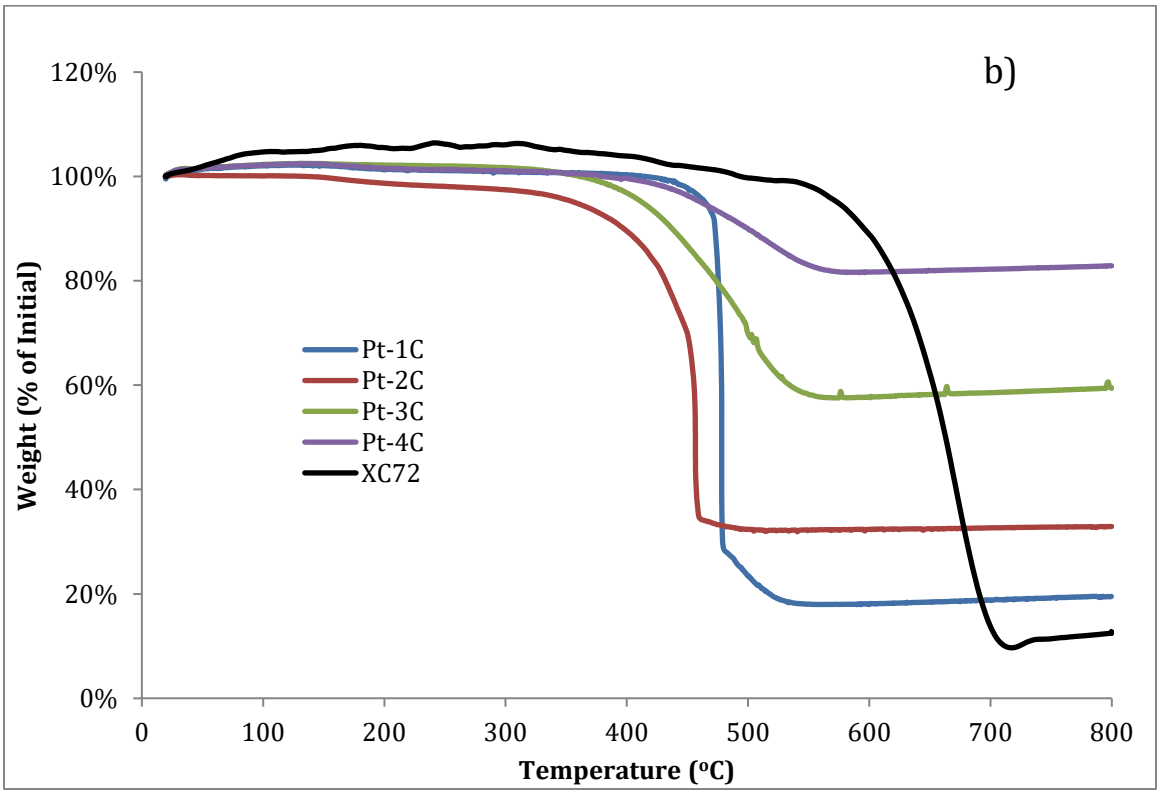
b)
120%
100%
80%
60%
40%
20%
0%
Weight (% of Initial)
0
100
200
300
400
500
600
700
800
Temperature (°C)
Pt-1C
Pt-2C
Pt-3C
Pt-4C
XC72

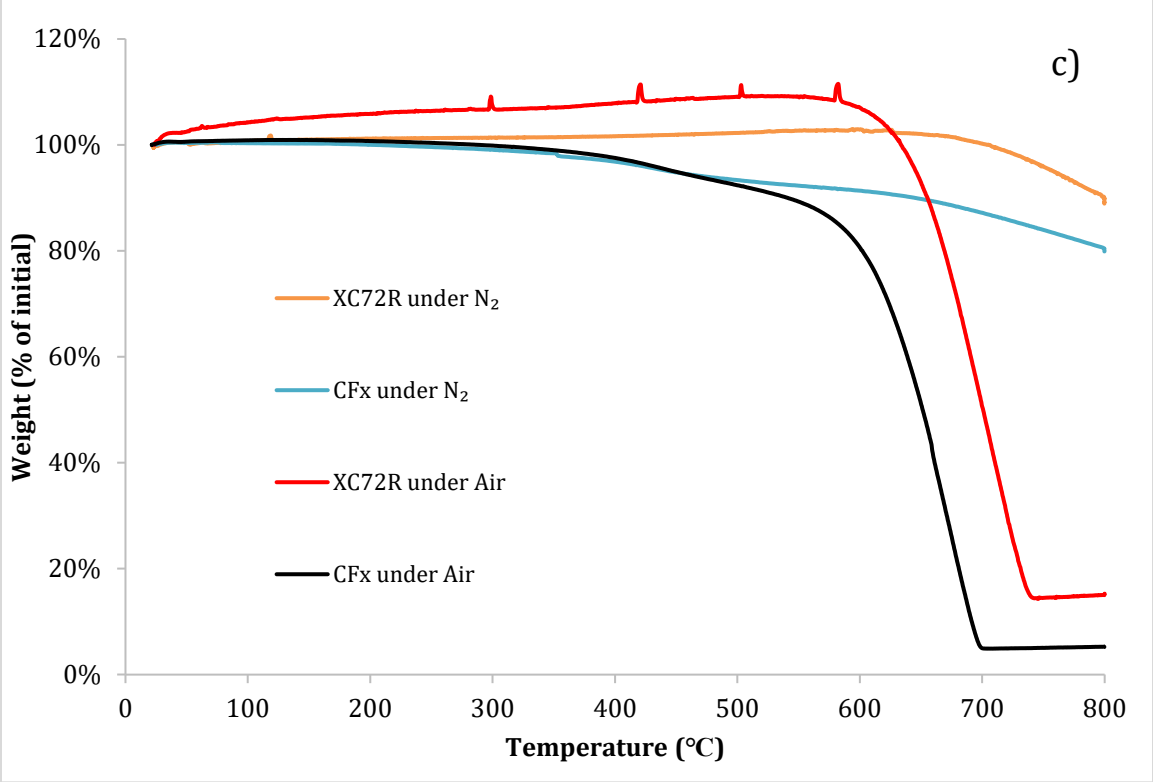

Fig. S2. TGA curves of the impregnated platinum catalysts on: a) CFx; b) XC-72R carbon supports and c) TGA of the CFx and XC72R under inert atmosphere and air.

Table S2. Summary of the TGA results for the platinum loadings of the catalysts.

Catalyst	Pt-1F	Pt-1C	Pt-2F	Pt-2C	Pt-3F	Pt-3C	Pt-4F	Pt-4C
Target Loading	10%	10%	25%	25%	50%	50%	75%	75%
Actual Loading	15.9%	10.3%	30.0%	30.6%	68.4%	49.9%	83.2%	73.8%

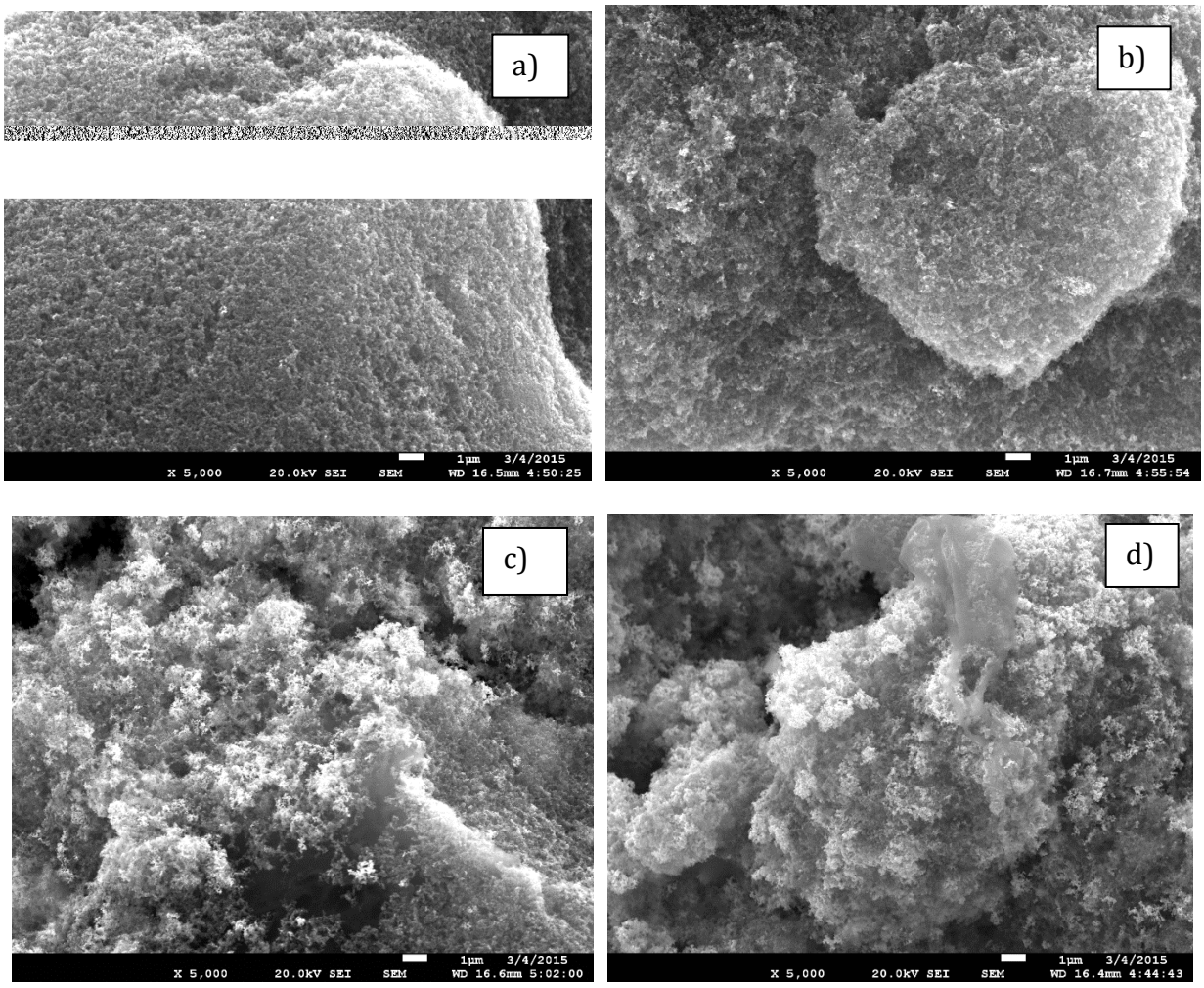

Fig. S3. SEM images of the catalysts: a) Pt-1F; b) Pt-2F; c) Pt-3F; and d) Pt-4F.

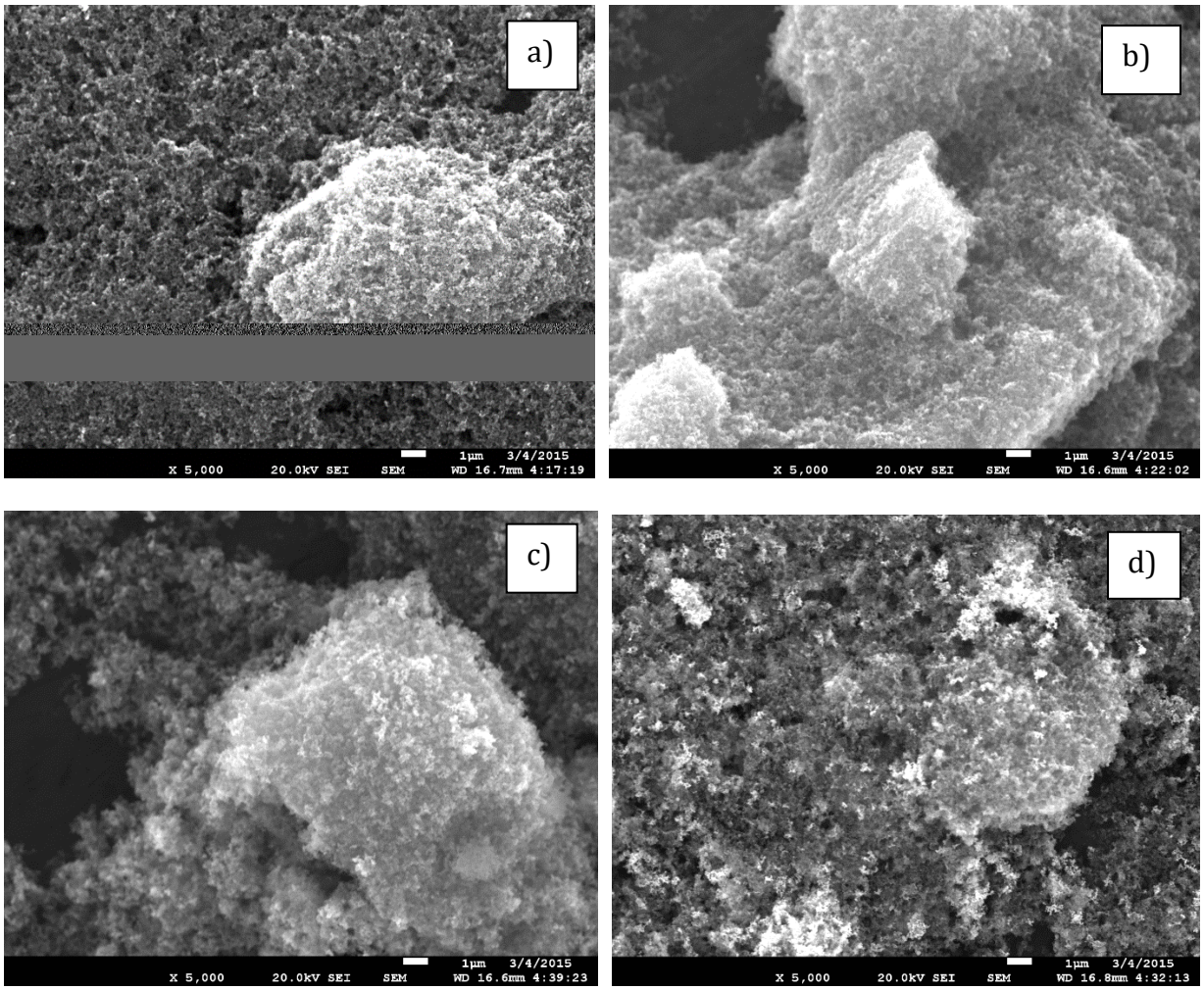

Fig. S4. SEM images of the catalysts: a) Pt-1C; b) Pt-2C; c) Pt-3C; and d) Pt-4C.

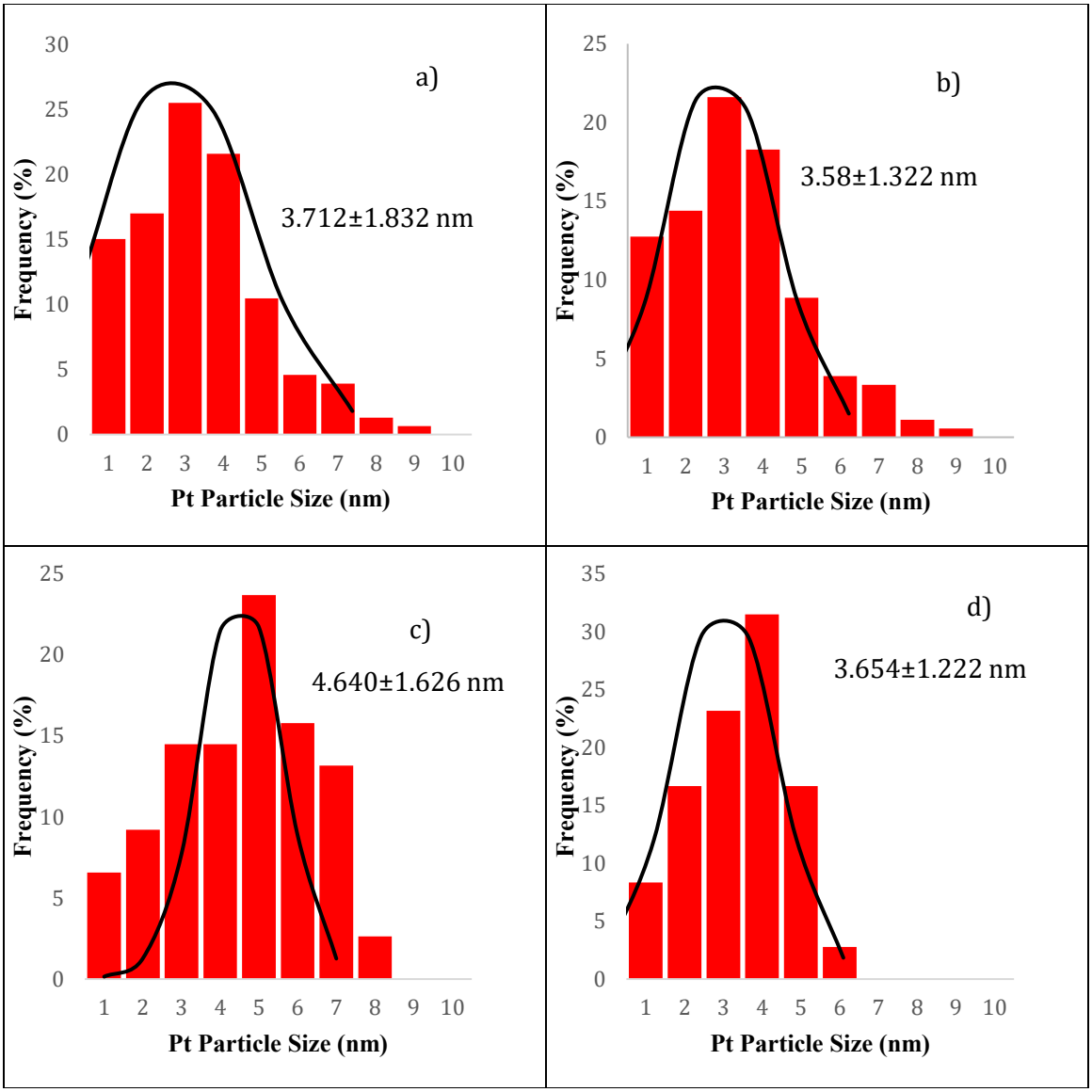

Fig S5. Particle size distributions for the TEM images of: a) Pt-1F; b) Pt-2F; c) Pt-1C and; d) Pt-2C.

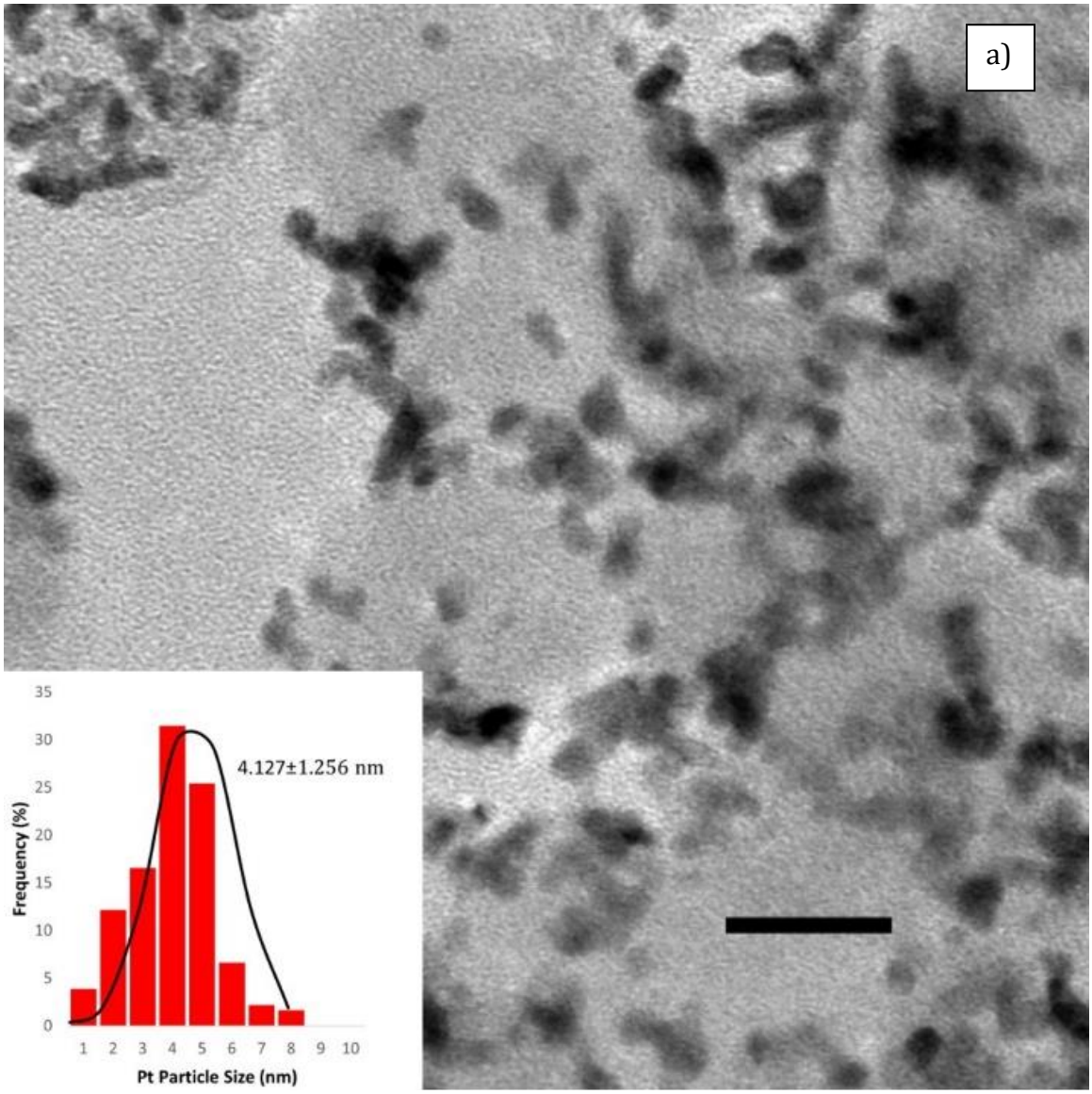
a)
4.127±1.256 nm
Frequency (%)
Pt Particle Size (nm)
0
5
10
15
20
25
30
35
1 2 3 4 5 6 7 8 9 10

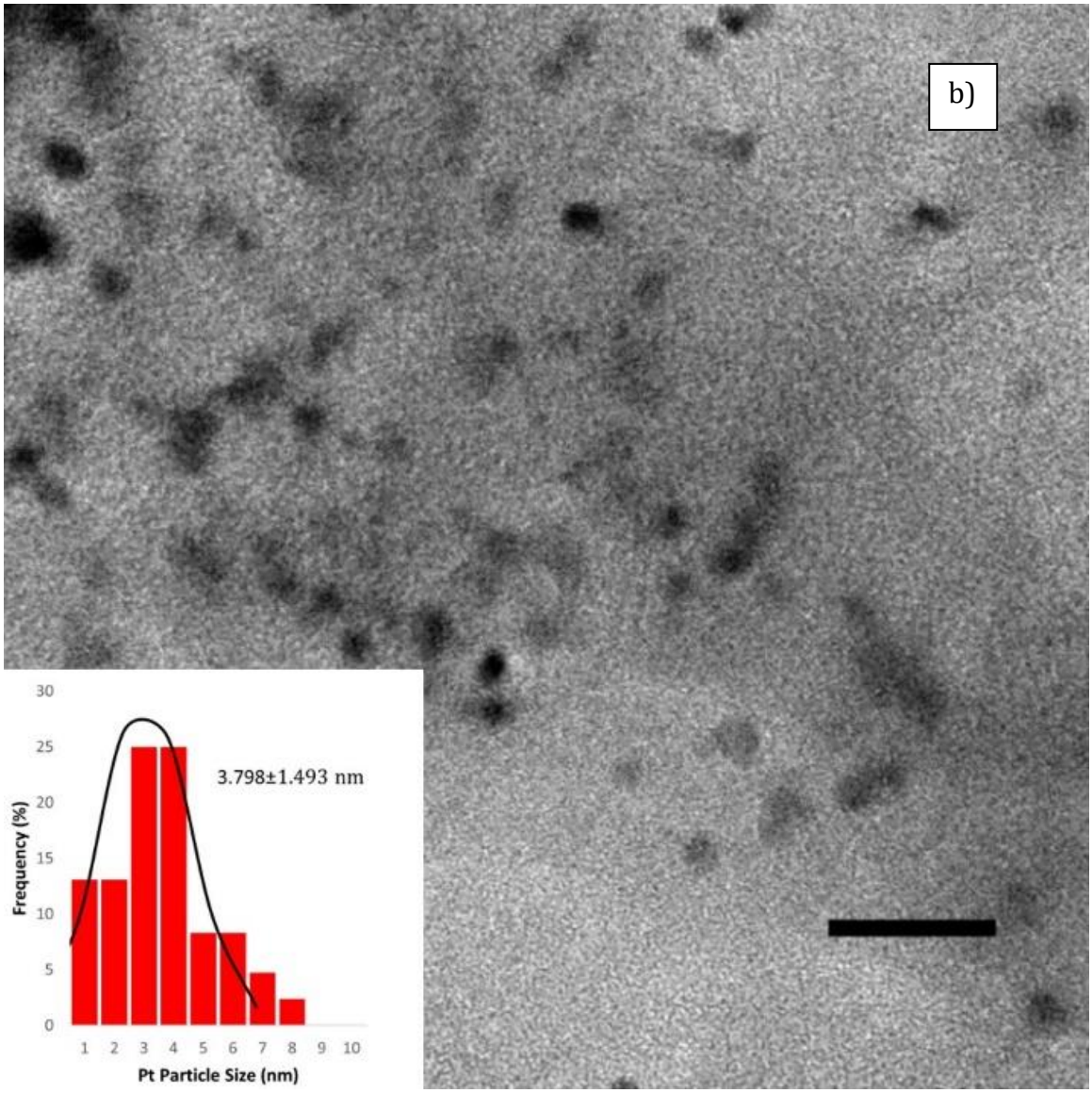
b)
3.798±1.493 nm
Frequency (%)
Pt Particle Size (nm)
0
5
10
15
20
25
30
1
2
3
4
5
6
7
8
9
10

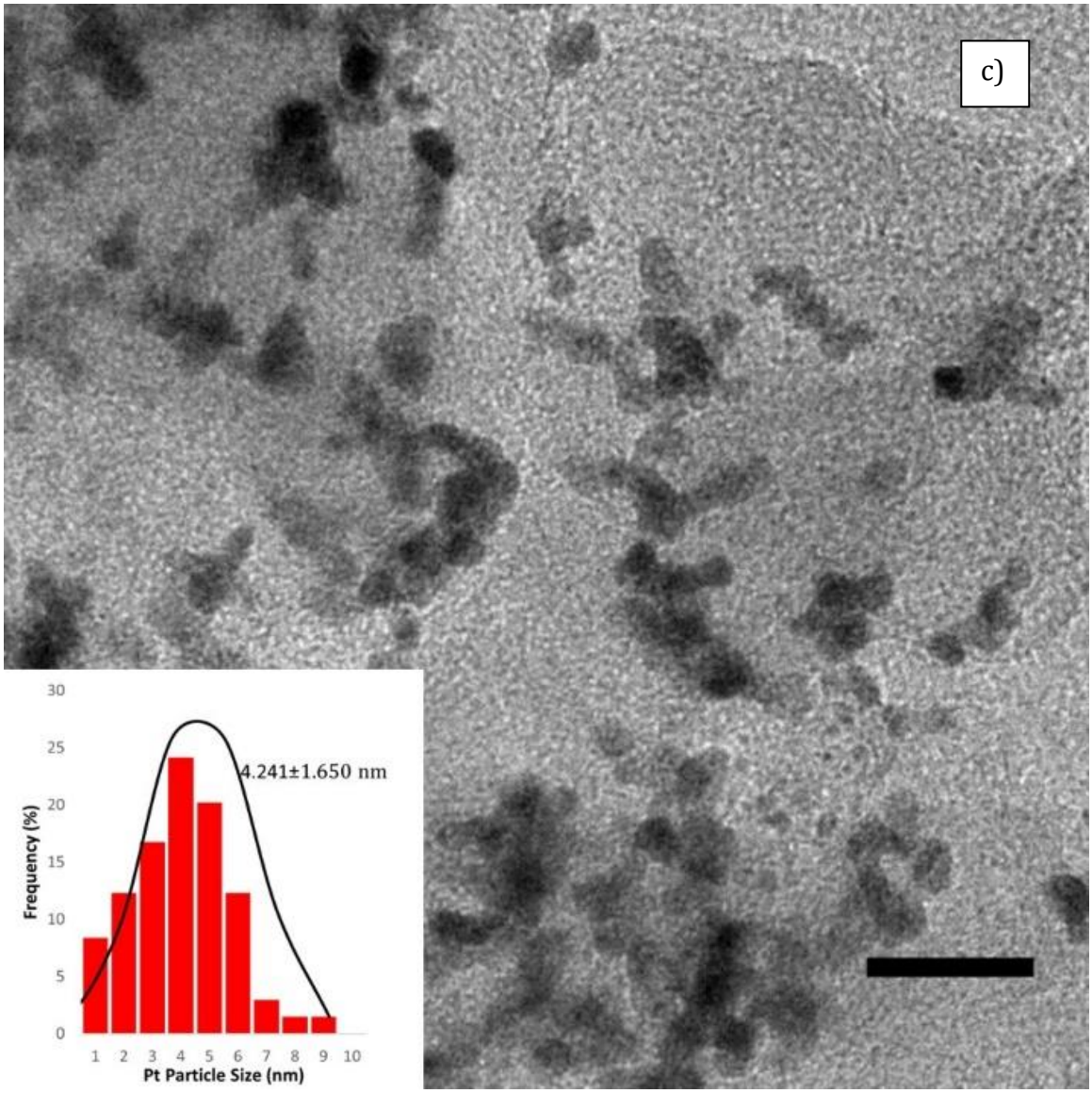
c)
4.241±1.650 nm
Frequency (%)
Pt Particle Size (nm)
0
5
10
15
20
25
30
1 2 3 4 5 6 7 8 9 10

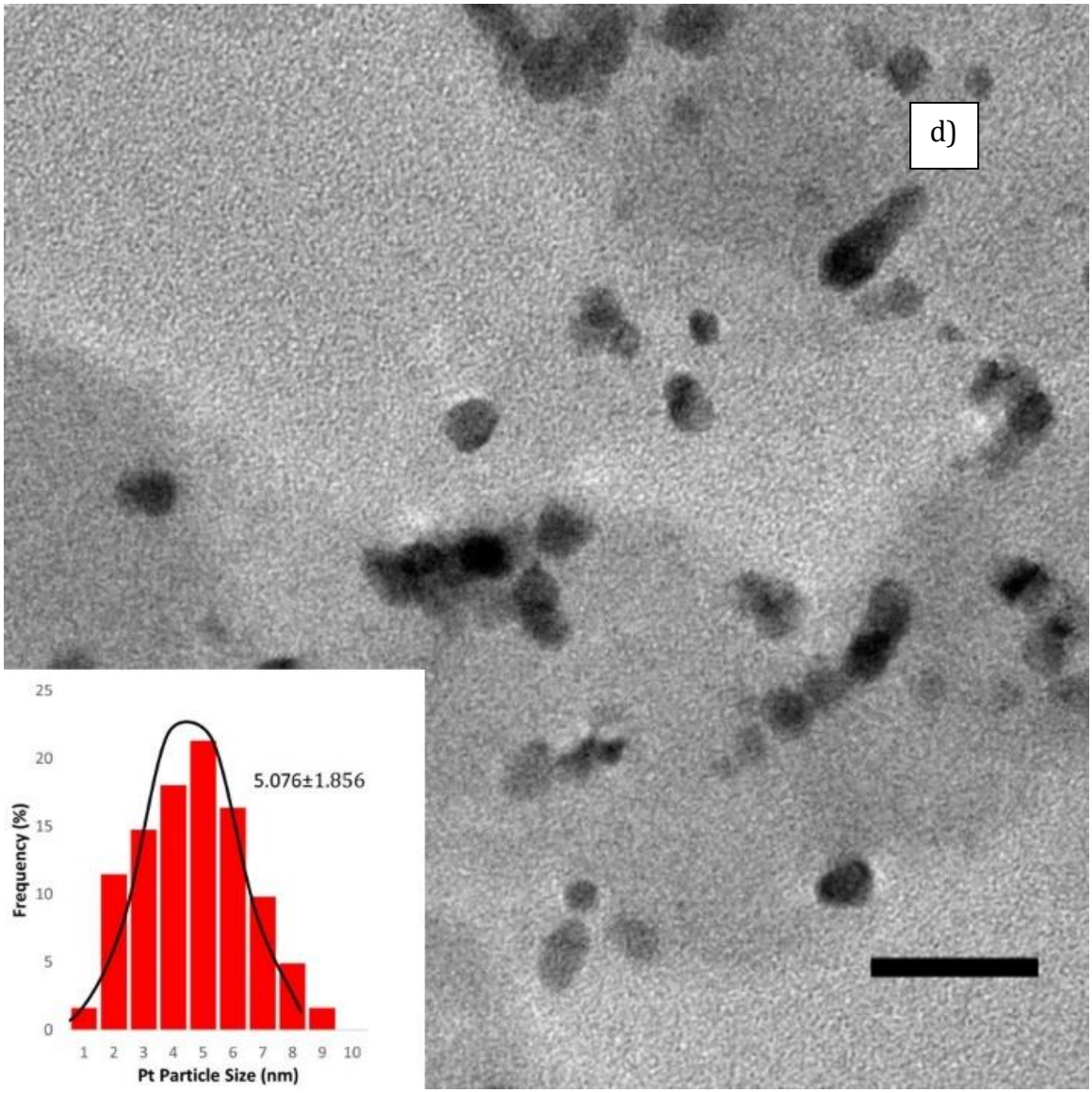

Fig. S6. TEM images of the catalysts: a) Pt-3F; b) Pt-4F; c) Pt-3C; and d) Pt-4C with particle size distribution charts. The measuring bar indicates 20 nm.

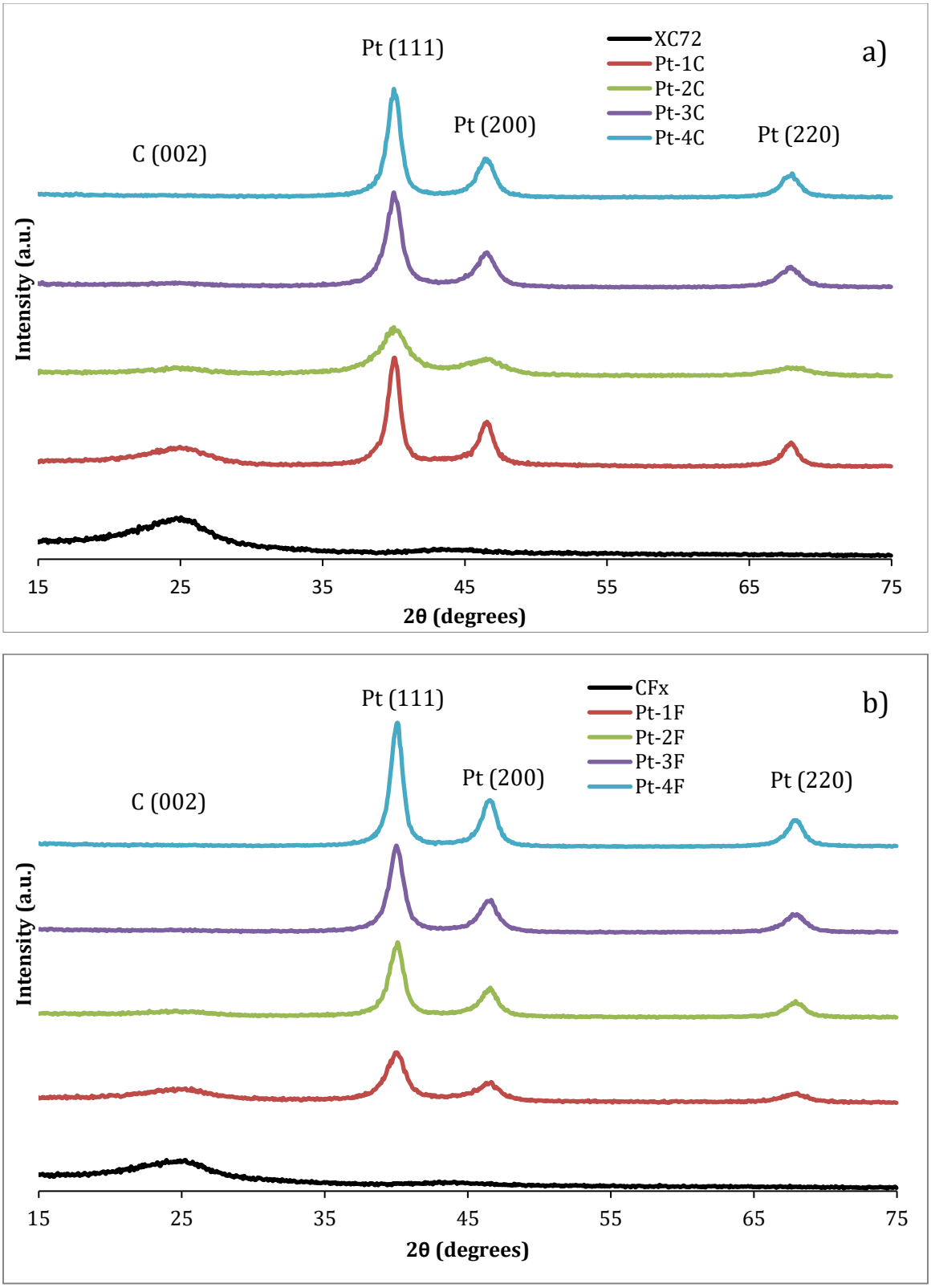

Fig. S7. XRD patterns of the catalysts on: a) XC-72R; and b) CFx support.

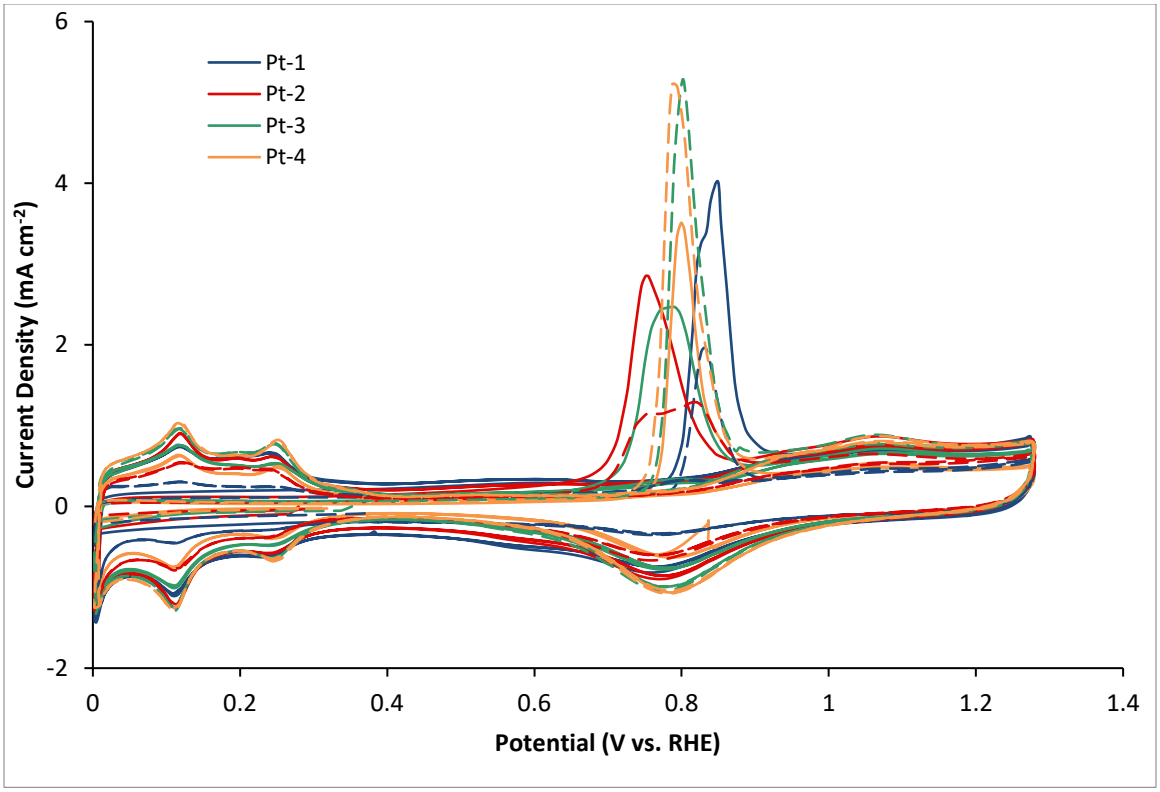

Fig. S8. CO stripping CVs for the catalysts. The solid lines indicate the CFx samples; the dashed lines indicate the XC-72R samples.

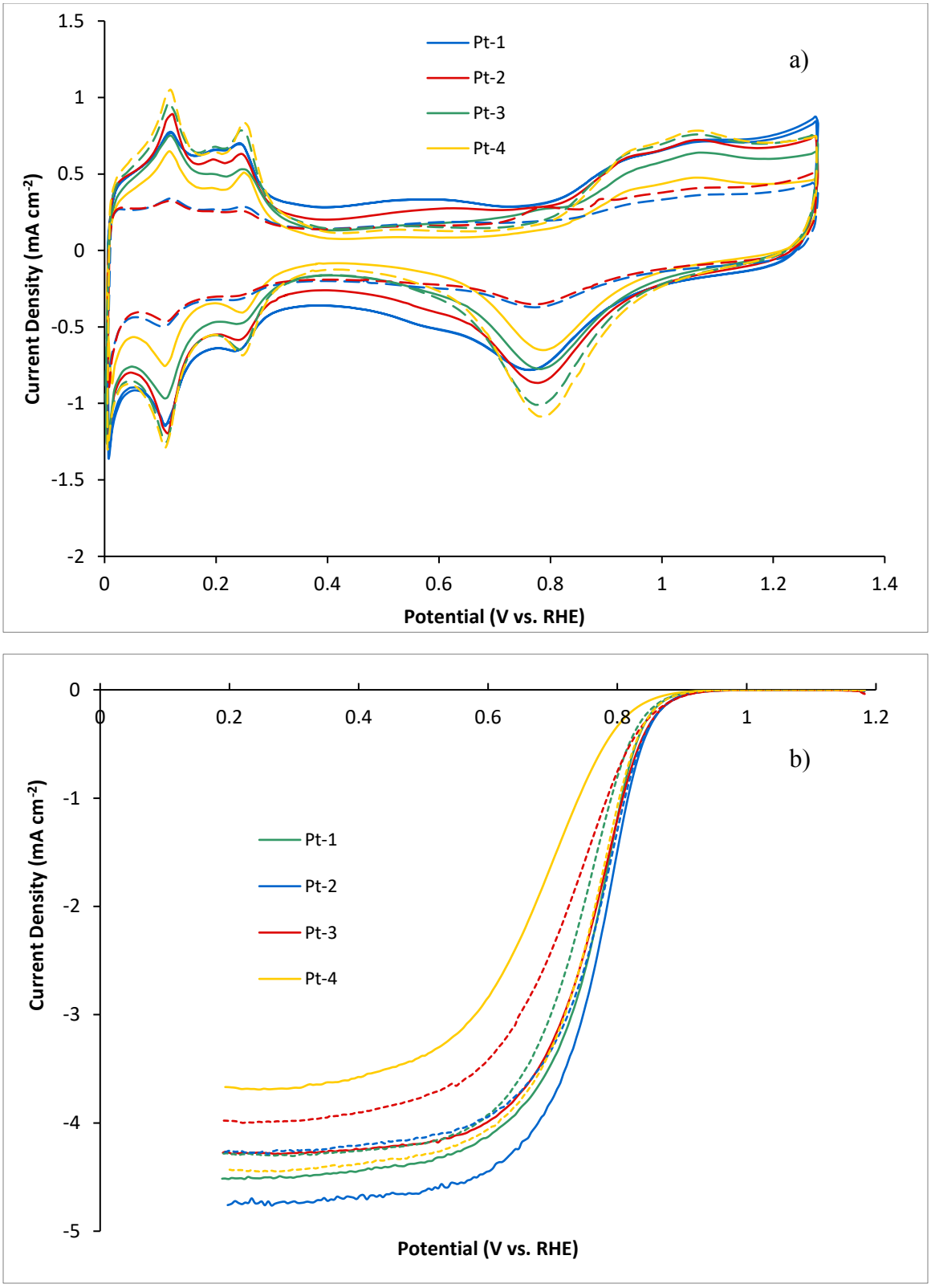

Fig S9. a) CV scans of the catalysts in 0.5 M H_2SO_4 solution at 20 mV s^{-1} under Ar. The solid lines indicate the CFx support; the dashed lines indicate the XC-72R support. b) LSV scan at 1600 RPM for all the catalysts. The solid lines indicate the CFx support; the dashed lines indicate the XC-72R support.

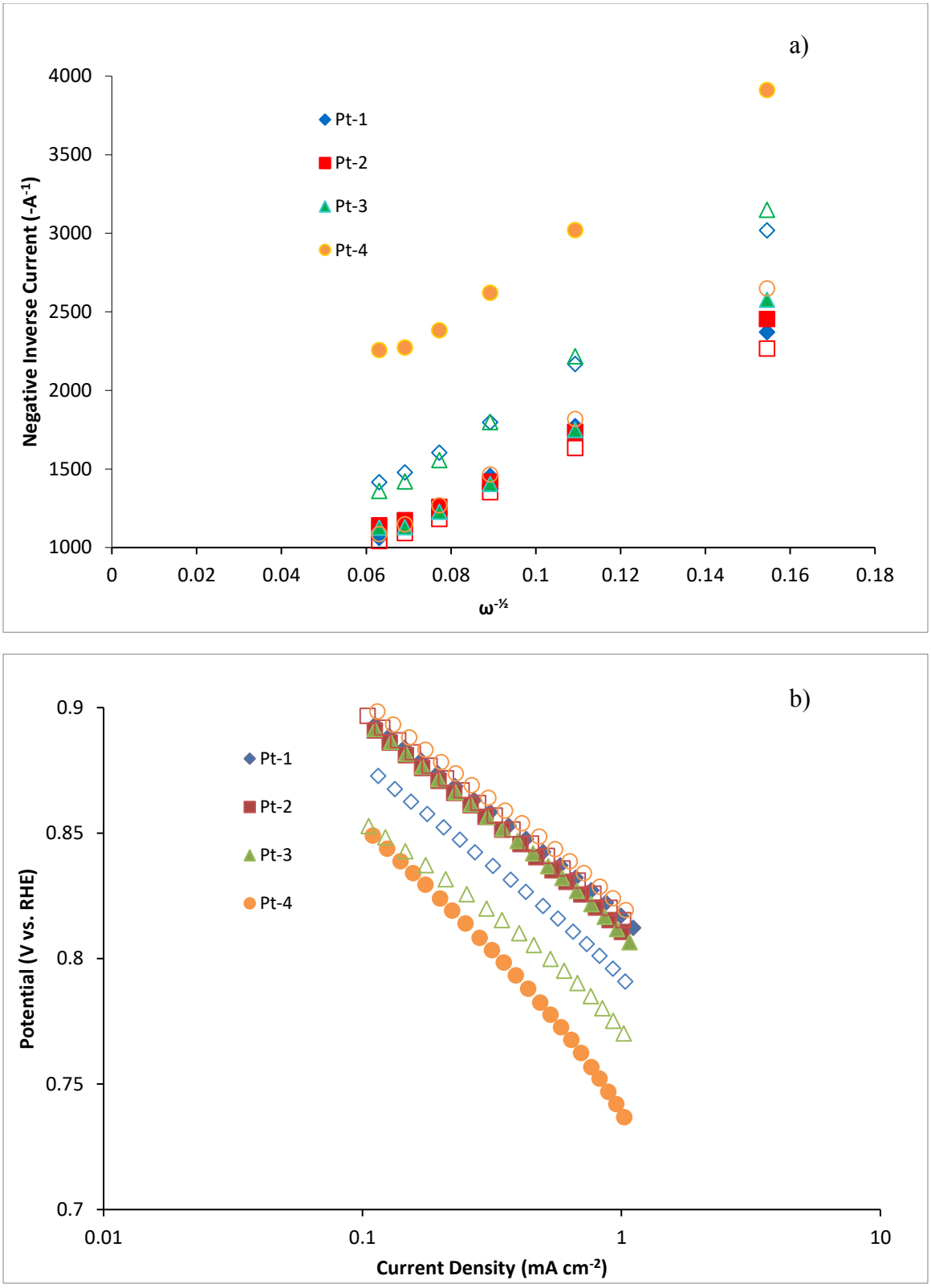

Fig S10. a) Koutecky-Levich plot of the catalysts at 0.6 V vs. RHE. The solid markers indicate the CFx support; the hollow markers indicate the XC-72R support. b) The Tafel plot for the catalysts. The solid markers indicate the CFx support; the hollow markers indicate the XC-72R support.

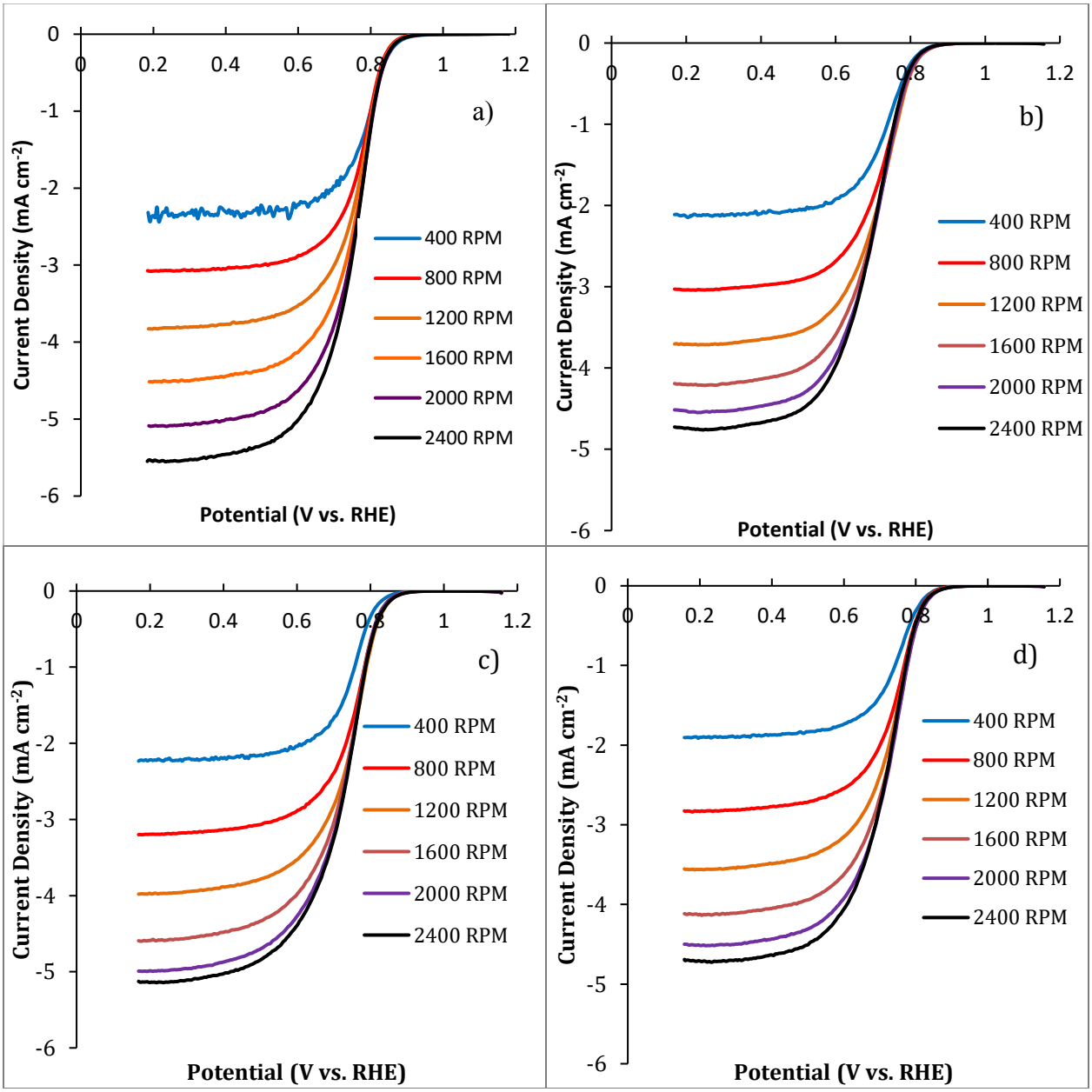
a)
b)
c)
d)
Current Density (mA cm-2)
Potential (V vs. RHE)
400 RPM
800 RPM
1200 RPM
1600 RPM
2000 RPM
2400 RPM

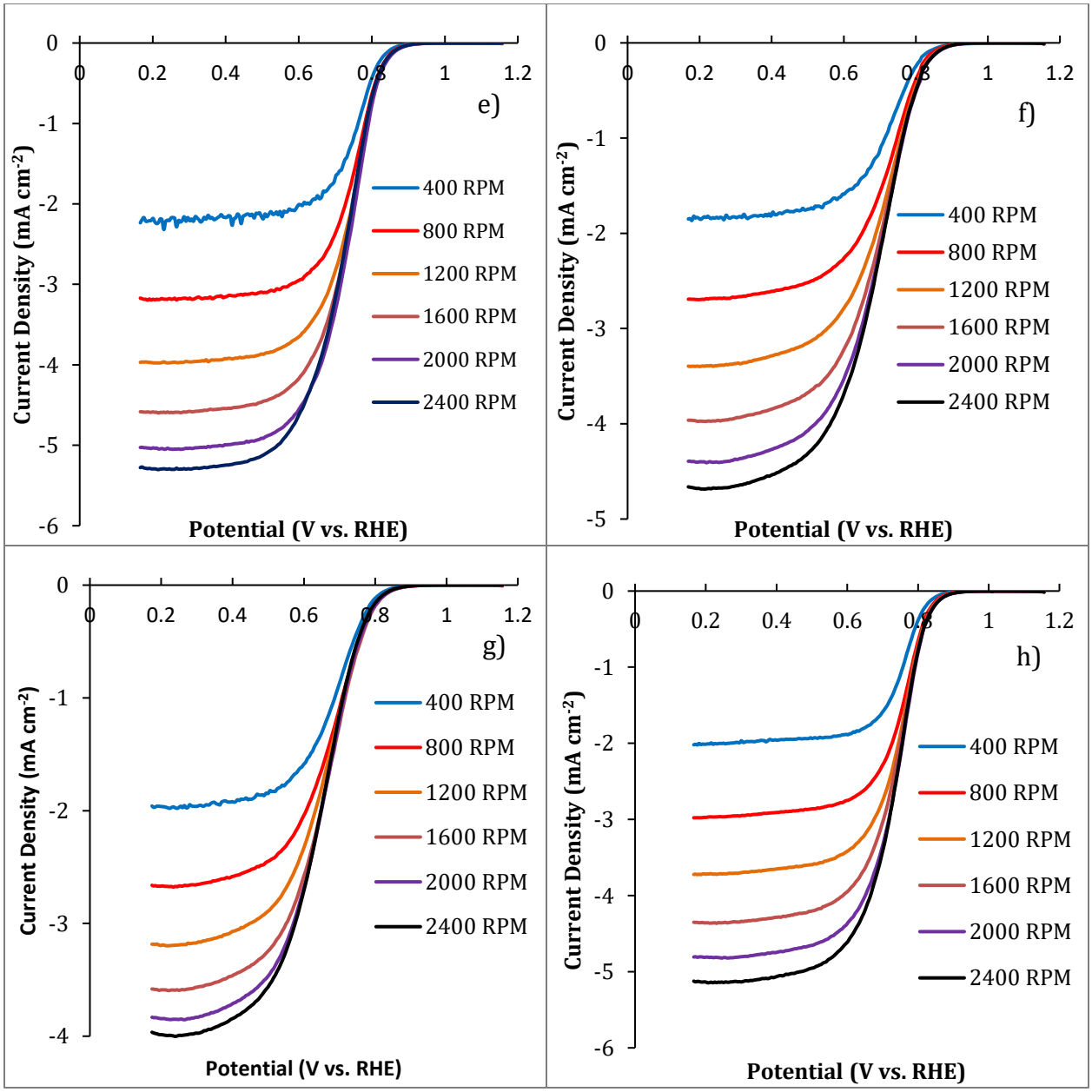

Fig. S11. LSV scans of the catalysts in 0.5 M H_2SO_4 solution at 5 mV s^{-1}: a) of the Pt-1F; b) Pt-1C; c) Pt-2F; d) Pt-2C; e) Pt-3F; f) Pt-3C; g) Pt-4F; h) Pt-4C.

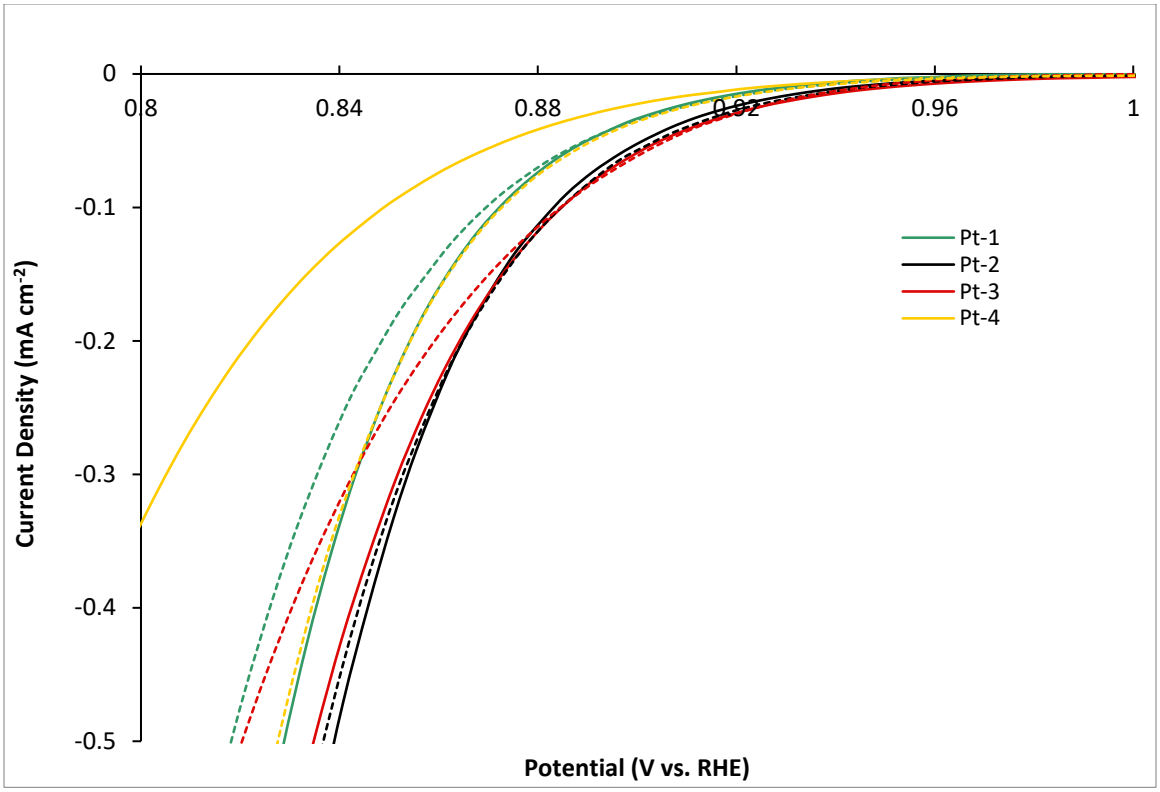

Fig. S12. Zoom-In for the onset potential of the LSV plots at 1600 RPM in 0.5 M H_2SO_4 solution scanned at 5 mV s^{-1}. The solid lines indicate the CFx support; the dashed lines indicate the XC-72R support.

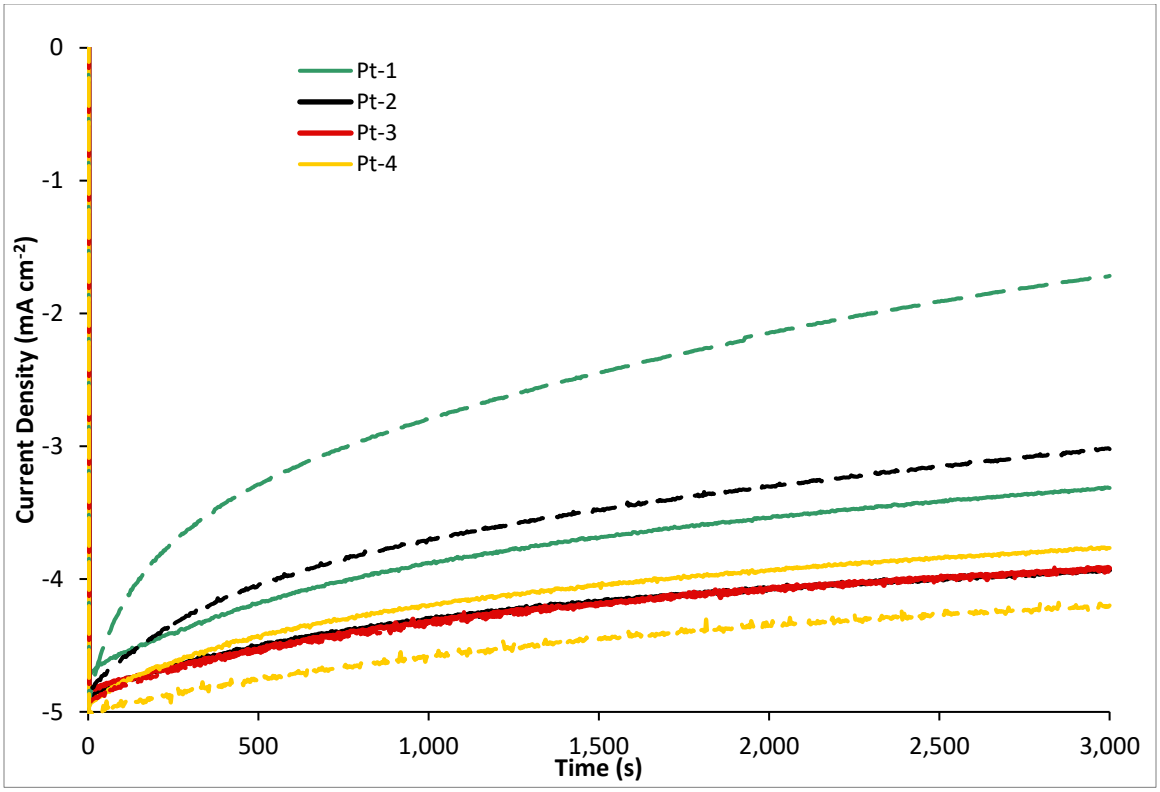

Fig. S13 Chronoamperommetry curves for the catalysts at 1600 RPM at 0.18 V vs. RHE. The solid lines indicate the CFx support; the dashed lines indicate XC-72R support.

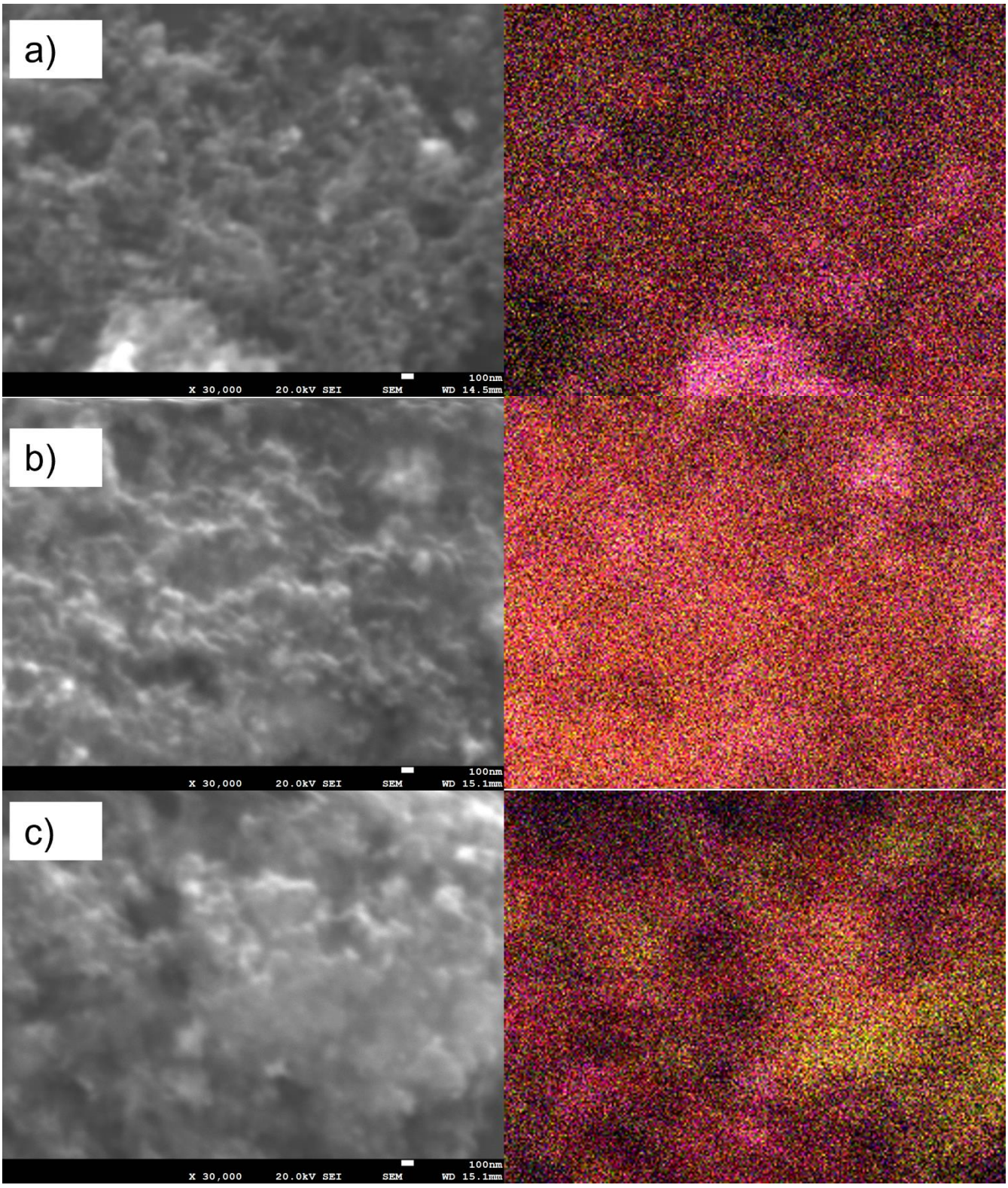
a)
X 30,000 20.0kV SEI SEM WD 14.5mm
100nm
b)
X 30,000 20.0kV SEI SEM WD 15.1mm
100nm
c)
X 30,000 20.0kV SEI SEM WD 15.1mm
100nm

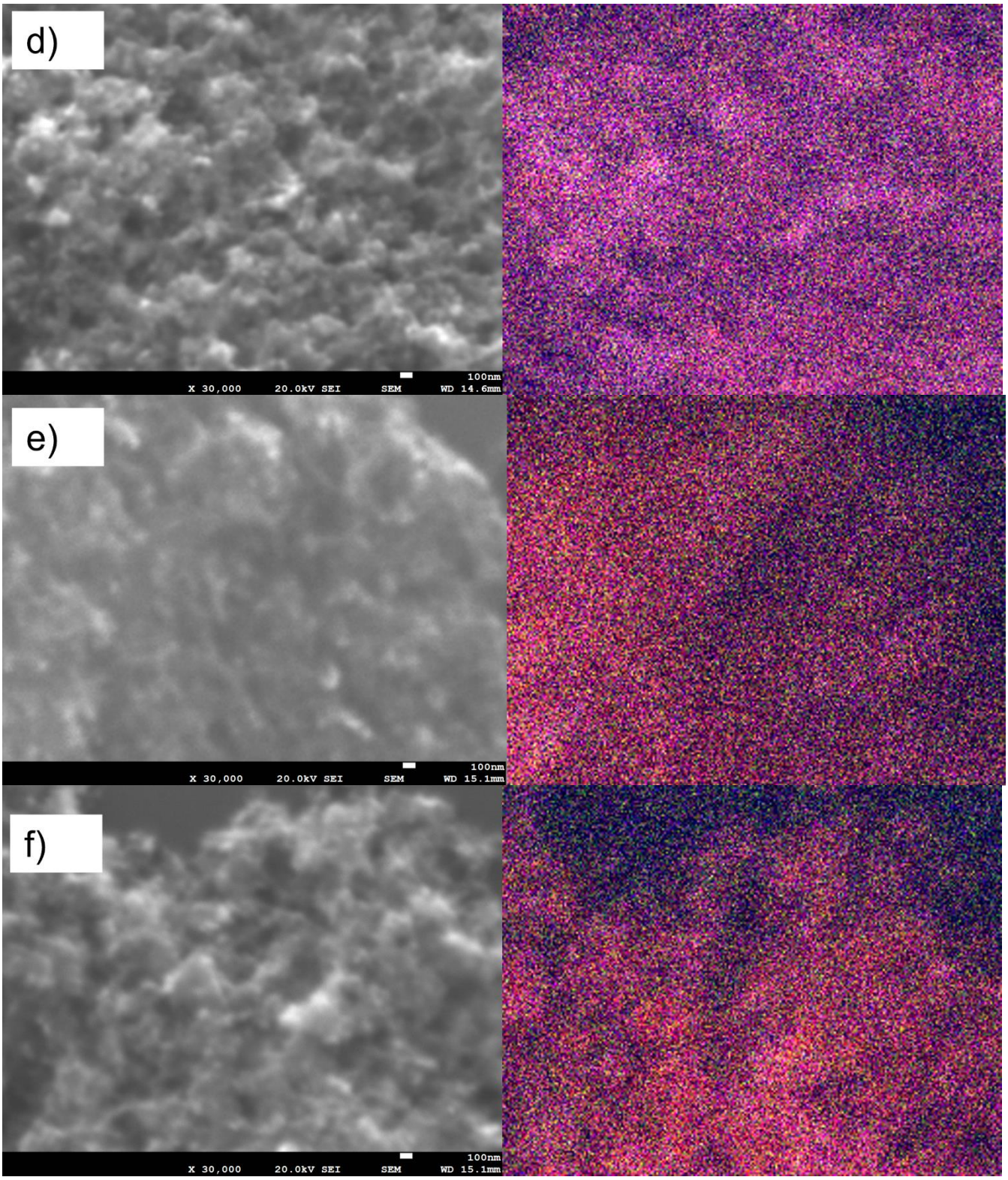

Fig. S14. SEM and EDS images for a) Pt-2C; b) Pt-2C after 3000 cycles; c) Pt-2C after start-stop; d) Pt-2F; e) Pt-2F after 3000 cycles and f) Pt-2F after start-stop in ORR potential region. For elemental mapping red corresponds to C, green corresponds to oxygen, blue corresponds to fluorine, magenta corresponds to Pt and yellow corresponds to sulfur.

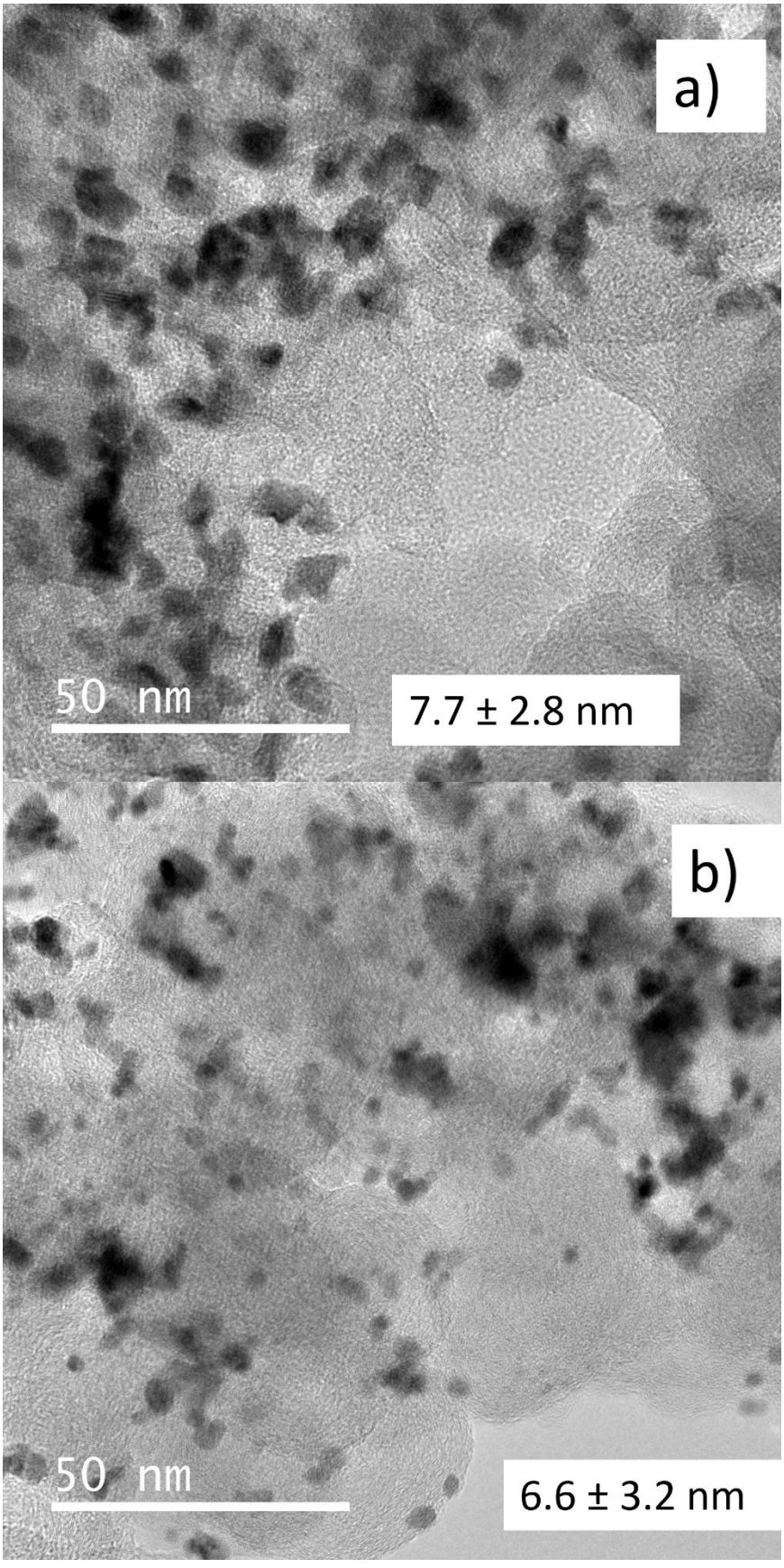
a)
50 nm
7.7 ± 2.8 nm
b)
50 nm
6.6 ± 3.2 nm

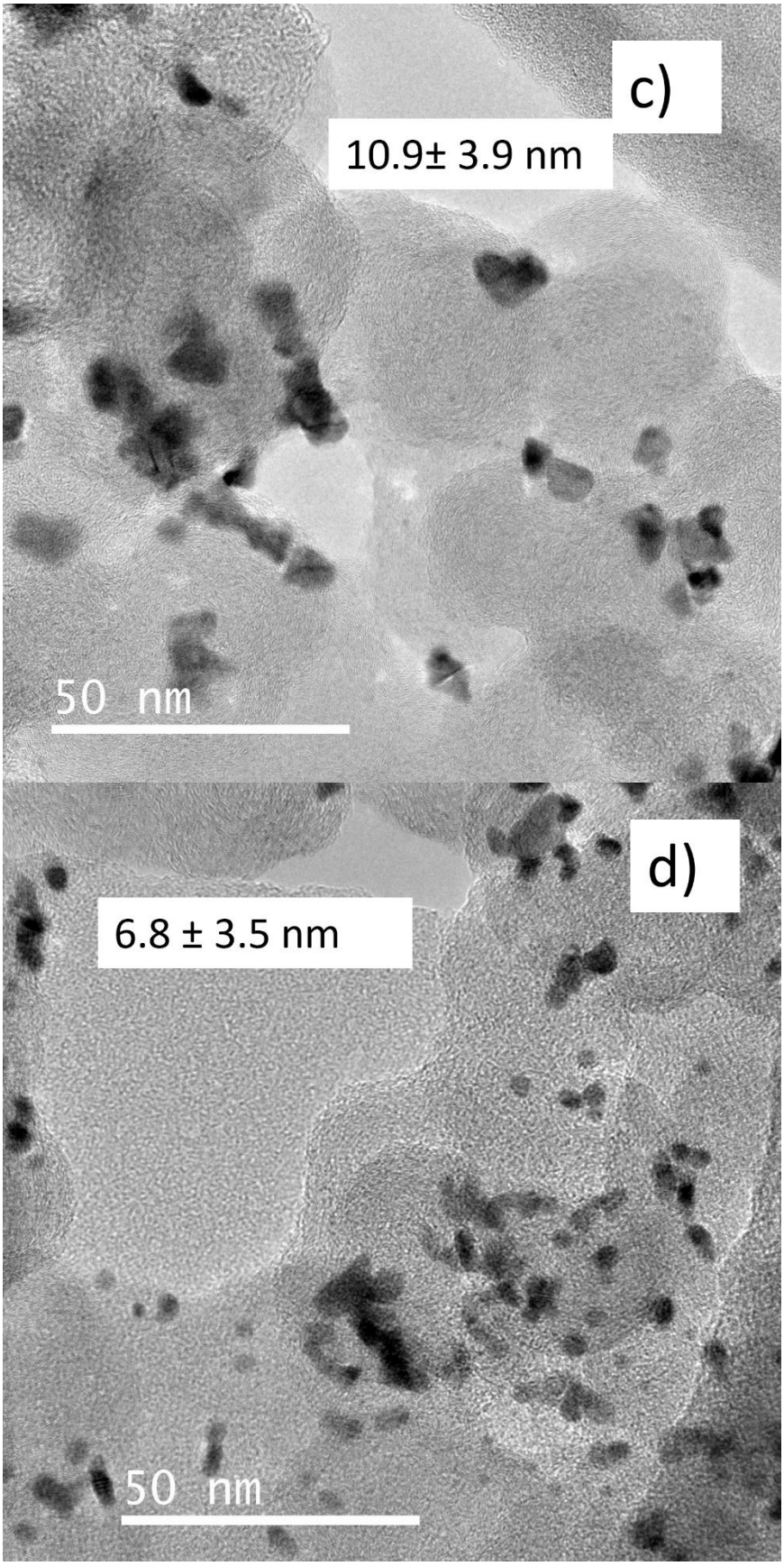

Fig. S15. TEM micrographs of a) Pt-2C and b) Pt-2F after start stop stability and c) Pt-2C and d) Pt-2F after 3000 cycles.

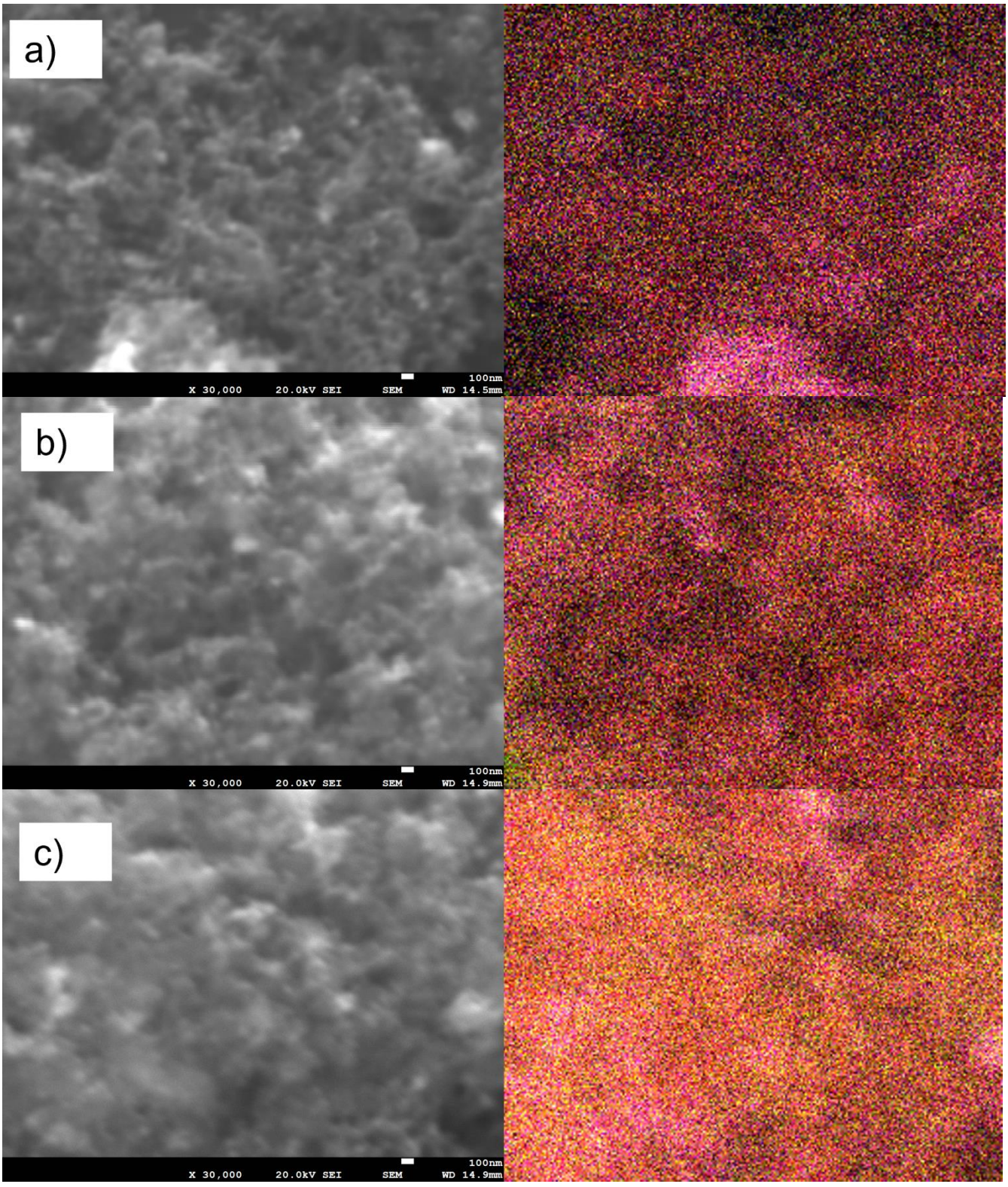
a)
X 30,000 20.0kV SEI SEM WD 14.5mm
100nm
b)
X 30,000 20.0kV SEI SEM WD 14.9mm
100nm
c)
X 30,000 20.0kV SEI SEM WD 14.9mm
100nm

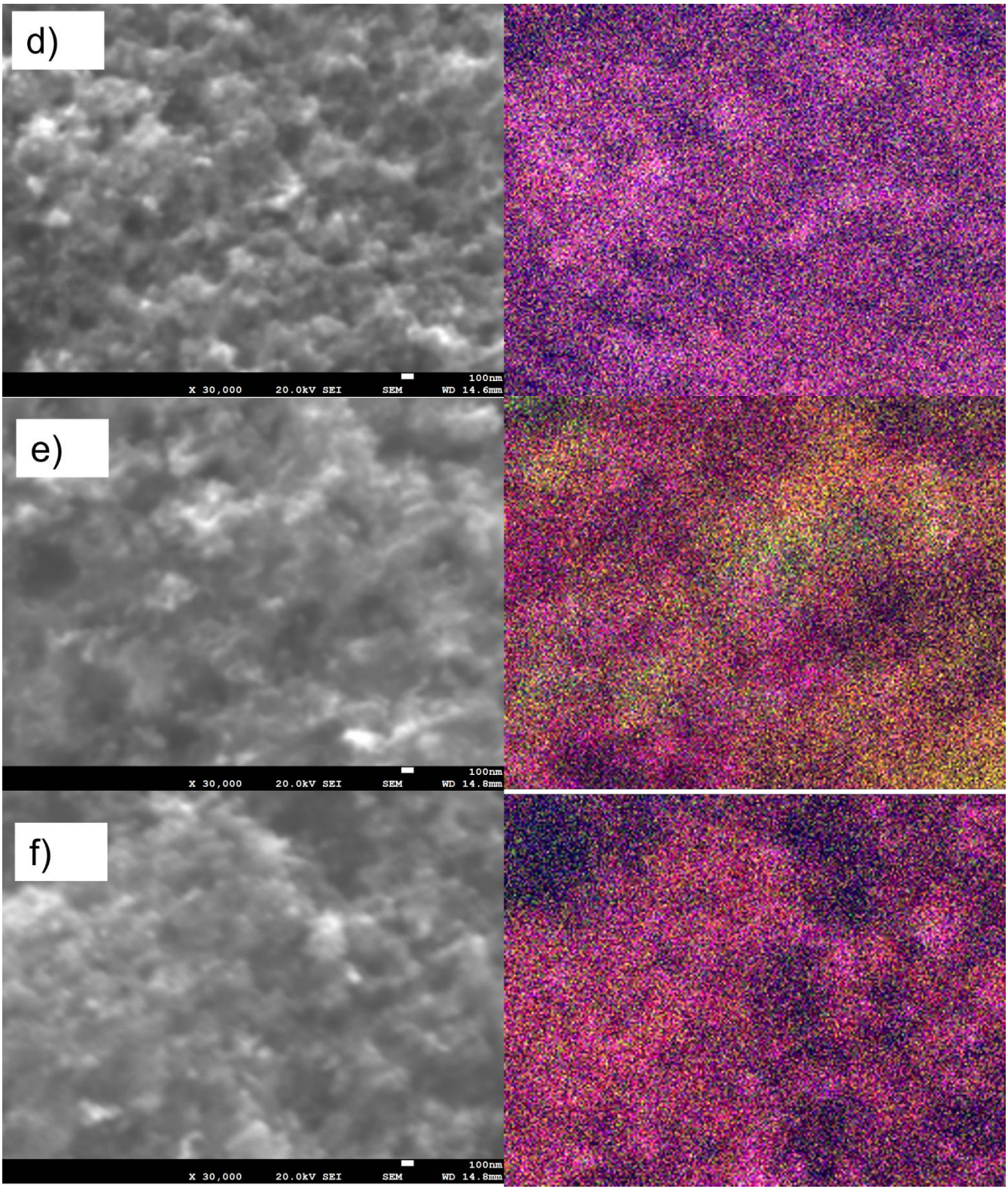

Fig. S16. SEM and EDS images for a) Pt-2C; b) Pt-2C after 3000 cycles; c) Pt-2C after start-stop; d) Pt-2F; e) Pt-2F after 3000 cycles and f) Pt-2F after start-stop in HOR potential region. For elemental mapping red corresponds to C, green corresponds to oxygen, blue corresponds to fluorine, magenta corresponds to Pt and yellow corresponds to sulfur.

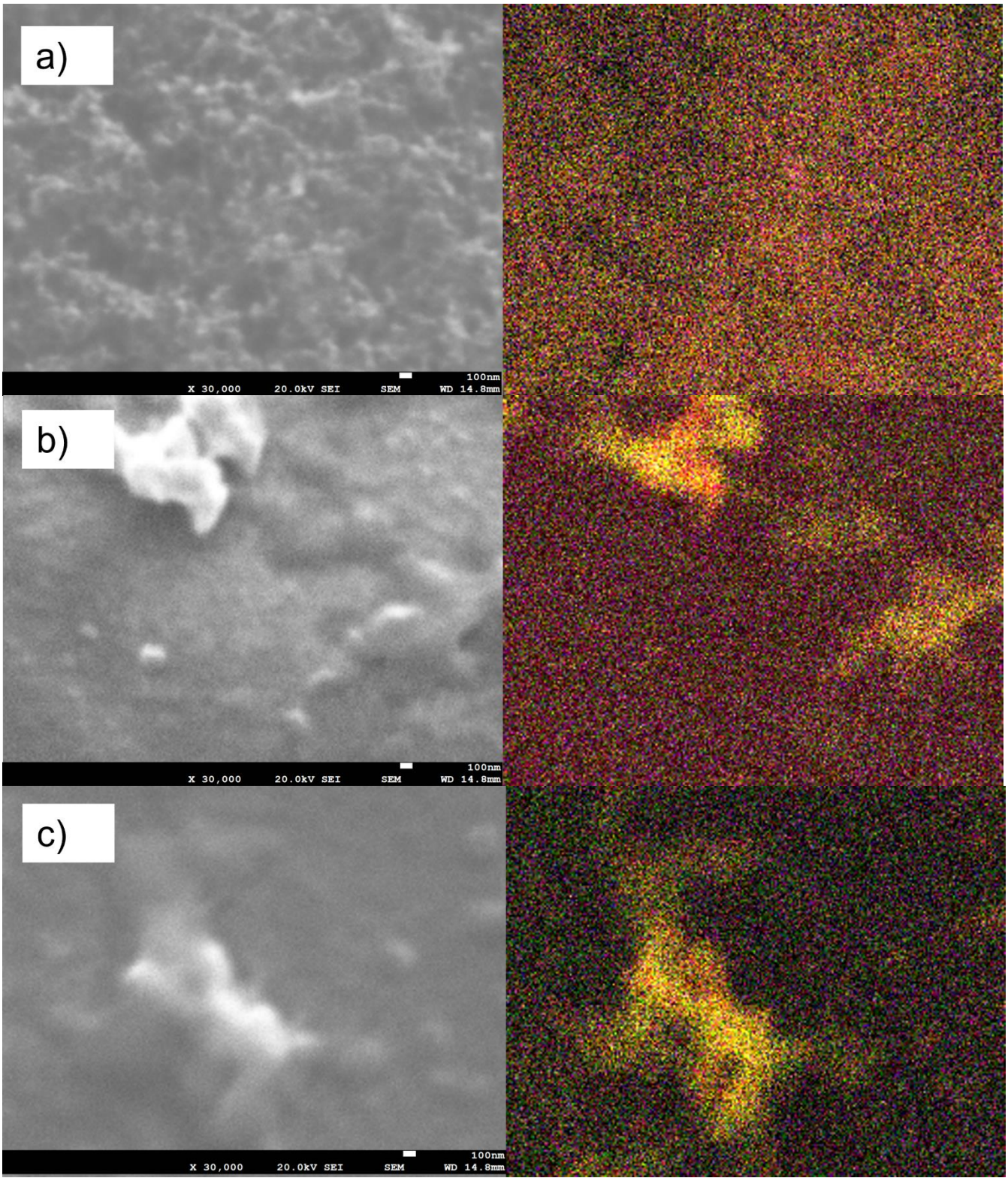
a)
X 30,000 20.0kV SEI SEM WD 14.8mm 100nm
b)
X 30,000 20.0kV SEI SEM WD 14.8mm 100nm
c)
X 30,000 20.0kV SEI SEM WD 14.8mm 100nm

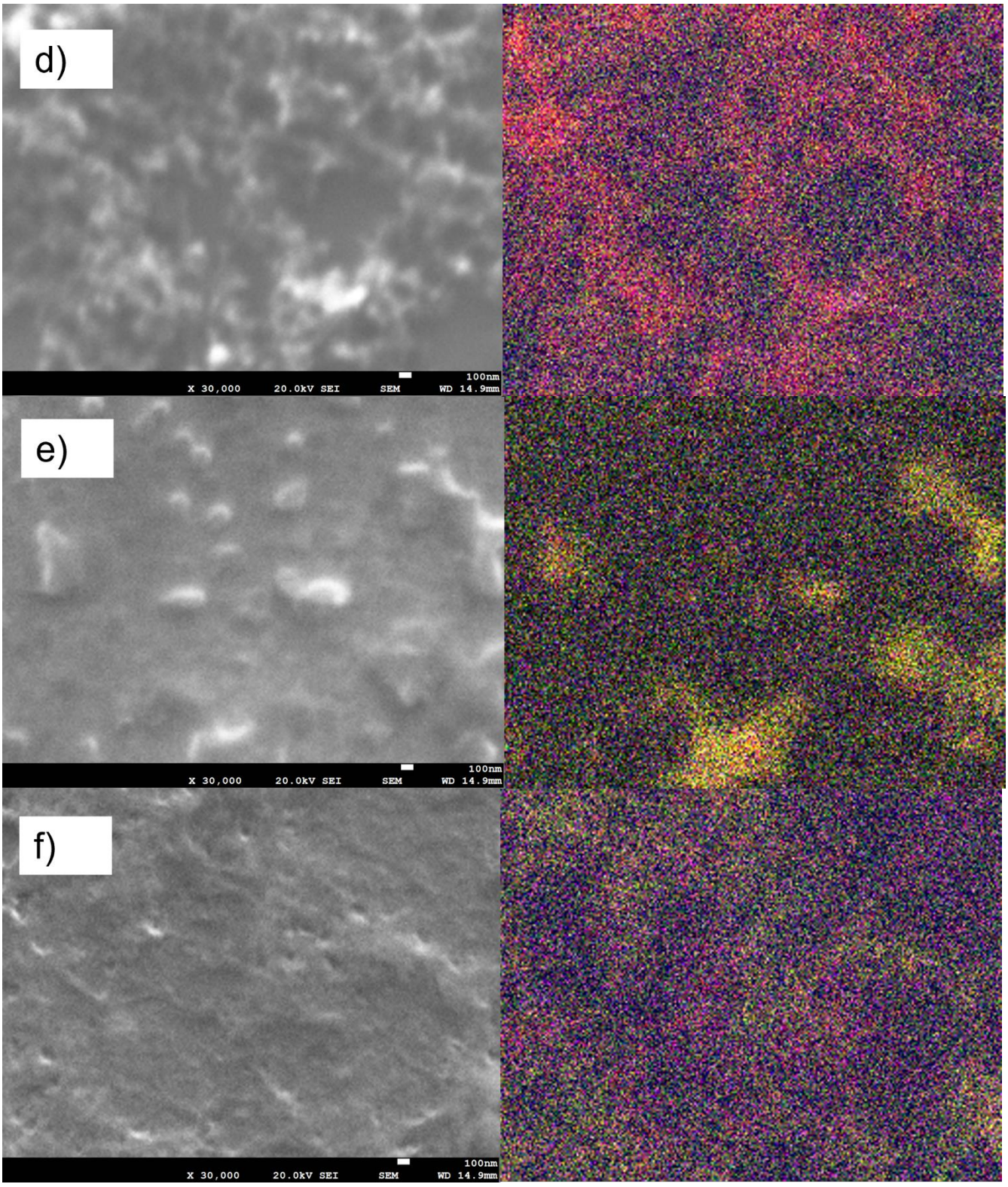

Fig. S17. SEM and EDS images for a) Pt-1C; b) Pt-1C after 3000 cycles; c) Pt-1C after start-stop; d) Pt-1F; e) Pt-1F after 3000 cycles and f) Pt-1F after start-stop in HOR potential region. For elemental mapping red corresponds to C, green corresponds to oxygen, blue corresponds to fluorine, magenta corresponds to Pt and yellow corresponds to sulfur.

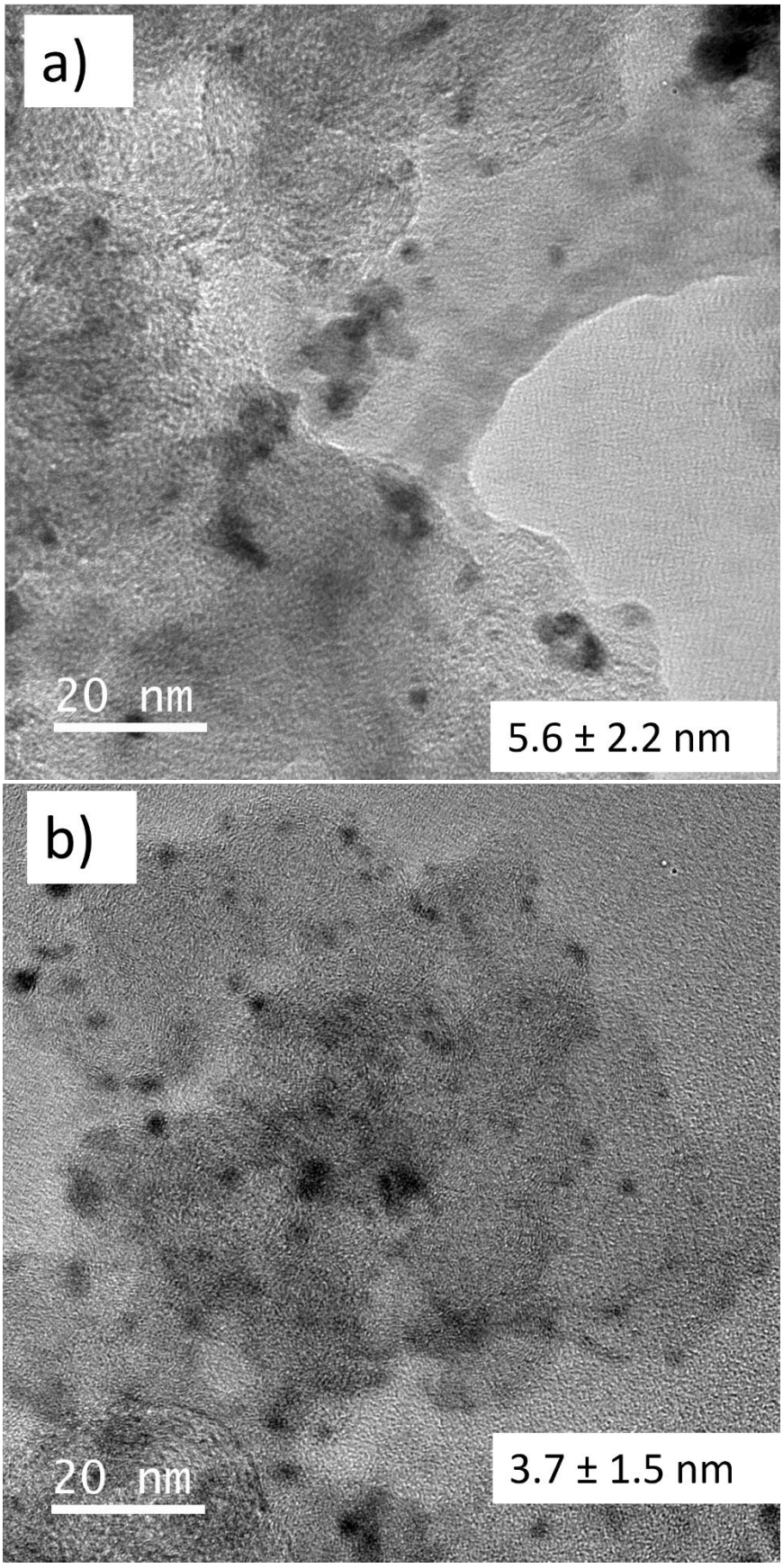
a)
20 nm
5.6 ± 2.2 nm
b)
20 nm
3.7 ± 1.5 nm

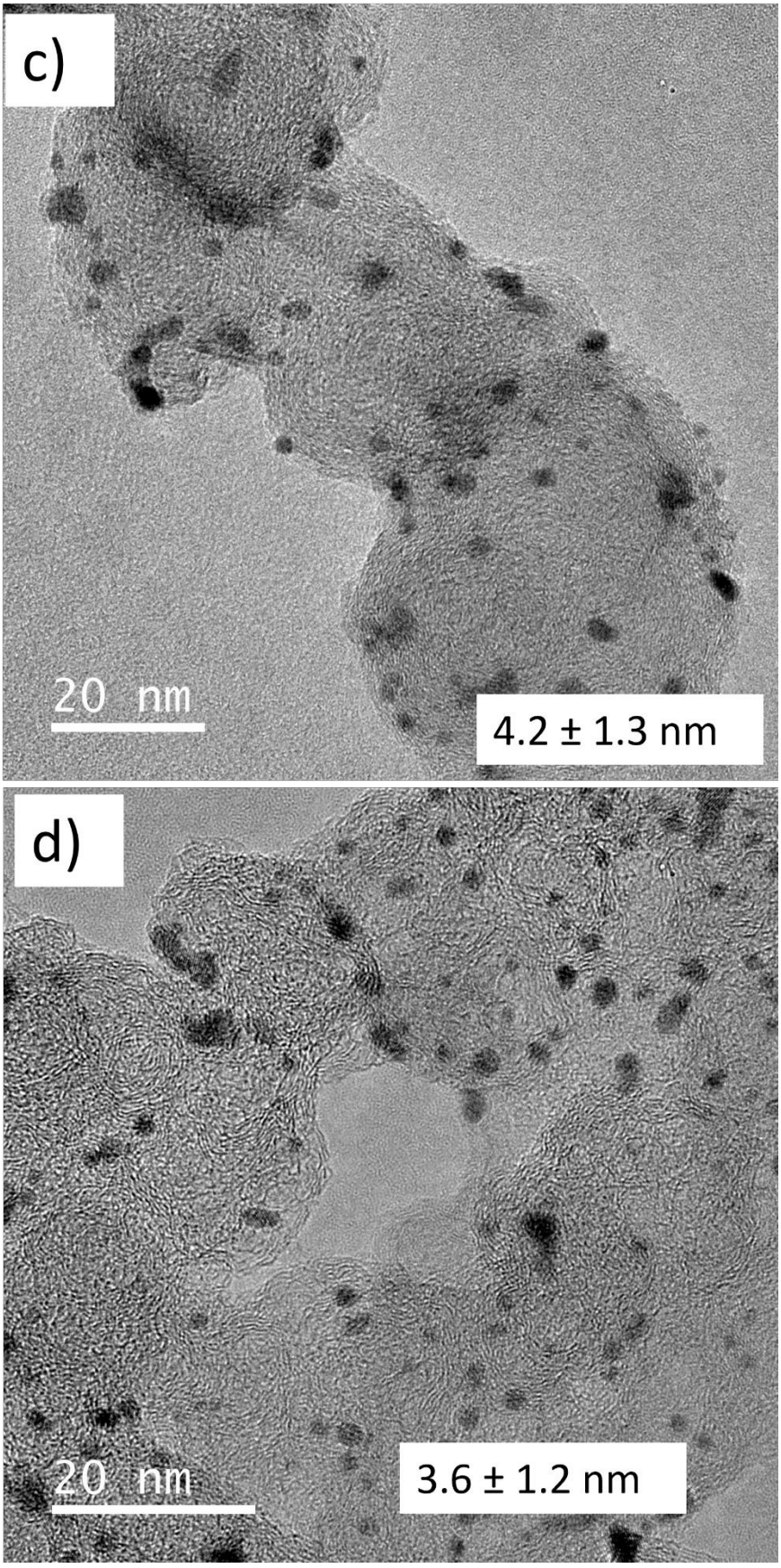
c)
20 nm
4.2 ± 1.3 nm
d)
20 nm
3.6 ± 1.2 nm

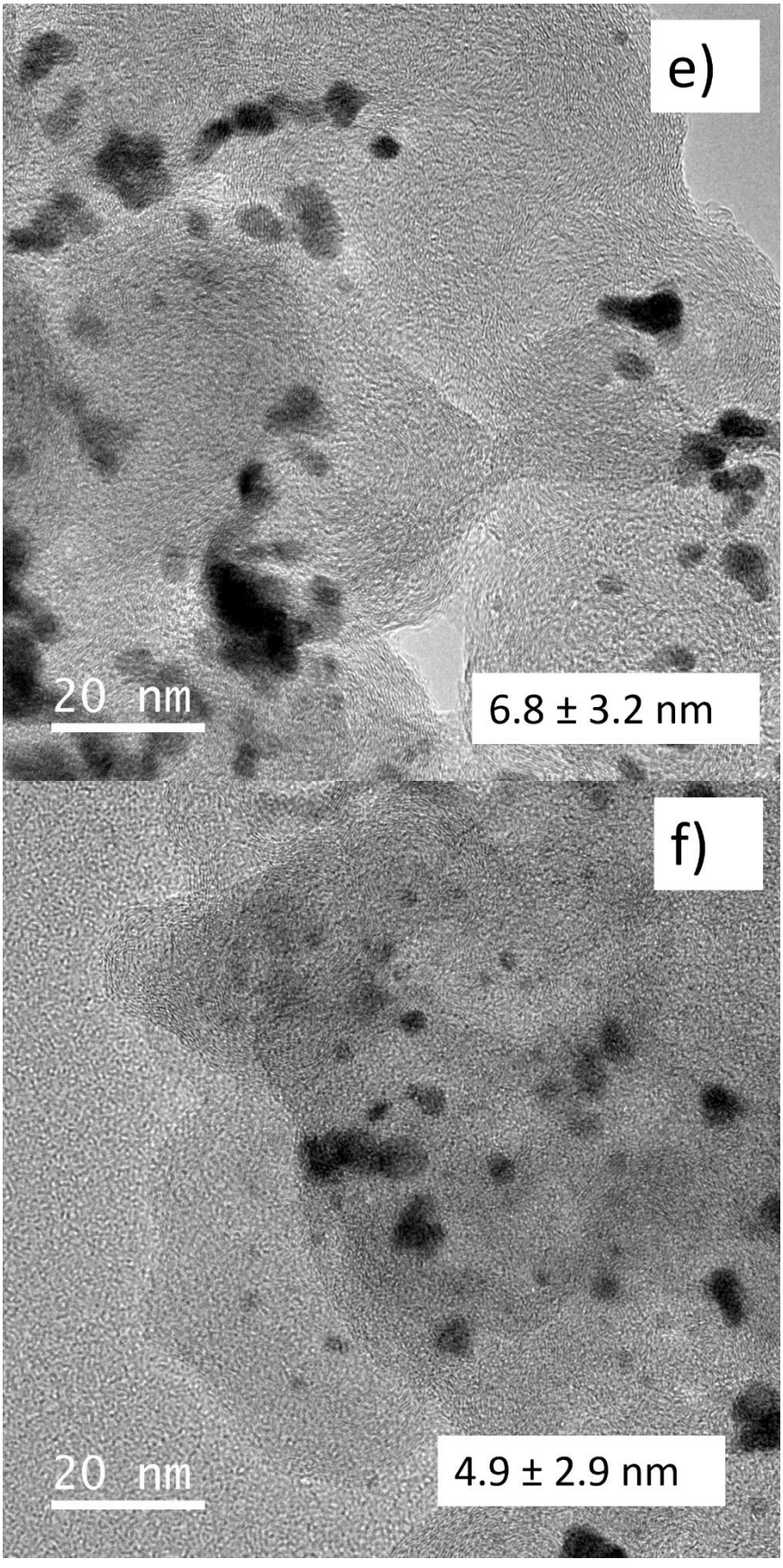
e)
20 nm
6.8 ± 3.2 nm
f)
20 nm
4.9 ± 2.9 nm

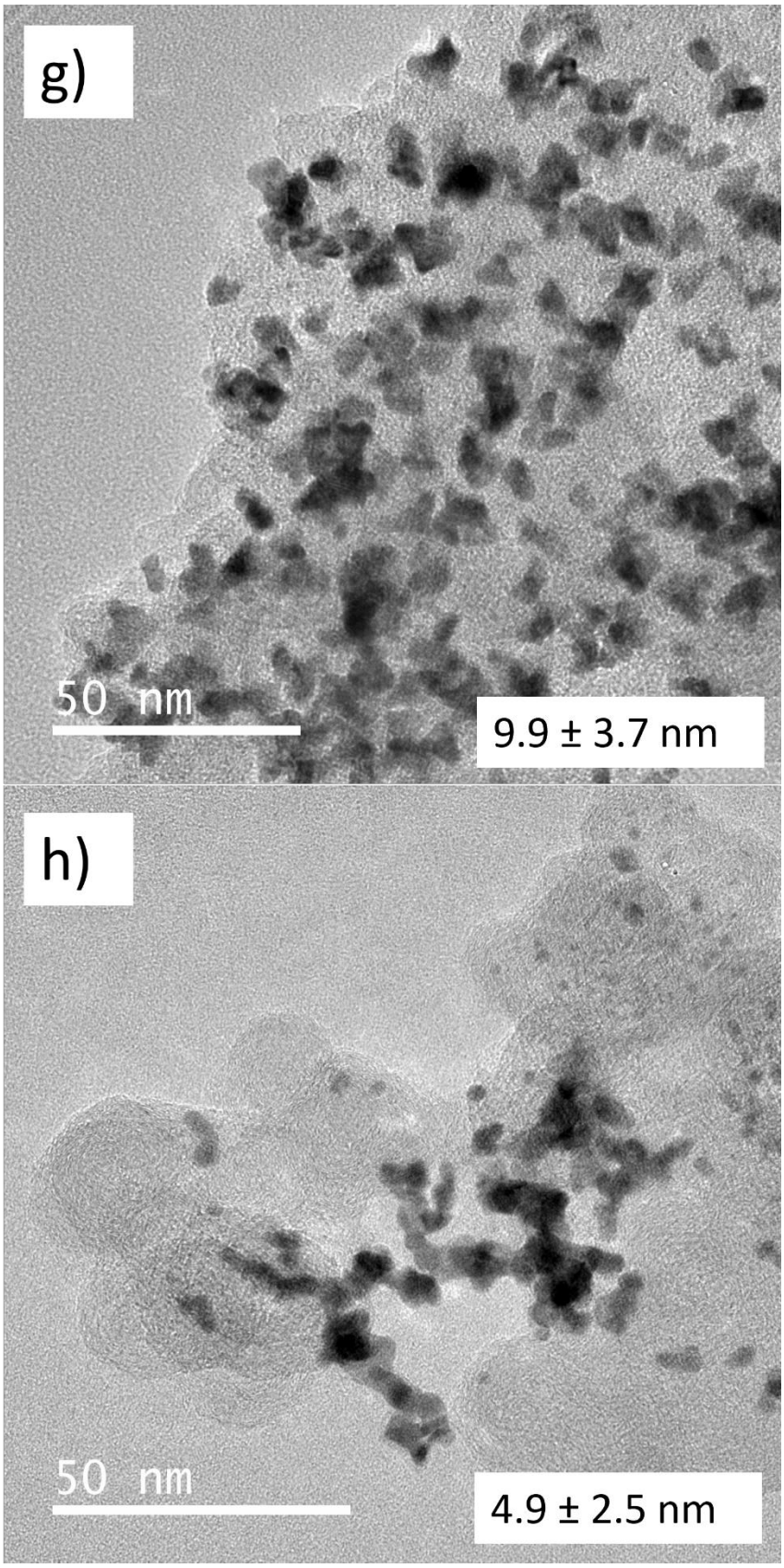

Fig. S18. TEM micrographs of a) Pt-1C and b) Pt-1F after 3000 cycles and c) Pt-1C and d) Pt-1F after start stop experiments. TEM micrographs of e) Pt-2C and f) Pt-2F after 3000 cycles and g) Pt-2C and h) Pt-2F after start stop experiments.

a)

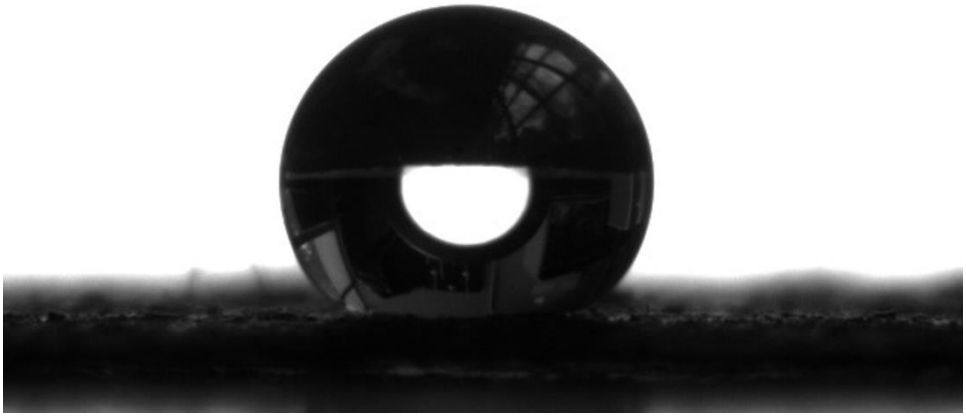

b)

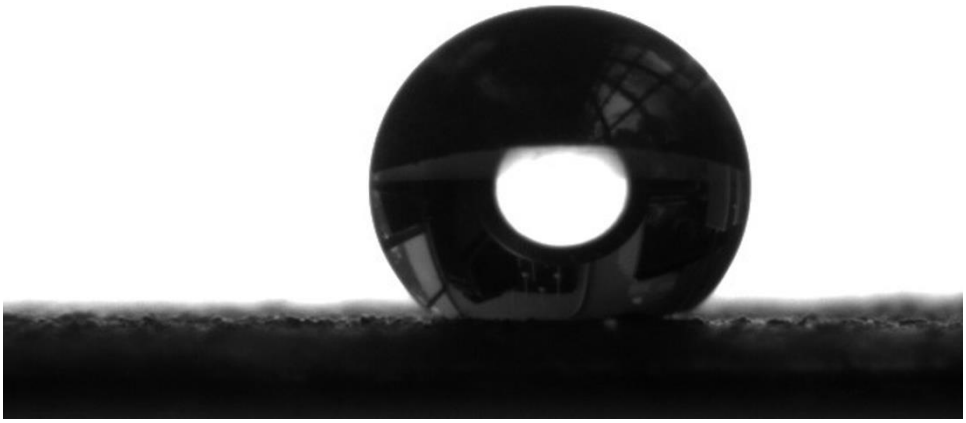

Fig. S19. Contact angle measurement image for a) Pt-1C and b) Pt-1F

a)

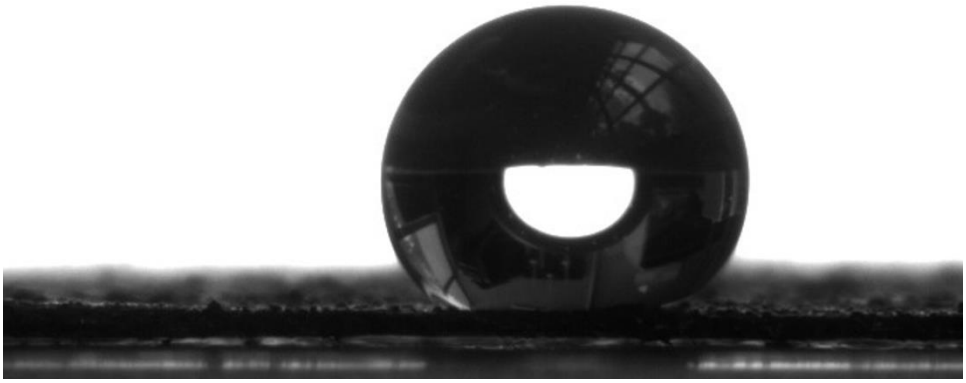

b)

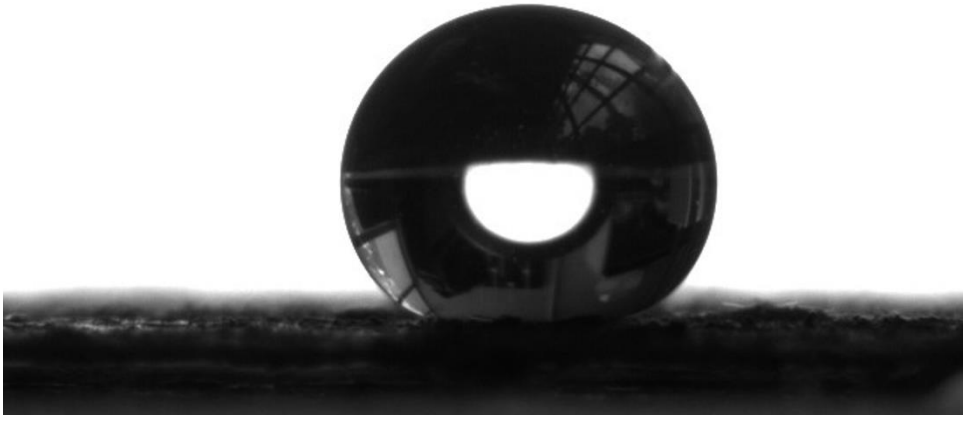

Fig. S20. Contact angle measurement image for a) Pt-2C and b) Pt-2F

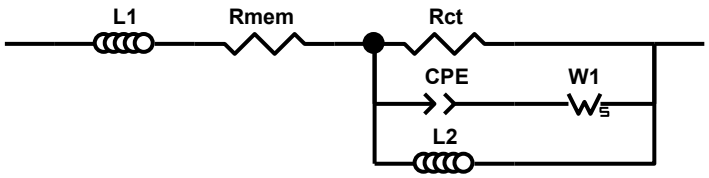

Fig. S21. Equivalent circuit of the EIS spectra for the fuel cells.

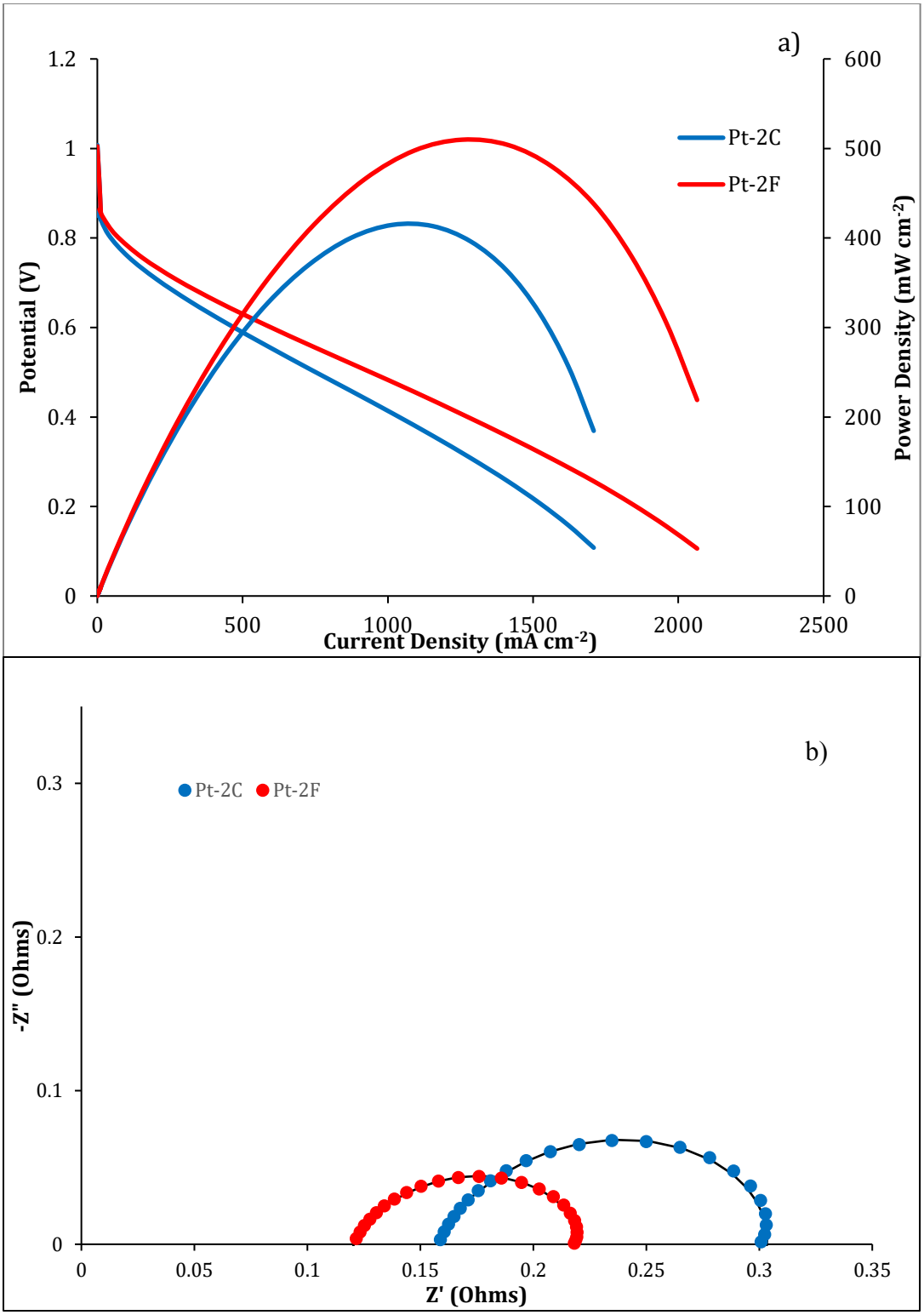

Fig. S22. Polarization curves for MEAs with the cathode electrode using the Pt-2 catalyst at: a) 25 °C. b) EIS curves for the Pt-2 catalyst MEAs at 0.4 V vs. reference at 25 °C.

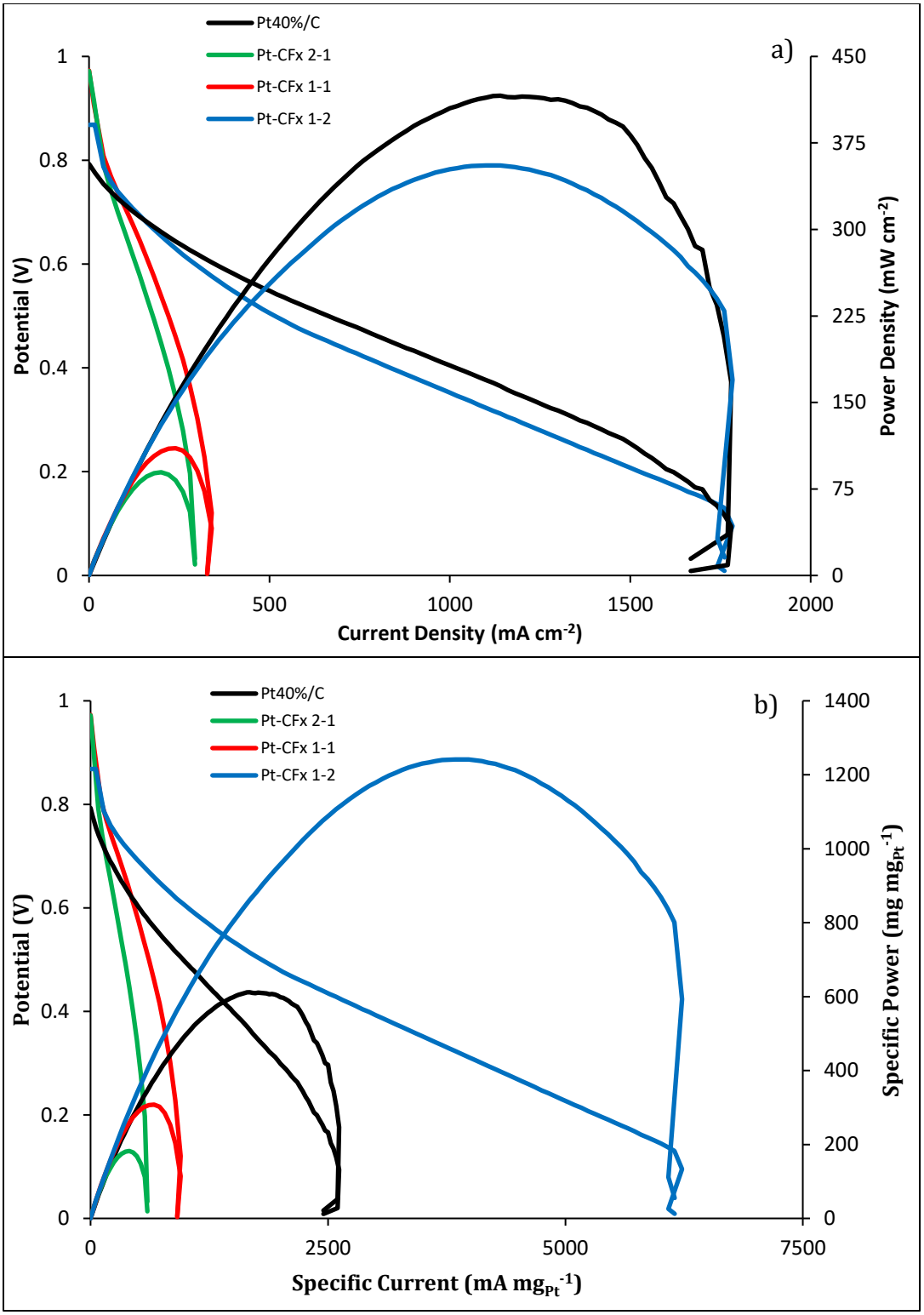

Figure S23. Polarization curves for the CFx mixed with the commercial Pt/C catalyst: a) normalized with respect to electrode surface area and; b) normalized with respect to platinum loading on the cathode.

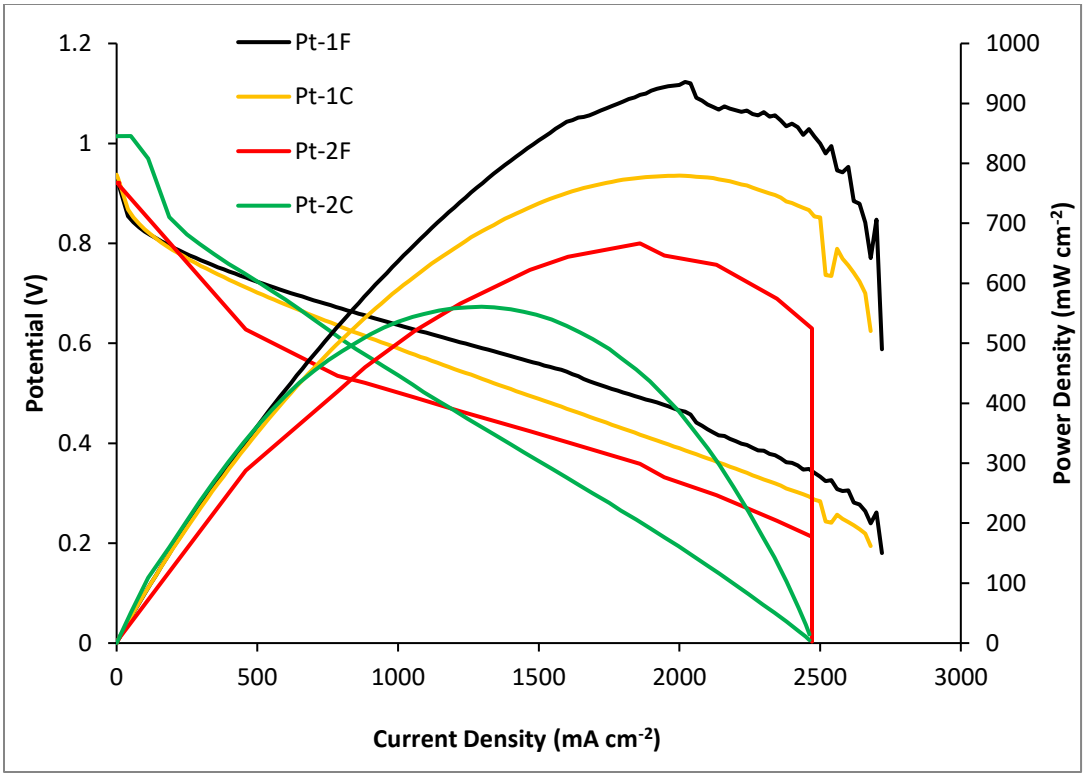

Fig. S24. Polarization curves for MEAs with the anode electrode using the Pt-1 or Pt-2 catalyst at 25 ℃.

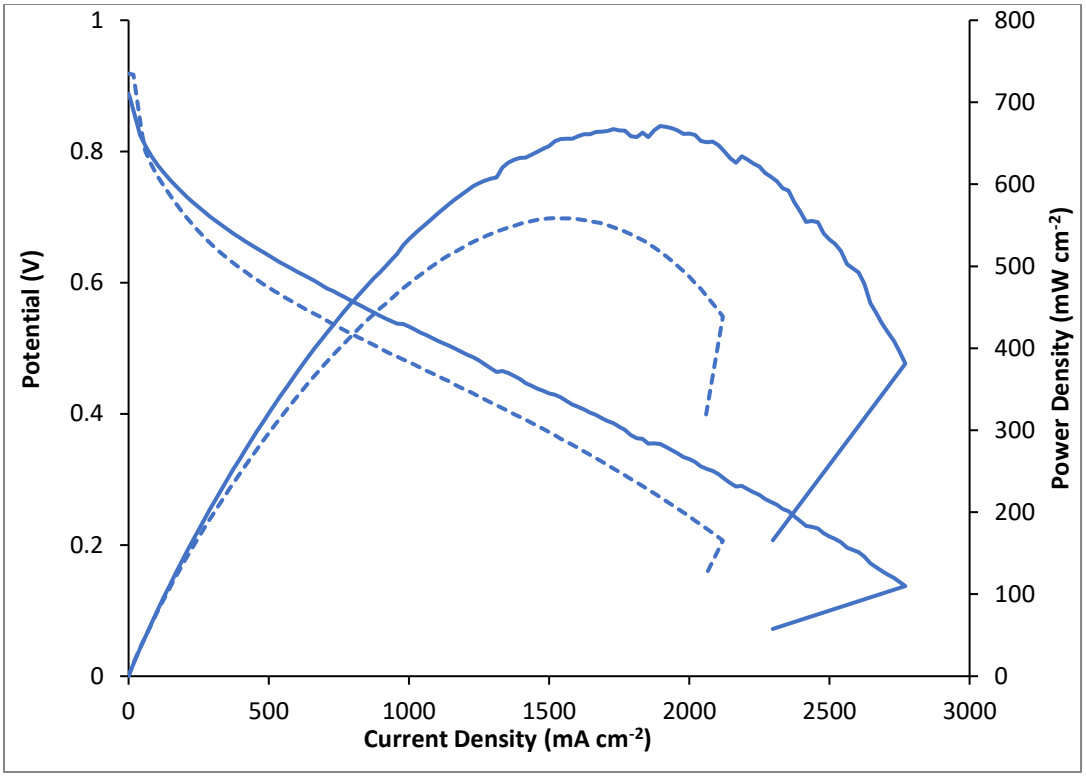

Fig. S25. Polarization curves for the MEAs with Pt-1 anode and Pt-2 cathode electrodes at 25 °C, solid lines indicate CFx supported and dashed lines indicate XC-72R supported catalyst.

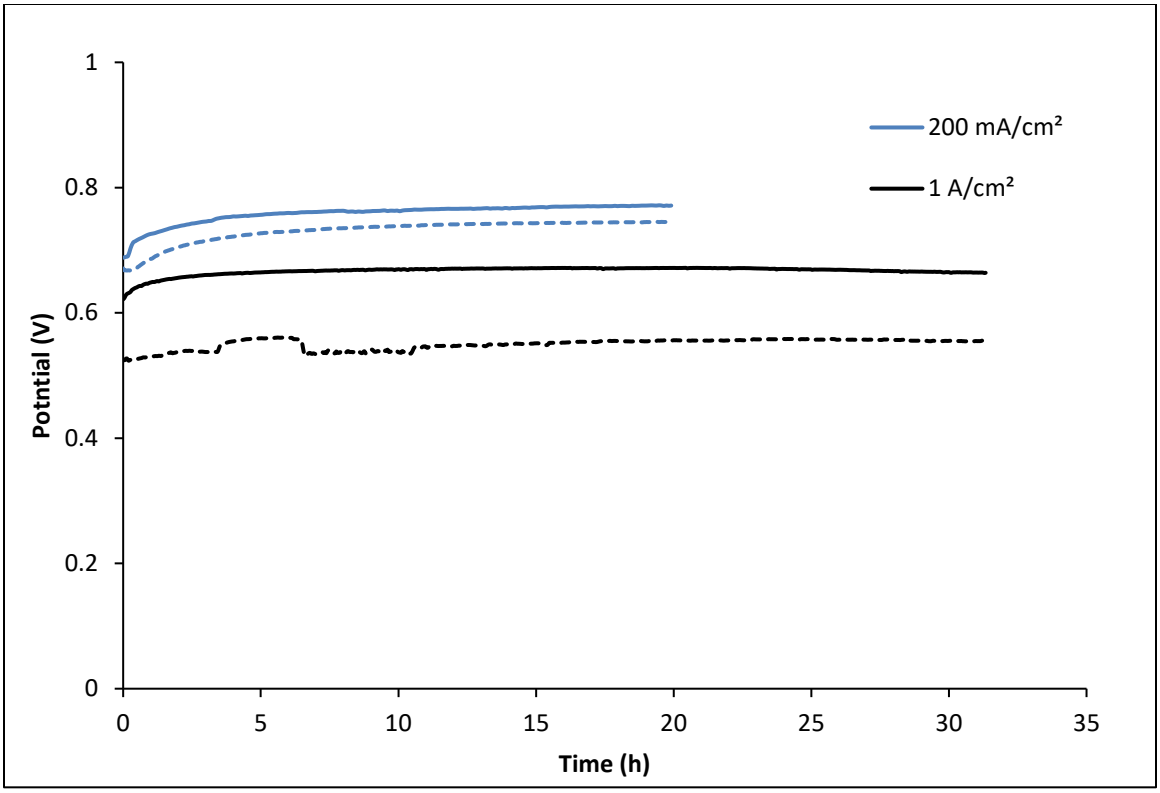

Fig. S26. MEAs held at constant currents with Pt-1 anode and Pt-2 cathode electrodes at 60 ℃. Solid lines indicate CFx supported and dashed lines indicate XC-72R supported catalyst.